VIBRATIONAL ANHARMONICITY IN THE WATER-NITRATE COMPLEX, ICE, AND GAS HYDRATES: APPLICATIONS TO SPECTROSCOPY AND THERMAL TRANSPORT

by

Eric G. Kratz

B.S. Millersville University, 2008

Submitted to the Graduate Faculty of

the Kenneth P. Dietrich School of

Arts and Sciences in partial fulfillment

of the requirements for the degree of

Doctor of Philosophy

University of Pittsburgh

2014

UNIVERSITY OF PITTSBURGH

KENNETH P. DIETRICH SCHOOL OF

ARTS AND SCIENCES

This dissertation was presented

by

Eric G. Kratz

It was defended on

May 14, 2014

and approved by

Kenneth D. Jordan, Professor, Department of Chemistry

Geoffrey R. Hutchison, Professor, Department of Chemistry

David H. Waldeck, Professor, Department of Chemistry

Alan J. H. McGaughey, Professor, Department of Mechanical Engineering, Carnegie Mellon

University

Dissertation Director: Kenneth D. Jordan, Professor, Department of Chemistry

VIBRATIONAL ANHARMONICITY IN THE WATER-NITRATE COMPLEX, ICE, AND GAS HYDRATES: APPLICATIONS TO SPECTROSCOPY AND THERMAL TRANSPORT

Eric G. Kratz, PhD

University of Pittsburgh, 2014

Vibrational anharmonicity strongly influences the properties of gas-phase complexes and solids. Anharmonicity is responsible for the observation of "forbidden" vibrational transitions, thermal expansion, and phonon-phonon scattering.

In the first portion of this dissertation the vibrational spectra of $NO_3^-{\cdot}H_2O$ and its isotopologues are examined through effective Hamiltonian and vibrational configuration interaction calculations employing *ab initio* force constants. While a harmonic treatment of the $NO_3^-{\cdot}H_2O$ infrared absorption spectrum predicts two OH stretch transitions, four strong peaks are experimentally observed. Anharmonic vibrational calculations confirm that the "extra" transitions are due to the rocking motion of the water molecule relative to the nitrate ion and a Fermi resonance between the OH stretch and water bend overtone.

The second part of the dissertation explores the nature of the vibrational anharmonicity of gas hydrates and ice Ih as well as its effects on the structure and thermal conductivity. The arrangement of the hydrogen atoms in the solids and the gas-water interactions are found to have a strong influence on some of the properties of the crystals. Coarse-grained simulations and analytic scattering approximations qualitatively reproduce the observed behavior of the thermal conductivity of gas hydrates and ice. In addition, the calculations reveal that guest-host coupling cannot fully explain the differences in the thermal conductivity of gas hydrates and ice.

TABLE OF CONTENTS

LIST OF TABLES

LIST OF FIGURES

PREFACE

Since graduate studies are never easy, I would like to take a moment to acknowledge and thank those who have given me support and guidance. My parents (Patricia and Michael Kratz), who spent decades listening to my rambling discussions of robotics, dinosaurs, and physics, have been one of the strongest influences during my scientific career. They have given me financial and emotional support, and the confidence to ask anyone questions when I want to understand how something works. Most importantly, they have raised me in a loving and supporting environment.

During my long and ~~torturous~~ tortuous path through graduate school, I have had the good fortune of making a large number of friends. While the contributions of my individual friends are too numerous to discuss here, I would like to thank the members of the Siska, Earl, and Jordan research groups. In the last six years, all of them have been vital to my sanity and have acted as a sounding board so that I could work through my ideas.

I would also like to thank Dr. David Earl. My time in his research group started me on the path to becoming a theoretical chemist. Most of my research would have been significantly harder without the programming skills I learned in the Earl group.

Most importantly, I would like to thank my research advisor Dr. Ken Jordan. Over the last four years he has been a fantastic source of advice, encouragement, and knowledge. Thank you for putting up with my unusual work schedule and allowing me to proceed with my research in my own way.

1.0   INTRODUCTION

1.1   INTERACTIONS OF OF WATER MOLECULES

Water is one of the most important substances on Earth and one of the most well studied.[1,2,3,4,5,6,7,8,9,10] However, due to its role in life, science, and technology, the interaction between water and other molecules is still an active research topic. Calculations of the properties of water containing systems or water-molecule interactions are complicated by nuclear quantum effects,[11,12,13,14] the use of force field models of varying accuracy,[1,15,16,17] and the scale of the system. Of particular interest are the interactions of water with small molecules and in molecular clusters.[18,19,20,21,22,23,24,25] These systems can serve as an important test of the accuracy of empirical and *ab initio* computational methods. To that end, studies of the vibrational spectrum of $NO_3^- \cdot (H_2O)_n$ clusters can give insight into the bonded and non-bonded interactions of the molecules.[18,24,26,27,28] The water molecules in ion-water clusters are often appreciably distorted away from their gas phase geometry[29] and display rich structure in the infrared absorption spectrum.[27] Due to the complicated nature of the vibrational coupling and geometric distortion, high-quality *ab initio* calculations need to be employed to unravel the spectra.

At low temperatures water can form many different solid phases[3,30,31,32,33,34] or can form cage-like structures which can trap small molecules.[35,36] While many solids consisting primarily of water are only stable under extreme conditions, ice Ih and gas hydrates are plentiful in the oceans and permafrost.[37,38,39] In particular methane hydrate is of interest due to its potential role in climate change,[38,39] fuel harvesting, and clogged natural gas pipelines.[40] Methane trapped in gas hydrate deposits on the ocean floor could be extracted to increase fossil fuel supplies, however, methane is a much more potent greenhouse gas than

carbon dioxide.[41] The methane can be released by rapid heating (fuel harvesting), gradual heating (climate change), or destabilization of the ocean sediments.

Studying the thermal and mechanical properties of solids at low temperatures often requires methods which account for the nuclear quantum effects.[42, 43, 44, 33, 34] Classical simulations overpopulate high-frequency vibrations and do not include the effects of the quantum ground state (zero-point) vibrations. Rigid water models often perform well in classical simulations since the constraints remove the high-frequency motions of the hydrogen atoms. However, flexible models do not introduce errors into the quantum simulation methods since the phonon populations are consistent with the Bose-Einstein distribution. Accordingly, the quantum methodologies are most appropriate appropriate for simulations of ice and gas hydrates at low-temperatures. The thermal and mechanical properties of ice and gas hydrates are of interest to industrial and environmental organizations that would like to determine how the methane is released from ocean sediments as the temperature rises.

1.2   NUMERICAL METHODS

While large portions of undergraduate and graduate chemistry courses are focused on analytic approaches, analytic solutions often do not exist for complicated systems. Fortunately, the prevalence of computers allows for accurate approximations of quantum or classical dynamics and properties. The remainder of this chapter gives a brief review of numerical approaches for the study of vibrational spectroscopy and thermal transport.

1.3   VIBRATIONAL CALCULATIONS

1.3.1   Quantum Harmonic Oscillator

The study of molecular vibrations and rotations are important for extracting information on the nature of the bonded and non-bonded interactions of molecules. The vibrational

patterns can be measured experimentally through infrared, Raman, and neutron scattering spectroscopies. Vibrational spectroscopy gives insight into the composition, bond structure, and interactions of the system. The peaks in infrared and Raman spectra can be assigned based on experimental data or by calculating the vibrational frequencies of the molecules. The simplest theoretical model of vibrations is based on the harmonic oscillator for which the Schrödinger equation can be solved analytically with a wave function built from the Hermite polynomials multiplied by a Gaussian function. The solution to the quantum harmonic oscillator can also be found by diagonalizing the Hessian matrix, which gives the normal modes and harmonic frequencies.

For linear molecules, two of the frequencies calculated from the Hessian matrix are rotations, and three others are translations. The rotations are low-frequency modes, and can be excited simultaneously with the vibrations. The simplest method for treating the rotations of molecules is the rigid rotor model, where the molecule is treated as if the bond lengths do not change during as the molecule rotates. For a linear diatomic molecule the Hamiltonian for the vibrations and rotations in inverse centimeter units is given by

$$\hat{H} = \frac{\hat{p}^2}{2} + \frac{J(J+1)}{2I} + \frac{\omega^2 \hat{q}^2}{2} , \qquad (1.1)$$

where ω^2 is the force constant for the vibration, $\hat{p}$ is the momentum operator, I is the moment of inertia (in inverse centimeter units), J is the total angular momentum quantum number, and $\hat{q}$ is the coordinate operator for the mass-scaled displacement from the potential energy minimum. The Schrödinger equation can be solved using this Hamiltonian to give the rovibrational frequencies of the linear diatomic. The calculated energy levels from this Hamiltonian do not match the experimental frequencies due to the anharmonicity and non-rigidity of the bond. The harmonic frequencies generated by diagonalizing the Hessian matrix are typically 5-10% higher than the observed frequencies[45] and must be multiplied by a scale factor to improve the agreement with observed values. Since harmonic oscillators are non-interacting, the vibrations need to be corrected for anharmonicity so that the vibrations can be coupled.

1.3.2 Anharmonic Oscillator

Anharmonicity can be introduced into the rovibrational energies by using a more complicated molecular Hamiltonian, such as the Watson Hamiltonian.[46] The Hamiltonian includes the normal mode kinetic energy, the kinetic energy due to rotations, and the anharmonic potential,

$$\hat{H} = \hat{T}_l + \hat{T}_c + \hat{V}(Q) \ . \tag{1.2}$$

The kinetic energy terms included in the Watson Hamiltonian are defined as

$$\hat{T}_l = \sum_i \frac{\hat{p}_i^2}{2} \ , \tag{1.3}$$

and

$$\hat{T}_c = \frac{1}{2}\sum_{\alpha\beta}(\hat{J}_\alpha - \hat{\pi}_\alpha)\mu_{\alpha\beta}(\hat{J}_\beta - \hat{\pi}_\beta) - \frac{1}{8}\sum_\alpha \mu_{\alpha\alpha} \ , \tag{1.4}$$

where T_l is the kinetic energy due to motions along the (3N-6) normal coordinates, T_c is the kinetic energy due to non-rigid rotations of the molecule, $\hat{J}$ is the total angular momentum operator, $\hat{\pi}_\alpha$ is the vibrational angular momentum operator, $\mu_{\alpha\beta}$ is the inverse of the moment of inertia, and α, β refer to the Cartesian coordinates.

The anharmonic potential energy is given by

$$\hat{V}(Q) = \sum_i V_i(q_i) + \sum_{ij} V_{ij}(q_i, q_j) + \sum_{ijk} V_{ijk}(q_i, q_j, q_k) + \cdots \ , \tag{1.5}$$

where q_i is a normal coordinate and Q represents the set of all the normal modes. The potential term, $\hat{V}(Q)$, is due to both the harmonic frequencies and the coupling of the normal modes. The accuracy of the potential depends on the amount of coupling that is included and the accuracy of the electronic structure calculations employed to generate the potential. While the full Hamiltonian includes the rotational degrees of freedom, their impact on the energy levels are negligible in large systems and can often be neglected. The Schrödinger equation employing the molecular Hamiltonian is typically solved via perturbation theory,[47,29] configuration interaction,[48] self-consistent field,[48] and Monte Carlo approaches.[25,49,50]

1.3.3 Periodic Systems

The vibrations of solids (phonons) can be determined through lattice dynamics (LD) calculations and be employed to calculate the heat capacity and thermal conductivity. Due to the periodic nature of solids, the Hessian matrix no longer predicts the entire vibrational spectrum. The vibrational frequencies of a periodic system depend on the wave vector, which is sometimes referred to as the crystal momentum of the phonon. When the wave vector dependence of the modes is introduced into the Hessian matrix, it becomes the dynamical matrix. The phonon frequencies and vibrational modes are determined by diagonalizing the dynamical matrix, $D(k)$,[51,52]

$$D(k)\epsilon(k,\nu) = \omega^2(k,\nu)\epsilon(k,\nu) . \tag{1.6}$$

Here $\epsilon(k,\nu)$ is the polarization vector (vibrational modes), k is the wave vector, and ν is the dispersion branch. The dynamical matrix is related to the equations of motion[51]

$$m_j \ddot{u}_j^n(t) = \sum_{j'n'} \Phi_{jj'}^{nn'} u_j^n(t) , \tag{1.7}$$

where u is the displacement from the minimum, Φ is the force constant matrix, j is the atom index, m_j is the mass of atom j, and n is the unit cell index. The force constant matrix elements are defined using the second derivatives in the truncated Taylor series expansion of the potential.

$$\Phi_{jj',\alpha\beta}^{nn'} = \begin{cases} -\nabla_\alpha \nabla_\beta V(R) & j, n \neq j', n' \\ \sum_{j''n''} \nabla_\alpha \nabla_\gamma V(R) & j, n = j', n' \end{cases} , \tag{1.8}$$

where R represents the positions of all of the atoms and (α,β,γ) refer to the Cartesian coordinates of the atom with indices $\{j,n\}$, $\{j',n'\}$, and $\{j'',n''\}$, respectively. The displacement from the minimum can be written in terms of the equations above as

$$u_j^n(t) = \sum_{k,\nu} m_j^{-\frac{1}{2}} \epsilon_j(k,\nu) e^{i[k \cdot r_j^n - \omega(k,\nu)t]} , \tag{1.9}$$

where r_j^n is the position of atom j in unit cell n. Employing the expressions above, the dynamical matrix becomes

$$D_{\eta,\mu}(k) = \frac{1}{\sqrt{m_j m_{j'}}} \sum_{n'} \Phi_{jj',\alpha\beta}^{0n'} e^{ik \cdot [r_{j'}^{n'} - r_j^0]} , \tag{1.10}$$

5

where $\eta = 3(j-1) + \alpha$ and $\mu = 3(j'-1) + \beta$.

Harmonic lattice dynamics can be employed to determine phonon frequencies, vibrational modes, and the heat capacity, but anharmonic corrections are required to calculate the thermal conductivity and more accurate frequencies. Anharmonic corrections can be included by using the third and fourth derivatives in the Taylor series expansion of the potential. The perturbative corrections add a frequency shift, $\Delta(k, \nu)$, and a line width, $\Gamma(k, \nu)$, to the phonon spectrum calculated with the harmonic approximation.[53] The corrected frequencies become

$$\omega_a(k, \nu) = \omega(k, \nu) + \Delta(k, \nu) \ , \tag{1.11}$$

where $\omega_a(k, \nu)$ is the anharmonic frequency.

1.4 HEAT CAPACITY AND THERMAL CONDUCTIVITY

1.4.1 Debye Model

Since bulk solids effectively extend infinitely in all directions, it is often useful to discuss the density of states (DOS) rather than individual phonon frequencies. The Debye model represents the DOS as an elastic continuum which can be utilized to calculate the heat capacity of a solid based on its physical properties.[54] The dispersion relation for the phonons is given by

$$\omega(k) = v_s k \ , \tag{1.12}$$

where ω is the frequency and v_s is the speed of sound in the solid. The density of states is then written as

$$\Xi(\omega) = \frac{V \omega^2}{2\pi^2 v_s^3} \ , \tag{1.13}$$

where V is the volume of the solid and the cutoff frequency of the elastic continuum is defined as[54]

$$\omega_D^3 = \frac{6\pi^2 v_s^3 N}{V} \ , \tag{1.14}$$

where N is the number of particles. In order to make the expressions easier to manipulate, the frequencies can be converted to dimensionless units,

$$x = \hbar\omega\beta , \tag{1.15}$$

$$X_D = \hbar\omega_D\beta = \frac{\Theta}{T} , \tag{1.16}$$

and

$$\Theta = \frac{\hbar v_s}{k_b} \sqrt[3]{\frac{6\pi^2 N}{V}} , \tag{1.17}$$

where $\beta = 1/k_b T$, k_b is the Boltzmann constant, and Θ is the Debye temperature.

The harmonic oscillator thermal energy and heat capacity can be written in terms of x and Θ,

$$U = 9Nk_bT\left(\frac{T}{\Theta}\right)^3 \int_0^{X_D} \frac{x^3}{e^x - 1} dx , \tag{1.18}$$

$$C_V = \frac{\partial U}{\partial T} , \tag{1.19}$$

and

$$C_V = 9Nk_b\left(\frac{T}{\Theta}\right)^3 \int_0^{X_D} \frac{x^4 e^x}{(e^x - 1)^2} dx , \tag{1.20}$$

where U is the vibrational energy and C_V is the heat capacity at constant volume.

The Debye model produces relatively simple equations for thermal properties and can be used as an estimate of how the energy and heat capacity behave as a function of temperature. At very low temperatures the Debye model predicts that the heat capacity should have a T^3 dependence and that at temperatures much greater than the Debye temperature it should approach the classical limit, $3Nk_b$.[54] Figure 1.1 shows the heat capacity of a Debye solid with $\Theta = 192$ K.
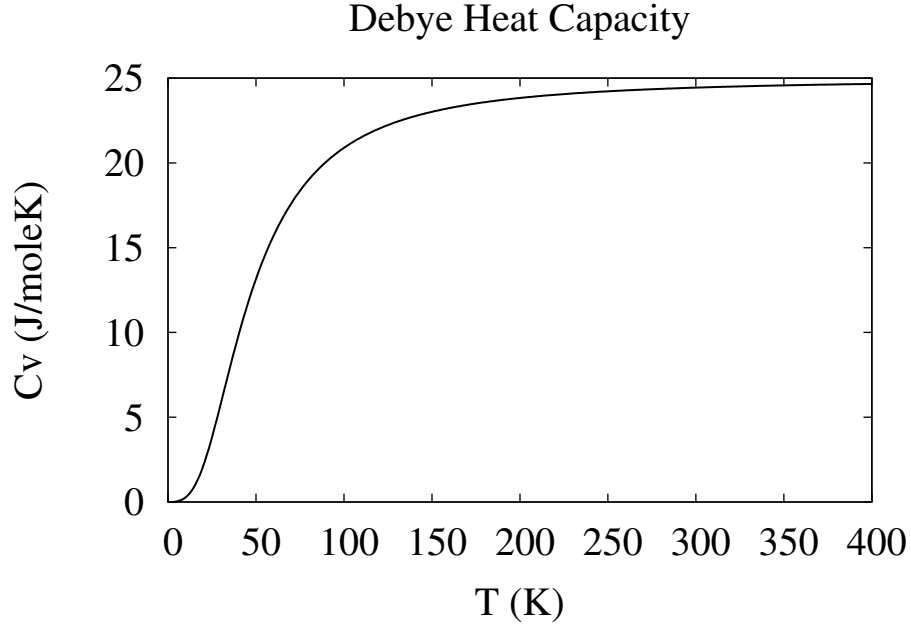
Figure 1.1: The heat capacity calculated using the Debye model with $\Theta = 192$ K.

1.4.2 Boltzmann Transport Equation

Thermal conductivity is a property that describes how well thermal energy moves through a solid.[53] Fourier's law gives the linear relationship between the heat flux and the temperature gradient.

$$J = \kappa \nabla T \ , \tag{1.21}$$

where J is the heat flux through a solid, κ is the thermal conductivity, and ∇T is the temperature gradient. The thermal conductivity can be calculated by using the Boltzmann transport equation (BTE) and the relaxation time approximation (RTA).[53,52] The single mode RTA-BTE is given by

$$\left(\frac{\partial f_t}{\partial t} \right)_{coll} = v_g \cdot \nabla T \left(\frac{\partial f_t}{\partial T} \right) \ , \tag{1.22}$$

$$f_t = f + f' \ , \tag{1.23}$$

and

$$\left(\frac{\partial f_t}{\partial t}\right)_{coll} = -\frac{f'}{\tau} \ , \tag{1.24}$$

where v_g is the group velocity of the phonon mode, f_t is the non-equilibrium phonon distribution function, f is the Bose-Einstein distribution function, f' is the fluctuation of the distribution function, $(\frac{\partial f_t}{\partial t})_{coll}$ represents the collisions of phonons, and τ is the phonon relaxation time. While Eqs. 1.22-1.24 are given for a single phonon mode, the extension to higher dimensions is straight forward. The equilibrium distribution function and the relaxation time can be found using the frequencies

$$f = \frac{1}{e^x - 1} \quad , \quad x = \hbar\omega\beta \ , \tag{1.25}$$

and line widths

$$\tau = \frac{1}{2\Gamma} \ . \tag{1.26}$$

By combining the equations above with the net phonon heat flux, the thermal conductivity can be calculated using

$$J = V^{-1} \sum_k \sum_\nu \hbar\omega v_g f' \ , \tag{1.27}$$

and

$$\kappa = V^{-1} \sum_k \sum_\nu \hbar\omega v_g^2 \tau \frac{\partial f}{\partial T} \ . \tag{1.28}$$

The phonon heat capacity can also be calculated with the following expression

$$C_V^p = V^{-1} \hbar\omega \frac{\partial f}{\partial T} \ , \tag{1.29}$$

where the superscript p indicates that the heat capacity is for a single phonon mode.

1.5   CLASSICAL SIMULATIONS

While the harmonic vibrational calculations described above include nuclear quantum effects and can easily be performed for both large and small systems, the computational cost of anharmonic corrections increases rapidly with the size of the system. For large systems, it is often useful to employ classical simulations which are far more efficient and include the full anharmonic potential instead of a Taylor series approximation.

1.5.1 Molecular Dynamics

Molecular dynamics (MD) simulations are performed on a collection of atoms by propagating Newton's equations of motion. The equations are discretized in time and are given by[55]

$$F_n = -\nabla V_n = m\ddot{r}_n \, , \tag{1.30}$$

$$\dot{r}_{n+1} = \dot{r}_n + \ddot{r}_n \Delta t \, , \tag{1.31}$$

and

$$r_{n+1} = r_n + \dot{r}_n \Delta t + \frac{\ddot{r}_n \Delta t^2}{2} \, , \tag{1.32}$$

where F is the force, V is the potential energy, r is a vector representing the potions of all atoms in the system, and Δt is the time interval between time step n and $n+1$. The natural ensemble for molecular dynamics is the mircocanonical ensemble (NVE), where the number of particles and energy are conserved inside a constant volume simulation box (SB). Although the NVE simulations are the native result of propagating Newton's equations, most experiments are typically performed in the canonical (NVT) or isothermal-isobaric (NPT) ensembles. In the NVT ensemble, the temperature is held constant instead of the energy, and the NPT ensemble also holds the pressure to be constant by adjusting the size of the SB.

1.5.2 Control of Temperature and Pressure

The temperature (pressure) in NVT (NPT) simulations is controlled through a thermostat (barostat) which links the system to an external "bath". The temperature and pressure can be controlled through scaling procedures,[56] modified equations of motion (non-Newtonian),[57] and stochastic processes.[58] The Berendsen thermostat (barostat) scales the kinetic energy (volume) so that a fluctuation in the temperature (pressure) relaxes to the desired magnitude in a set amount of time.[56] While this type of procedure is easily implemented and does not significantly impact the dynamics (weak coupling), it does not reproduce the true NVT (NPT) ensemble. Another procedure is to derive damped and driven equations of motion that are designed to reproduce fluctuations consistent with the canonical or isothermal-isobaric

ensembles. A popular procedure of this class of thermostats and barostats is the Nosé-Hoover method.[57]

1.5.3 Thermal Conductivity from Non-Equilibrium Molecular Dynamics

An alternative to the BTE approach for calculating the thermal conductivity is to perform classical simulations of the heat flow through the SB. A solid, liquid, or gaseous system is constructed in a SB with a large aspect ratio. The two ends of the SB become the heat source and heat sink where energy is added or removed from the system, respectively. If a temperature gradient is imposed across the SB, then the two sides of the system are no longer in thermal equilibrium and, hence, the simulations are no longer sampling the equilibrium NVE, NVT, or NPT ensembles. Non-equilibrium molecular dynamics (NEMD) simulations of the thermal conductivity are based on Fourier's law,

$$J = \kappa \nabla T \; , \tag{1.33}$$

where J is the heat flux, κ is the phonon thermal conductivity, and ∇T is the temperature gradient. The flux and temperature gradient can be extracted directly from the molecular dynamics (MD) simulations to calculate the thermal conductivity,

$$\kappa = \frac{|\Delta E_\pm| \Delta z}{A \Delta T \Delta t} \; , \tag{1.34}$$

where $\Delta E_\pm$ is the energy added (+) or removed (-) at the edges of the SB, Δz is the distance between the heat source and sink, Δt is the simulation time, and ΔT is the difference in temperature between the heat source and sink. The thermal conductivity can be determined using two different approaches[59, 60, 61, 62, 63] by applying either a heat flux, $(|\Delta E_\pm|/A\Delta t)$, or a gradient, $(\Delta T/\Delta z)$, during the simulations. Unfortunately, the NEMD approach introduces artificial boundaries in the SB. Phonons can scatter off of the boundaries and hence, the thermal conductivity will be underestimated. The thermal conductivity calculated using NEMD simulations can be corrected by performing the simulations for a range of system sizes and extrapolating to the bulk limit. NEMD simulations are not the only method to calculate the thermal conductivity through classical simulations, however, they are the most straight forward and trivially easy to implement.

2.0 VIBRATIONAL SPECTROSCOPY OF THE WATER-NITRATE COMPLEX IN THE OH STRETCHING REGION

2.1 PREFACE

This chapter was previously published as:

Nadja Heine[*], Eric G. Kratz[*], Risshu Bergmann, Daniel P. Schofield, Knut R. Asmis, Kenneth D. Jordan, and Anne B. McCoy; Vibrational Spectroscopy of the Water-Nitrate Complex in the OH Stretching Region; J. Phys. Chem A; doi:10.1021/jp500964j

[*] Authors contributed equally

Some modifications have been made to the text. In particular the supporting information was extended to include additional information on the anharmonic force constants. The IRMPD experiments on the $NO_3^- \cdot H_2O$ complex were performed by Nadja Heine and Risshu Bergmann. The generation of molecular geometries for the CCSD(T)-F12/VTZ-F12 potential energy surface was performed by Daniel P. Schofield. Anne B. McCoy performed diffusion Monte Carlo simulations employing the CCSD(T)-F12/VTZ-F12 potential energy surface.

2.2 INTRODUCTION

Nitrate ions in aqueous media play an important role in a wide range of environmental and biological processes. The nitrate anion is the major chromophore in the Antarctic snow.[64] Nitrate is also one of the most abundant tropospheric ions and a major constituent of sea salt and mineral dust aerosols.[65,66] A fundamental understanding of how nitrate ions are hydrated in the bulk[28] as well as at the air-aqueous interface[67] is thus of importance with

respect to understanding atmospheric aerosol chemistry. Spectroscopic studies of anion-water clusters in the gas phase,[68, 69, 70, 71, 72] in general, and on nitrate-water clusters,[27] in particular, play an important role in elucidating the nature of ion-water interactions one water molecule at a time (microhydration) in the absence of counter ions and of an extended solvation network. In the present study we focus on characterizing the interaction of the nitrate anion with a single water molecule and report vibrational spectra of the gas phase $NO_3^- \cdot H_2O$, $NO_3^- \cdot D_2O$, and $NO_3^- \cdot HDO$ isotopologues in the OH (and OD) stretching region measured using temperature-dependent infrared multiphoton dissociation (IRMPD) spectroscopy.

Studies of other water-anion complexes[73, 29, 74, 75] have shown that, in general, there is a significant red-shift of the water OH stretch vibration in the complexes compared to the gas-phase water monomer. In addition, in the case of $HCO_2^- \cdot H_2O$, $CH_3NO_2^- \cdot H_2O$ and $CH_3CO_2^- \cdot H_2O$, the vibrational spectra in the OH stretch region display progressions of up to five members with observed spacings of about 80 cm^{-1}. These progressions are due to the water rock vibration and result from a large cubic force constant coupling the OH stretch and water rock degrees of freedom.

Robertson et al.[74] have found that for complexes adopting a single ionic hydrogen-bond motif (SIHB), the red-shift of the OH stretch is well-correlated to the proton affinity of the anion. In contrast for the double ionic hydrogen bond motif (DIHB), the red-shift is about 200 cm^{-1} smaller than for SIHB complexes with similar proton affinities. We note further that although $HCO_2^- \cdot H_2O$, $CH_3NO_2^- \cdot H_2O$ and $CH_3CO_2^- \cdot H_2O$ adopt DIHB structures, $NO_2^- \cdot H_2O$ adopts a SIHB structure. It is not clear *a priori* which bonding motif would be adopted by the $NO_3^- \cdot H_2O$ complex. Anion photoelectron spectroscopy[23] as well as IRMPD experiments[27] in the fingerprint region (600-1800 cm^{-1}) are not conclusive, although both favor the DIHB motif based on predictions from electronic structure calculations. However, the exact nature of the DIHB global minimum energy structure, either a symmetric C_{2v} isomer with two equivalent hydrogen bonds[76, 21, 24] or a slightly asymmetric variant of C_s symmetry,[71, 27, 19, 26, 77] remains unclear. Prior theoretical studies indicate that the global minimum of $NO_3^- \cdot H_2O$ is asymmetric but only 0.2-0.3 kJ/mol more stable than the C_{2v} transition state structure.

In order to aid in assigning the experimentally observed IRMPD spectra of $NO_3^- \cdot H_2O$, $NO_3^- \cdot D_2O$, and $NO_3^- \cdot HDO$ we have undertaken calculations of the vibrational spectra of

these species using model Hamiltonian approaches that allow for OH (OD) stretch-rock cubic coupling as well as for Fermi resonances with the water bend overtone. The calculations confirm our expectation that in all three isotopologues there is a progression due to the water stretch-rock coupling with spacings of approximately 80 cm^{-1}, with the further complication in the H_2O and D_2O cases of a Fermi resonance between the OH (OD) stretch modes and the water bend overtone.

2.3   EXPERIMENTAL DETAILS

The IRMPD experiments were carried out using a previously described ion-trap tandem mass-spectrometer.[27,78] Briefly, nitrate-water complexes are produced by electrospray in a modified commercial Z-spray source from a 1 mM solution of HNO_3 (Fluka) in a 1:3 mixture of 15 MΩcm deionized water and acetonitrile. For the isotopologues, 1.5 mM solutions of 1.5 mmol/L DNO3 in 1:3 deuterium oxide (both 99 atom % D, Sigma Aldrich) and acetonitrile are used. The beam of ions is skimmed and collimated in a decapole ion guide, and subsequently mass-selected in a commercial quadrupole mass filter. After mass selection, the cluster anions are deflected by 90° using an electrostatic quadrupole deflector and focused into a cryogenically-cooled ion trap, held at 15 K for the initial experiments and increased up to 300 K for the temperature-dependent measurements. Here, the anions are collected for 99 ms and thermalized through collisions with a He buffer gas. In a 10 Hz cycle, ions are extracted and focused into the center of the extraction region of a time-of-flight (TOF) mass spectrometer, where they interact with a tunable wavelength (2.5-4.5 μm) IR laser pulse from a nanosecond OPO/OPA IR laser system[79] with typical pulse energies of 5 mJ. If the wavelength of the IR radiation is in resonance with a vibrational transition, fragmentation of the (parent) anions occurs. All anions are extracted by a set of high voltage pulses and are detected as a function of their TOF using an MCP detector.

A mass spectrum is obtained for each laser shot. IR spectra are recorded by averaging over 50-70 TOF mass spectra per wavelength and scanning the laser wavelength. The fluence as well as the optical path length of the laser pulse is increased using a multipass cell-setup.[18]

The photodissociation cross section, $\sigma(\nu)$, is determined from the relative abundances of the parent and photofragment ions, $I_P(\nu)$ and $I_F(\nu)$, and the frequency dependent energy fluence (assuming a constant interaction area throughout the range of scanned wavelengths), $\phi_e(\nu)$, using[80]

$$\sigma(\nu) = -\phi_e(\nu)^{-1} \ln \left[1 - \frac{I_F(\nu)}{I_P(\nu) + I_F(\nu)} \right] . \tag{2.1}$$

2.4   IRMPD SPECTRA

2.4.1   15 K Spectra

Figure 2.1 shows an overview of the experimental IRMPD spectra of $NO_3^- \cdot H_2O$ and its hydrogen related isotopologues $NO_3^- \cdot D_2O$ and $NO_3^- \cdot HDO$, covering the OH (3200-3800 cm^{-1}) and OD (2300-2900 cm^{-1}) stretching regions. Band positions are listed in Table 2.1. The spectra were measured at an ion trap temperature of 15 K. The only observed photofragment is NO_3^-. The energy of at least two photons is required to overcome the predicted dissociation limit (see below) and hence the IRMPD intensities plotted in Figure 2.1 may deviate from a linear absorption behavior.

The IRMPD spectrum of cold $NO_3^- \cdot H_2O$ (see Figure 1a) shows a surprisingly rich structure in the hydrogen-bonded OH stretching region (¡3600 cm^{-1})[70] and little or no signal in the regions of the symmetric (ν_s, 3657 cm^{-1}) and antisymmetric (ν_a, 3756 cm^{-1}) stretching vibrational frequencies of the free water molecule,[81] suggesting the exclusive presence of a DIHB complex. At least five characteristic peaks are observed at 3363, 3398, 3464, 3542 and 3620 cm^{-1} and labeled A_0 to A_4, respectively. A closer look reveals a weak background throughout the 3200-3650 cm^{-1} range and several smaller features. The observation of a series of peaks in-between 3363 and 3620 cm^{-1} suggest that the two OH oscillators are coupled to one (or more) lower frequency modes. Indeed, the spectrum shows similarities with those reported earlier by Myshakin et al.[29] for Ar-tagged $CH_3NO_2^- \cdot H_2O$ and $CH_3CO_2^- \cdot H_2O$ and $HCO_2^- \cdot H_2O$ by Gerardi et al.[73] where this structure was assigned to a progression in the water rocking mode built on top of an OH stretch fundamental. In the present case, the spectrum
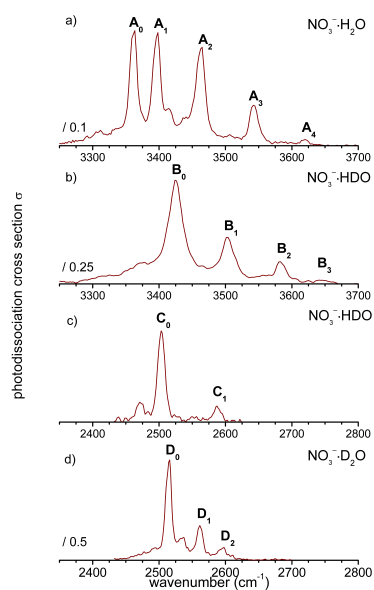
Figure 2.1: Experimental IRMPD spectra of the hydrogen-related isotopologues of the nitrate-water complex in the OH and the OD stretching region measured at an ion trap temperature of 15 K: (a) $NO_3^-\cdot H_2O$, (b-c) $NO_3^-\cdot HDO$, (d) $NO_3^-\cdot D_2O$. See Table 2.1 for peak positions.

appears more complex, as peaks A_0 to A_4 are not equidistantly spaced, but separated by 35 cm^{-1} (A_1-A_0), 66 cm^{-1} (A_2-A_1), 78 cm^{-1} (A_3-A_2), and 78 cm^{-1} (A_4-A_3).

Further insight into the assignment of the IRMPD spectra can be gained by isotopic substitution. The IRMPD spectrum of cold NO_3^-·HDO in the OH stretching region (see Figure 2.1b) indeed shows a similar, but simpler and slightly blue-shifted progression (B_0 to B_3) with an origin at 3423 cm^{-1} (B_0). Peaks B_0 to B_3 (see Table 2.1) are more evenly spaced: 78 cm^{-1} (B_1-B_0), 82 cm^{-1} (B_2-B_1) and 63 cm^{-1} (B_3-B_2). A shorter progression of similar spacing (84 cm^{-1}) is also observed in the OD stretching region (see Figure 2.1c) consisting of only two peaks at 2503 (C_0) and 2587 cm^{-1} (C_1). These observations are consistent with an assignment to progressions in the water rock mode (80 cm^{-1}), whose frequency is not expected to show a pronounced isotope-dependence, built on top of either the OD or OH stretching fundamental. They also suggest that the progression for NO_3^-·H_2O has an extra feature near the origin due to Fermi-type coupling to the water bend overtone $2\nu_b$.[82] The origin of the more than twice as broad peaks in the OH stretching region in the NO_3^-·HDO spectrum compared to the peaks observed in all the other spectra reported in Figure 2.1 remains unclear.

Finally, the IRMPD spectrum of cold NO_3^-·D_2O (see Figure 2.1d) looks similar to the NO_3^-·HDO spectrum in the OD stretching region (see Figure 2.1c), but exhibits an additional band at 2561 cm^{-1} (D_1). Assuming similar rocking vibrational frequencies for the H_2O, HDO and D_2O complexes, peaks D_0 and D_2, separated by 82 cm^{-1}, correlate to bands C_0 ad C_1. They thus correspond to the origin and first member of the stretch-rock progressions, of which the one observed in the NO_3^-·D_2O spectrum lies 13 cm^{-1} higher in energy. This leaves peak D_1 unassigned, which we tentatively attribute to overtone excitation of the D_2O bending vibration.

2.4.2   Temperature Dependent Spectra

IRMPD spectra of hotter NO_3^-·D_2O and NO_3^-·H_2O complexes, measured at ion trap temperatures up to room temperature, are compared to the 15 K spectra, discussed above, in Figure 2.2. The ions probed in the 50 K IRMPD spectra appear only slightly hotter than

17

Species	Band positions
$NO_3^- \cdot H_2O$	3363(A_0), 3398(A_1), 3464(A_2), 3542(A_3), 3620(A_4)
$NO_3^- \cdot HDO$	2503(C_0), 2587(C_1), 3423(B_0), 3501(B_1), 3583(B_2), 3646(B_3)
$NO_3^- \cdot D_2O$	2516(D_0), 2561(D_1), 2598(D_2)

Table 2.1: Positions (in cm^{-1}) of the main bands observed in the IRMPD spectra of $NO_3^- \cdot H_2O$, $NO_3^- \cdot HDO$ and $NO_3^- \cdot D_2O$ shown in Figure 2.1.
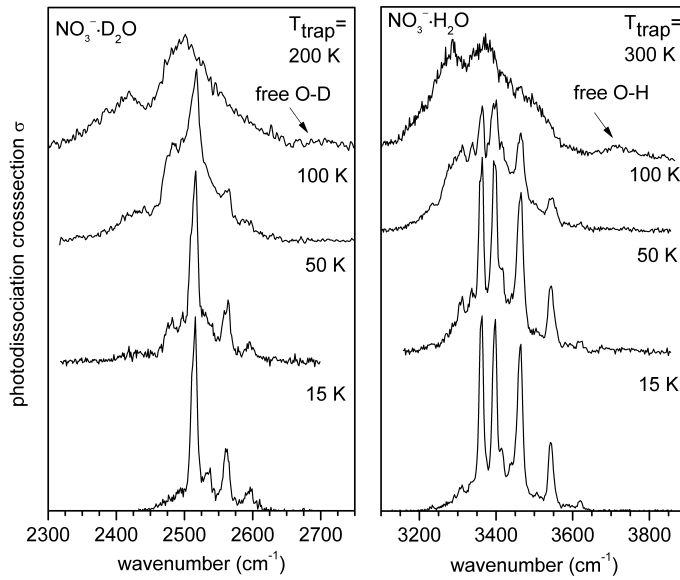
Figure 2.2: Experimental IRMPD spectra of $NO_3^- \cdot D_2O$ (left) and $NO_3^- \cdot H_2O$ (right) measured at ion trap temperatures of 15, 50, 100, 200 and 300 K. The 15 K spectra are the same as shown in Figure 2.1.

those in the 15 K spectra. This suggests, that the present experimental procedure of filling and extracting the ions, using a continuous buffer gas flow, allows for efficient thermalization of the ions slightly below 50 K, but probably not completely down to the lowest possible ion trap temperature of 15 K. At 100 K the observed features in the IRMPD spectra significantly broaden and hot bands to the red of the origins gain in intensity. At the highest temperatures measured, 200 K for $NO_3^- \cdot D_2O$ and 300 K for $NO_3^- \cdot H_2O$, the discrete features cannot be distinguished anymore and a continuous absorption is observed from 2300 to 2700 cm^{-1} ($NO_3^- \cdot D_2O$) and 3150-3700 cm^{-1} ($NO_3^- \cdot H_2O$). At these ion trap temperatures a new feature is observed in the free OD and free OH stretching regions, respectively, signaling the breaking of one of the two hydrogen bonds and the existence of both of SIHB and DIHB complexes.

2.5   COMPUTATIONAL DETAILS

The geometry optimizations and the calculations of the quadratic and cubic force constants were performed at the CCSD(T)[83,84]/aug-cc-pVDZ[85,86] level of theory with the *CFOUR* package.[87] To examine the sensitivity of the geometry and harmonic frequencies to the basis set, additional calculations were carried out at the CCSD(T)/aug-cc-pVTZ, CCSD(T)-F12b[88]/VDZ-F12,[89] and CCSD(T)-F12b/VTZ-F12 levels of theory. The F12 calculations were carried out with the *MOLPRO* package[90] since *CFOUR* lacks the explicitly correlated F12 method. In the computed spectra, transitions were given Gaussian widths with a half-width of 15 cm^{-1}, close to that of the peaks in the experimental spectrum of the $NO_3^- \cdot H_2O$ complex obtained at $T = 15$ K.

2.6   GEOMETRICAL STRUCTURE AND ADIABATIC POTENTIALS

The calculated minimum energy structure of $NO_3^- \cdot H_2O$ at the CCSD(T)/aug-cc-pVDZ level of theory has C_s symmetry and is depicted in Figure 2.3. This is in contrast to the $HCO_2^- \cdot H_2O$, $CH_3NO_2^- \cdot H_2O$ and $CH_3CO_2^- \cdot H_2O$ complexes, for which the two OH groups of the water

$R1 = 0.96$ Å $\qquad$ $R1 = 0.97$ Å $\qquad$ $R1 = 0.97$ Å

$R2 = 0.98$ Å $\qquad$ $R2 = 0.97$ Å $\qquad$ $R2 = 0.99$ Å

$\theta = 97.8°$ $\qquad$ $\theta = 96.5°$ $\qquad$ $\theta = 101.4°$

$E_{rel} = 0$ cm^{-1} $\qquad$ $E_{rel} = 11$ cm^{-1} $\qquad$ $E_{rel} = 962$ cm^{-1}
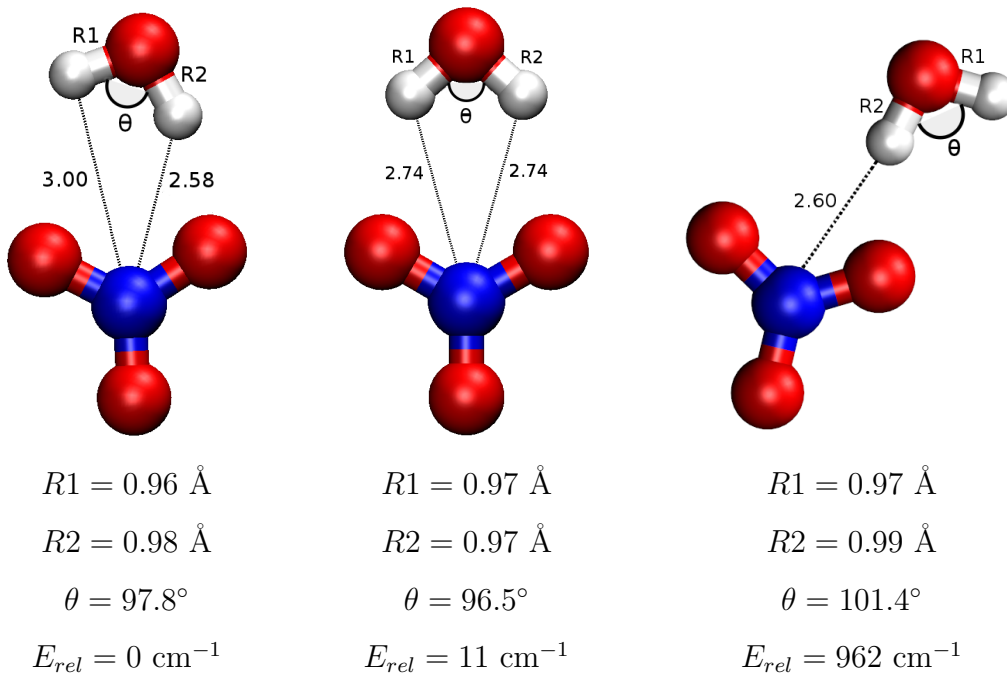
Figure 2.3: Structures of the $NO_3^- \cdot H_2O$ potential energy minimum (left) and C_{2v} transition state (middle) optimized at the CCSD(T)/aug-cc-pVDZ level of theory. The right-most structure corresponds to a local minimum energetically lying 962 cm^{-1} above the global minimum structure. The hydrogen-nitrogen distances are indicated in Angstroms.
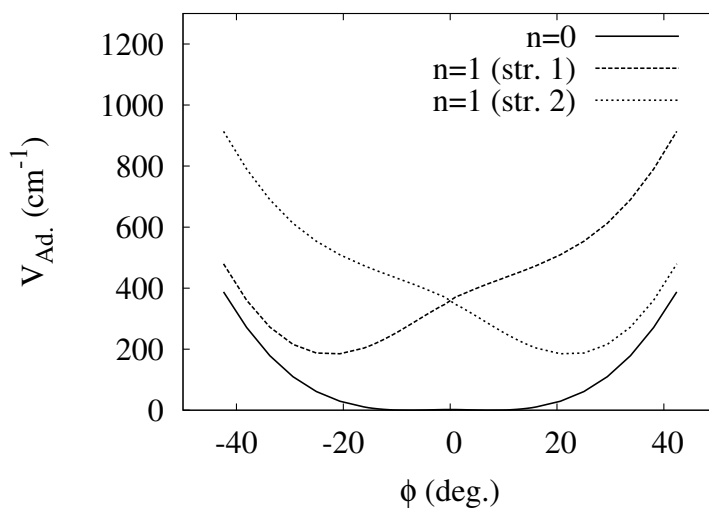
Figure 2.4: Adiabatic rock potentials for the $NO_3^- \cdot H_2O$ complex with 0 and 1 quanta in the OH stretch determined at the CCSD(T)/aug-cc-pVDZ level of theory. The OH stretch excited state potentials (str. 1 and 2) are depicted in the local mode representation. The excited state potentials have been shifted downwards by 3350 cm^{-1} for convenience.

molecule are symmetrically equivalent.[29,73] However, the C_{2v} transition state for conversion between the two symmetrical structures of $NO_3^- \cdot H_2O$ is calculated to be only 11 cm^{-1} above the potential energy minima at the CCSD(T)/aug-cc-pVDZ level of theory, in agreement with the calculations at the same level of theory in Ref.[27] This is much lower than the rock frequency, which is calculated to be 84 cm^{-1} in the harmonic approximation. A common aspect of the geometries of the $NO_3^- \cdot H_2O$, $HCO_2^- \cdot H_2O$, $CH_3NO_2^- \cdot H_2O$ and $CH_3CO_2^- \cdot H_2O$ complexes is the small water HOH angle, which is calculated to be 97.8° for the $NO_3^- \cdot H_2O$ complex. At the global minimum, the complex has a binding energy of approximately 5625 cm^{-1} calculated at the CCSD(T)-F12b/VTZ-F12 level of theory. In addition to the C_s global minimum, there is a second minimum lying 962 cm^{-1} above the global minimum. The high energy minimum has a larger HOH angle and is further distorted away from C_{2v} symmetry. Additional details on the water-nitrate intaction energy and the vibrationally averaged structure can be found in the supporting information.

21
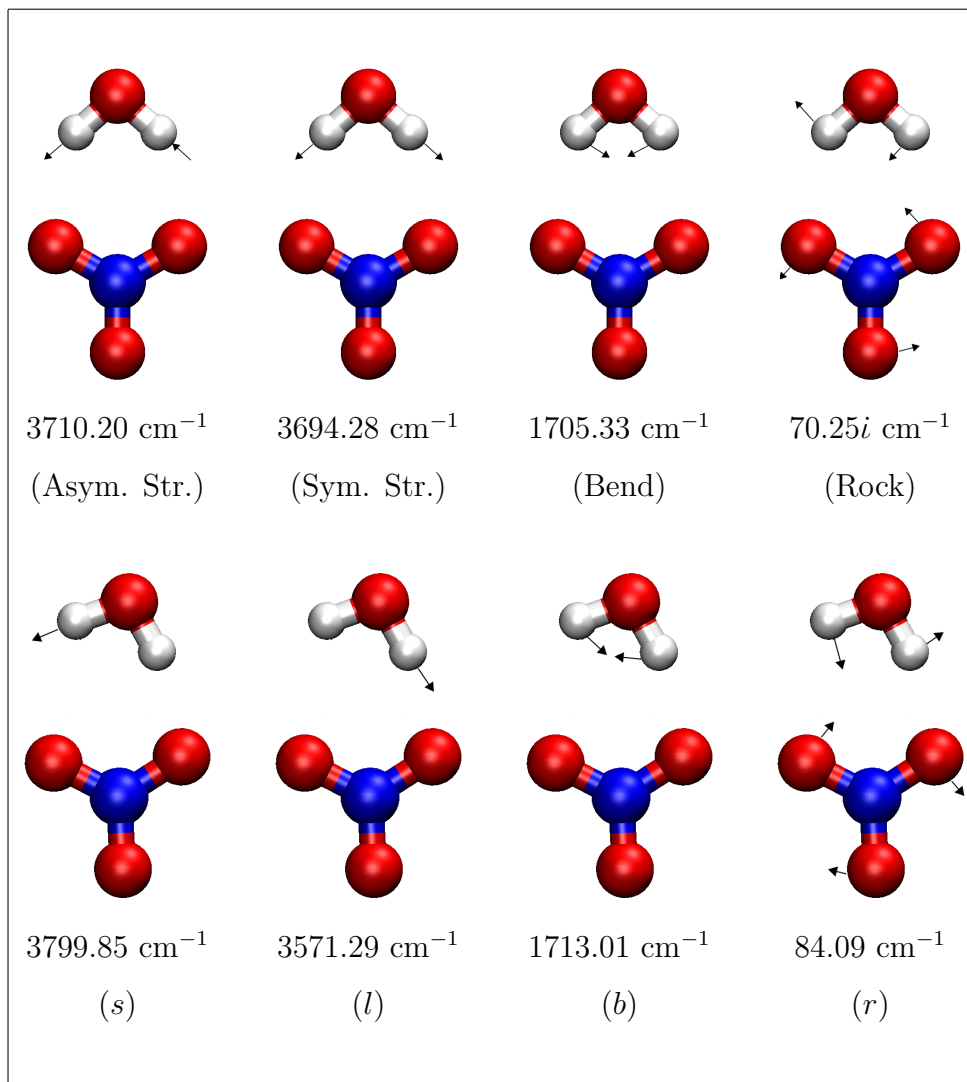
Figure 2.5: Harmonic frequencies of the four key vibrational modes of $NO_3^- \cdot H_2O$. Results for the C_s potential energy minimum are shown at the bottom of the figure and those for the C_{2v} transition state structure are shown at the top of the figure. All results are from CCSD(T)/aug-cc-pVDZ calculations. For the C_{2v} structure the depicted normal modes are antisymmetric stretch, symmetric stretch, water bend (b), and intermolecular rock (r), with the rock mode having an imaginary frequency. For the C_s minimum, the two water stretch vibrations are labeled as the long stretch (l) and short stretch (s), where long and short refer to the lengths of the water OH bonds. The bend and rock modes are labeled as (b) and (r), respectively.

In considering the distortion of the complex from C_{2v} symmetry it is useful to define the angle ϕ between the vectors bisecting the HOH angle of the water molecule and the ONO angle of the nitrate ion. The vectors are oriented so that the angle between them is 0° for the C_{2v} structure. At the minimum energy structure shown in Figure 2.3 the value of the ϕ angle is 15° compared to 0° in the transition state structure. The value of the ϕ angle at the potential energy minimum is very sensitive to the atomic basis set employed. As the basis set is expanded along the sequence aug-cc-pVDZ, aug-cc-pVTZ VDZ-F12, and VTZ-F12 the minimum energy structure becomes closer to C_{2v} symmetry, and the water rock harmonic frequency decreases. Here VnZ-F12 refers to CCSD(T)-F12b calculations with the VnZ-F12 basis set. With the largest basis sets employed, the value of the ϕ angle is only 4-7° at the potential energy minimum and the rock frequency is calculated to be only 20-35 cm^{-1} within the harmonic approximation. Thus it is possible that, in the limit of a complete basis set, the global minimum could have a C_{2v} structure.

Insight into the vibrational spectra of $NO_3^-\cdot H_2O$ and its isotopologues is provided by the calculating the adiabatic rock potentials for the complex with zero and one quanta in the OH stretch local mode degrees of freedom.

$$V_{Ad.}^{g.s.} = E_{B.O.}(\phi) + E_{ZPE}(\phi) , \tag{2.2}$$

and

$$V_{Ad.}^{ex.} = E_{B.O.}(\phi) + E_{ZPE}(\phi) + \omega_{loc}(\phi) , \tag{2.3}$$

where $V_{Ad.}^{g.s.}$ and $V_{Ad.}^{ex.}$ refer to the ground and excited state potentials, respectively, $E_{B.O.}(\phi)$ is the Born-Oppenheimer energy obtained from the geometry optimization at a fixed ϕ value, $E_{ZPE}(\phi)$ is the harmonic zero-point energy (ZPE) calculated using the optimized geometry and excluding the rock degree of freedom, and the last term in Eq. 2.3, $\omega_{loc}(\phi)$, is the frequency of the OH stretch local mode. Figure 2.4 reports the adiabatic rock potentials with zero or one quanta in the OH stretch obtained at the CCSD(T)/aug-cc-pVDZ level of theory. In the adiabatic ground state the rock potential is very flat, and, even in the absence of the small barrier at $\phi = 0$, the potential is highly anharmonic. The minima in the excited state potentials are displaced to $\phi = \pm 21°$, and the resulting potentials are more harmonic than the ground state potential. The crossing point of the two excited state potentials occurs about

23

175 cm^{-1} above their minima. Since the experimentally observed spacing in the progressions in the OH (OD) stretch region is about 80 cm^{-1}, the third energy level in the progression lies above the crossing point. In addition, given the shape of the excited state potentials shown in Figure 2.4, the spacing between the $n_r = 1$ and $n_r = 2$ levels would be expected to be smaller than that between the $n_r = 0$ and $n_r = 1$ levels. This suggests that the ϕ angle, as defined above, is not fully satisfactory for representing the rock coordinate. It is also likely that the shape of the $n_{loc} = 1$ potentials would differ if the curves were generated using the anharmonic frequencies for E_{ZPE} and ω_{loc}.

We have also calculated the adiabatic potentials at the CCSD(T)-F12b/VDZ-F12 level (see supporting information), obtaining potentials very close to those depicted in Figure 2.4. Thus, in spite of the sensitivity of the rock angle of the Born-Oppenheimer potential energy surface to the basis set, the adiabatic potentials, especially those for the excited state, are relatively insensitive to the basis set used in the calculations.

2.7   NORMAL MODES AND CUBIC FORCE CONSTANTS

The four key vibrations for understanding the anharmonic coupling in the OH stretch region of $NO_3^- \cdot H_2O$ spectrum are the two OH stretches, the water bend (b), and the water rock (r). These vibrations and their frequencies at the CCSD(T)/aug-cc-pVDZ level of theory are depicted for the C_{2v} and C_s structures in Figure 2.5. The two OH stretch modes become localized in the C_s structure, and the l and s labels refer to the long and short OH bonds, respectively. The calculated harmonic frequencies of these modes and the relevant cubic force constants are listed in Table 2.2. The table also includes results for the various isotopologues of the $NO_3^- \cdot H_2O$ complex. Separate entries are given for $NO_3^- \cdot HDO$ and $NO_3^- \cdot DHO$ complexes, where the first atom (H or D) specified for the water molecule refers to the atom engaged in the long OH bond, and we will define the coupling constants as coming from either the HDO or DHO complexes. A full list of the harmonic frequencies for the isotopologues can be found in the supporting information.

24

2.8   EFFECTIVE HAMILTONIAN

In their study of the $CH_3NO_2^- \cdot H_2O$ and $CH_3CO_2^- \cdot H_2O$ complexes, Myshakin et al.[29] introduced a model Hamiltonian employing harmonic OH stretch and water rock degrees of freedom together with a $\lambda q_a q_s q_r$ cubic coupling, where q_s and q_a are, respectively, the symmetric and antisymmetric OH stretch normal coordinates, and q_r is the water rock normal coordinate. By assuming an adiabatic separation between the OH stretch and water rock degrees of freedom, and switching to a local mode approximation for the OH stretch vibrations, Myshakin et al. obtained analytical expressions for the rock potentials for the system with $n_{loc} = 0$ and 1 quanta of OH stretch. This model predicts displaced minima for the $n_{loc} = 1$ stretch potentials with the displacements (in dimensionless coordinates) being $\Delta q_r = \pm \omega_{asr}/2\omega_r$, where ω_r and ω_{asr} are, respectively, the rock frequency and the cubic force constant in wavenumbers. The $n_{loc} = 0 \rightarrow 1$ OH stretch absorption spectrum is then given by

$$\Delta E(n_r) = \omega_{loc} - \frac{\omega_{asr}^2}{8\omega_r} + n_r \omega_r ~, \tag{2.4}$$

where ω_{loc} is the frequency of the OH stretch local mode, the second term on the right-hand side gives the red-shift of the origin, and n_r is the number of quanta in the $n_{loc} = 1$ potential.

The transition intensities for this model can be calculated using the overlap of harmonic oscillator wave functions of the ground and excited displaced harmonic potentials. Assuming that the ground state is in its zero-point level, the relative intensities of the levels in the progression are given by:[29]

$$I_{n_r} \propto \frac{exp(-0.5\Delta q_r^2)(\Delta q_r)^{2n_r}}{2^{n_r} n_r!} ~. \tag{2.5}$$

This model was quite successful at reproducing the observed vibrational spectra in the OH stretch region of $CH_3NO_2^- \cdot H_2O$ and $CH_3CO_2^- \cdot H_2O$.

The adiabatic model of Myshakin et al. assumes that the equilibrium structure is symmetrical and that the rock potential of the ground state is well described as harmonic. In this displaced oscillator model, the harmonic rock frequency is necessarily the same for the $n_{loc} = 0$ and $n_{loc} = 1$ potentials. However as seen from examination of the potential energy curves in Figure 2.4, this is not the case for $NO_3^- \cdot H_2O$.

Harmonic frequencies				
Mode	$NO_3^- \cdot H_2O$	$NO_3^- \cdot D_2O$	$NO_3^- \cdot HDO$	$NO_3^- \cdot DHO$
ω_s	3799.85	2763.94	2760.46	3797.68
ω_l	3571.29	2591.82	3571.60	2597.64
ω_b	1713.01	1246.16	1541.49	1476.68
ω_r	84.09	76.34	77.91	82.33
Cubic force constants				
Type	$NO_3^- \cdot H_2O$	$NO_3^- \cdot D_2O$	$NO_3^- \cdot HDO$	$NO_3^- \cdot DHO$
ω_{ssr}	-105.65	-78.54	-76.57	-106.10
ω_{llr}	242.42	169.11	234.97	174.47
ω_{sbb}	-99.33	-55.48	15.01	-268.60
ω_{lbb}	151.72	104.49	314.03	-12.39

Table 2.2: Selected harmonic frequencies and reduced cubic force constants (cm^{-1}) of $NO_3^-\cdot H_2O$ calculated at the CCSD(T)/aug-cc-pVDZ level of theory.

	Harmonic frequencies			Force constants	
Species	ω_1	ω_2	ω_r	ω_{11r}	ω_{22r}
$NO_3^-\cdot H_2O$	3571.29	3571.29	80.00	242.42	-242.42
$NO_3^-\cdot D_2O$	2591.82	2591.82	80.00	169.11	-169.11
$NO_3^-\cdot HDO$	3571.60	2597.64	80.00	234.97	-174.47

Table 2.3: Frequencies and reduced cubic force constants (cm^{-1}) used in the effective Hamiltonian calculations. The force constants for $NO_3^-\cdot HDO$ are taken from the long OH (OD) stretch modes from the calculations on $NO_3^-\cdot HDO$ and $NO_3^-\cdot DHO$ (Table 2.2).
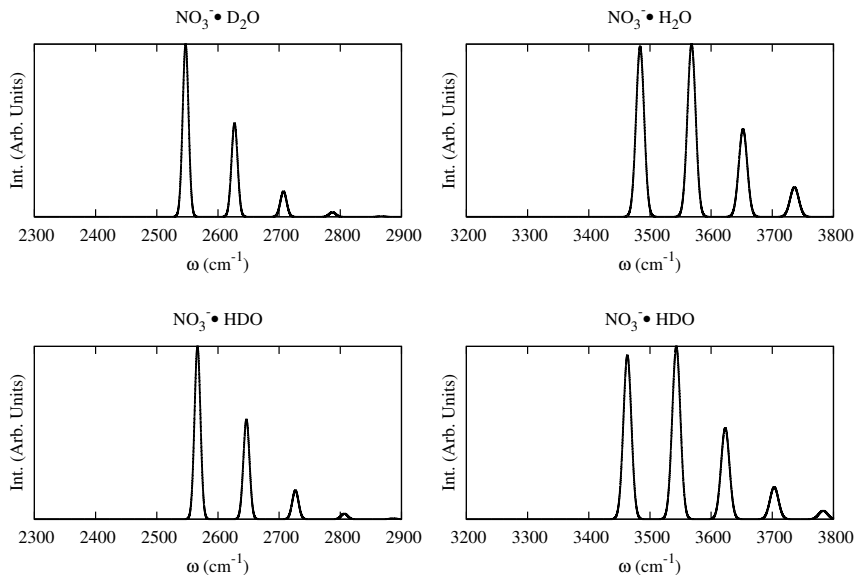
Figure 2.6: Vibrational spectra for the water-nitrate isotopologues generated using the effective Hamiltonian given by Eq. 2.12 and with intensities calculated using Eq. 2.5.

Diffusion Monte Carlo (DMC) calculations[50] (see supporting information) based on an analytical representation of the $NO_3^- \cdot H_2O$ potential energy surface calculated at the CCSD(T)-F12b/VTZ-F12 level give an anharmonic rock frequency close to 80 cm^{-1} for the ground state, which agrees well with the spacings of the observed progressions in $NO_3^- \cdot HDO$. This is appreciably larger than the 35 cm^{-1} value of the harmonic rock frequency calculated at the CCSD(T)-F12b/VTZ-F12 level of theory. Thus, it is fortuitous that the harmonic rock frequency from the CCSD(T)/aug-cc-pVDZ calculations is close to the observed splittings accompanying excitation of the OH stretch vibration in $NO_3^- \cdot HDO$.

In spite of the issues raised in the preceding paragraph, in the absence of Fermi resonances, the observed energy levels in the OH and OD stretch regions of $NO_3^- \cdot H_2O$ and its isotopologues are well described by

$$\Delta E(n_r) = \omega_{loc} - \Delta + n_r \omega_r \ , \tag{2.6}$$

where Δ is a frequency shift that depends on the anharmonic coupling, ω_r is the rock frequency associated with the $n_{loc} = 1$ potential. This has motivated us to apply an extension of the

27

model of Myshakin et al. to the water-nitrate complex. Specifically, the extended model allows for both OH (OD) stretch local modes, which is important for the $NO_3^-\cdot HDO$ complex. The relevant model Hamiltonian is given by

$$H = H_1 + H_2 + H_r + H_c \, , \tag{2.7}$$

$$H_i = \frac{p_i^2}{2} + \frac{\omega_i^2 q_i^2}{2} \, , \quad i = 1, 2, r \, , \tag{2.8}$$

and

$$H_c = \frac{\lambda_1 q_1^2 q_r}{2} + \frac{\lambda_2 q_2^2 q_r}{2} \, , \tag{2.9}$$

where H is the total Hamiltonian, H_1, H_2, and H_r are the Hamiltonians for the OH (OD) stretch and rock modes, H_c is the coupling Hamiltonian, and p_i, ω_i, q_i and λ_i are, respectively, the momentum, harmonic frequency, mass-scaled coordinate and cubic coupling constants for mode i. The two local modes are designated "1" and "2", while, as above, the rock mode is labeled by "r".

The effect of the cubic coupling on the frequencies of the OH (OD) stretch modes can be approximated as a first-order perturbation to the ground state energy.

$$E_i = \frac{\omega_i}{2} + \frac{\lambda_i}{2} \langle 0|q_i^2 q_r|0\rangle = \frac{\omega'_i}{2} \, , \tag{2.10}$$

where

$$\omega'_i = \omega_i + \frac{\lambda_i q_r}{2\omega_i} \, , \quad i = 1, 2 \, . \tag{2.11}$$

The same result can be obtained by completing the square giving, $\omega'_i = \sqrt{\omega_i^2 + \lambda_i q_r}$, and retaining the first two terms of the Taylor series expansion of the right-hand side.

Assuming that the stretch vibrations behave as harmonic oscillators with the new frequencies ω'_i, the effective Hamiltonian becomes

$$
\begin{aligned}
H^{eff} = &\frac{p_1^2}{2} + \frac{p_2^2}{2} + \frac{p_r^2}{2} \\
+ &\frac{\omega'^2_1 q_1^2}{2} + \frac{\omega'^2_2 q_2^2}{2} + \frac{\omega_r^2 q_r^2}{2} \, ,
\end{aligned}
\tag{2.12}
$$

which can be solved, within the adiabatic approximation, as if the system contains three independent harmonic oscillators.

28

The remainder of the derivation follows that of Myshakin et al.[29] and is given in the supporting information section. With the assumption that the OH stretch ground state is initially in the $n_r = 0$ level, the excitation energies are given by:

$$\Delta E_1(n_r) = \omega_1 - \frac{\omega_{11r}^2}{4\omega_r} - \frac{\omega_{11r}\omega_{22r}}{8\omega_r} + n_r\omega_r \, , \qquad (2.13)$$

where ω_{11r} and ω_{22r} are the reduced cubic coupling constants in inverse centimeter units,

$$\omega_{iir} = \frac{\lambda_i}{\omega_i\sqrt{\omega_r}} \, . \qquad (2.14)$$

An analogous expression, $\Delta E_2(n_r)$, is obtained for the second OH stretch local mode. It should be noted that Eq. 2.13 reduces to Eq. 2.4 when ω_{11r} and ω_{22r} are of equal magnitude with opposite signs, as occurs at C_{2v} symmetry. Since the CCSD(T)/aug-cc-pVDZ force constants are calculated with a ϕ value near the minimum in the $n_i = 1$ potentials, the local environment experienced by the long OH stretch can be assumed to provide a good approximation for the stretch local modes. In light of this, for $NO_3^- \cdot H_2O$ we take $\omega_1 = \omega_2 = \omega_l$, $\omega_{11r} = \omega_{llr}$, and $\omega_{22r} = -\omega_{llr}$. We further take $\omega_r = 80$ cm^{-1}. With these assumptions, the model gives potentials that approximately reproduce those in Figure 2.4. As with the original C_{2v} model, the transition intensities are estimated by Eq. 2.5.

This Hamiltonian can be readily applied to the $NO_3^- \cdot D_2O$, $NO_3^- \cdot DHO$, and $NO_3^- \cdot HDO$ isotopologues. Table 2.3 lists the values of the OH stretch and rock frequencies and the *iir* force constants used in the effective Hamiltonian calculations of the isotopologues. The assumptions for $NO_3^- \cdot D_2O$ are the same as for $NO_3^- \cdot H_2O$. However, since the two water stretching modes are not identical in the HDO (DHO) isotopologue, the effective Hamiltonian was constructed by employing the OH stretch parameters calculated for both $NO_3^- \cdot DHO$ and $NO_3^- \cdot HDO$. Specifically the harmonic frequencies are defined as $\omega_1 = \omega_l$ (HDO) and $\omega_2 = \omega_l$ (DHO), and the cubic coupling constants for this system are taken to be $\omega_{11r} = \omega_{llr}$ (HDO) and $\omega_{22r} = \omega_{llr}$ (DHO).

Qualitatively, the effective Hamiltonian calculations reproduce the trends in the experimental spectra except for the extra features that are due to Fermi resonances that are not accounted for by the model. Specifically, the model predicts red-shifts in the origin of the OH stretch-rock progression about two times larger than those found for OD, in qualitative

29

agreement with experimentally observed isotopic shifts. In the IRMPD spectrum of $NO_3^-\cdot D_2O$, the peaks in the stretch-rock progression are separated by ~ 40 cm^{-1}. However, it is likely that the bend overtone is coupling with the OD stretch and that the peak due to the Fermi resonance (D_1) appears between the $n_r = 0$ and $n_r = 1$ OD stretch-rock transitions, which would then correspond to D_0 and D_2, respectively.

The agreement between the model Hamiltonian and the experiments is quite good, however the model seems to incorrectly predict the relative shifts of the isotopologues. For instance the OH stretch vibration of $NO_3^-\cdot H_2O$ is blue-shifted above the $NO_3^-\cdot HDO$ OH stretch. This is likely due to the influence of the stretch-bend coupling which is strongest for the H_2O and D_2O isotopologues. While the model Hamiltonian predicts that the stretch-rock progression is shorter for $NO_3^-\cdot D_2O$ than for $NO_3^-\cdot H_2O$ in agreement with experiment, the lengths of both progressions are larger than experimentally observed. In part, this reflects the inadequacy of Eq. 2.5 to calculate the intensities, due to the neglect of non-linear terms in the dipole moment expansion and the fact that the rock potential for the $n_{loc} = 0$ ground state is highly anharmonic.

2.9 VIBRATIONAL CI

Although the effective Hamiltonian approach gives a qualitative description of the experimental spectra, a more sophisticated treatment is required to include the participation of Fermi resonances with the water bend overtone. To accomplish this, vibrational configuration interaction calculations were performed within the local mode approximation using the Hamiltonian:

$$H = H_1 + H_2 + H_b + H_r + H_c , \tag{2.15}$$

where H_1, H_2, and H_r are as defined above, H_b is the Hamiltonian for the HOH bend, and

$$H_c = \frac{\omega_{llr}}{2}(q_1^2 - q_2^2)q_r + \frac{\omega_{lbb}}{2}(q_1 + q_2)q_b^2 , \tag{2.16}$$

couples the OH stretch modes to both the rock and the bend modes. The basis functions used in the calculations were of the form $|n_1, n_2, n_b, n_r\rangle$, where n_1, n_2, n_b, and n_r refer to

(a)   (b)
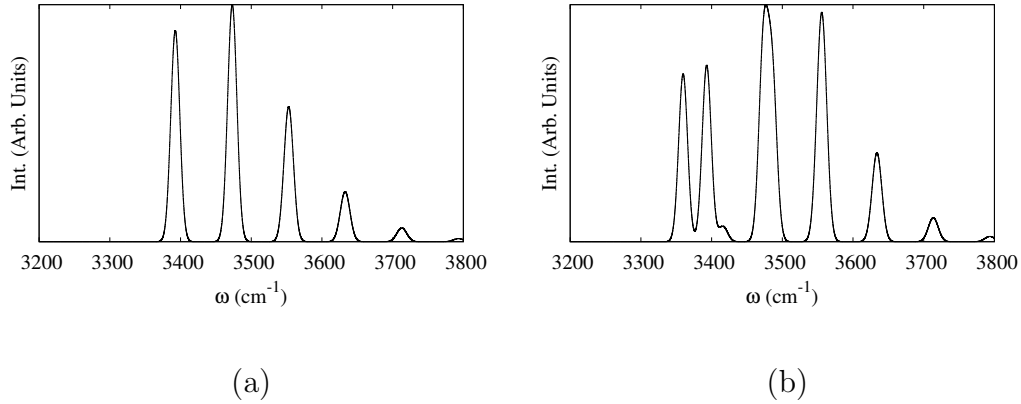
Figure 2.7: Vibrational spectra of $NO_3^- \cdot H_2O$ calculated with vibrational CI calculations employing (a) the ω_{llr} force constant and (b) the ω_{llr} and ω_{lbb} force constants. The calculations for both (a) and (b) employed scaled frequencies as described in the text.
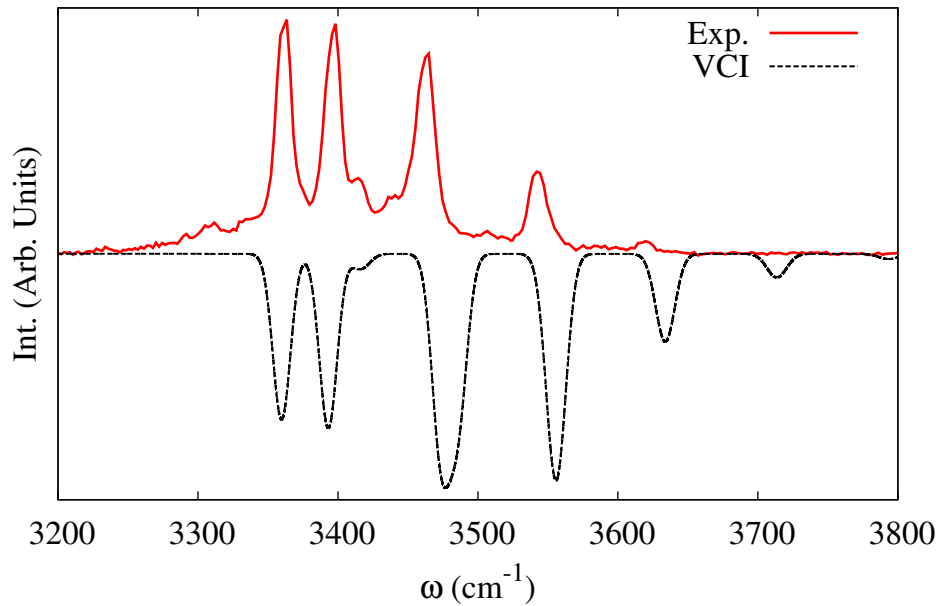
Figure 2.8: Comparison of the experimental spectrum of $NO_3^- \cdot H_2O$ at $T = 15$ K to the spectrum calculated using the vibrational CI method. The calculations include the ω_{llr} and ω_{lbb} force constants and the scaled frequencies given in the text.

31

the number of quanta in the local OH stretch, HOH bend, and rock degrees of freedom, respectively. Based on a series of exploratory calculations, the vibrational CI calculations were found to be well converged with a basis set using up to five quanta in the water OH stretch, bend, and rock modes, and up to twenty quanta in the stretch-rock progressions.

Since the strength of the Fermi resonance between the OH stretch and HOH bend overtone is strongly dependent on the values of the fundamental frequencies, scaled frequencies were employed to correct for anharmonic interactions not included in the model. The frequencies used for $NO_3^- \cdot H_2O$ are 3485 and 1700 cm^{-1} for the OH stretch and HOH bend modes, respectively. These frequencies were chosen to match the origin of the progression and to bring the bend overtone into near degeneracy with the origin of the rock progression accompanying excitation of the OH stretch fundamental of $NO_3^- \cdot H_2O$. A value of 80 cm^{-1} was chosen for the water rock frequency as that closely corresponds to the observed spacings (in the absence of Fermi resonances). The cubic force constants employed were taken from Table 2.2. All intensity was assumed to derive from the fundamental transitions.

The results of the vibrational CI calculations on $NO_3^- \cdot H_2O$ are shown in Figure 2.7. Figure 2.7a shows the vibrational spectrum obtained neglecting the Fermi resonance with the water bend overtone. This spectrum is close to that obtained with the effective Hamiltonian from the previous section, which is not surprising as the effective Hamiltonian and the CI calculations essentially contain the same physics. The spectrum obtained including the Fermi resonance with the bend overtone is reported in Figure 2.7b. The first member of the rock progression in Figure 2.7a is now replaced by a pronounced doublet. Figure 2.8 shows a direct comparison between the experimental and calculated spectra of $NO_3^- \cdot H_2O$. An interesting feature of the calculated spectrum is the appearance of a weak feature near 3415 cm^{-1}. Based on an analysis of the CI coefficients, this extra peak results from both OH stretch local modes interacting with the bend overtone simultaneously. The calculated spectrum is in good agreement with that measured experimentally in terms of the locations of the peaks. The calculations are less successful at reproducing the experimentally observed intensity distribution. This most likely reflects the need allow for the highly anharmonic nature of the rock motion associated with the ground state potential energy surface when calculating the intensities.

2.10 CONCLUSION

IRMPD spectroscopy of cryogenically-cooled water-nitrate complexes combined with anharmonic vibrational calculations reveals strong anharmonic coupling in the OH stretch region of the IR spectrum of $NO_3^-\cdot H_2O$ and its isotopologues. This gives rise to a progression in the water rock vibration, and in the case of the H_2O and D_2O complexes, there is also a strong Fermi resonance with the water bend overtone. This assignment is confirmed by effective Hamiltonian and vibrational configuration interaction calculations have been carried out to aid in assigning the observed vibrational spectra of $NO_3^-\cdot H_2O$, $NO_3^-\cdot HDO$, and $NO_3^-\cdot D_2O$. As found earlier for $HCO_2^-\cdot H_2O$, $CH_3NO_2^-\cdot H_2O$ and $CH_3CO_2^-\cdot H_2O$, the water stretch-rock coupling causes a red-shift in the origin of the rock progression. Interestingly, in the absence of this red-shift, the energy gap between the water bend overtone and the OH stretch fundamental would be too great for there to be significant mixing between the OH stretch and bend overtone. Finally, $NO_3^-\cdot H_2O$ belongs to the class of anion-water complexes with a double ionic hydrogen bond motif, which is consistent with the structures found for the $HCO_2^-\cdot H_2O$, $CH_3NO_2^-\cdot H_2O$ and $CH_3CO_2^-\cdot H_2O$ complexes. However, the adiabatic ground state rock potential is highly anharmonic in the case of $NO_3^-\cdot H_2O$.

2.11 SUPPORTING INFORMATION

2.11.1 SAPT Analysis

A symmetry-adapted perturbation theory[91] (SAPT2+3) analysis of the interaction energy of the C_{2v} and C_s forms of $NO_3^-\cdot H_2O$ was performed using the PSI4 package.[92] These calculations were carried out using Hartree-Fock-based SAPT with the aug-cc-pVDZ basis set.[85,86] In the notation of the PSI4 package, SAPT2+3 includes intramonomer correlation up to second order and intermonomer correlation up to third order. Table 2.4 reports the resulting electrostatic (ΔE_{el}), exchange (ΔE_{ex}), induction (ΔE_{ind}), and dispersion (ΔE_{disp}) contributions to the interaction energy. Exchange-induction and δHF contributions are

Component	Structure	
	C_{2v}	C_s
ΔE_{el}	-1.0	-0.98
ΔE_{ex}	0.74	0.75
ΔE_{ind}	-0.21	-0.23
ΔE_{disp}	-0.18	-0.17
$\Delta E_{Tot.}$	-0.65	-0.65
ΔE_{ct}	-0.10	-0.10

[a] using the CCSD(T)/aug-cc-pVDZ optimized geometries

Table 2.4: Energy contributions (eV) to the $NO_3^-\cdot H_2O$ interaction energy from SAPT calculations.[a]

included in ΔE_{ind}, and exchange-dispersion, induction-dispersion, and exchange-induction-dispersion contributions are included in ΔE_{disp}. Charge transfer between the two monomers is included in ΔE_{ind}. The charge transfer contributions to the interaction energies, estimated using the approach of Stone and Misquitta,[93] are quite small, being 15.0 and 16.2% of the total interaction energy for the C_{2v} and C_s structures, respectively.

2.11.2 Thermal Displacement

At low temperatures the $NO_3^-\cdot H_2O$ complex has approximately C_{2v} symmetry (DIHB). As the temperature rises the complex can access higher energy regions of the potential where the there is one hydrogen bond and one free OH stretch (SIHB). Calculations using partition functions employing harmonic vibrational frequencies and assuming the rigid rotor approximation predict that that at $T = 300$ K the high-energy minimum (right-most structure in Figure 2 of the main manuscript) has a population of about 20%. Given the higher IR intensity of the hydrogen bonded OH stretch of the high-energy isomer than for the OH stretch vibrations of

the ground state isomer, this could account for the extra structure observed in the IRMPD spectrum at $T = 300$ K.

2.11.3 Additional Frequency Calculations

Table 2.5 reports the complete set of harmonic frequencies for the $NO_3^- \cdot H_2O$ complex and its isotopologues at the CCSD(T)/aug-cc-pVDZ C_s minimum. $NO_3^- \cdot HDO$ and $NO_3^- \cdot DHO$ are viewed as separate entities. Figure 2.9 shows the adiabatic potentials from the main text recalculated at the CCSD(T)-F12b/VDZ-F12 level of theory. The potential energy curves are nearly identical to those calculated at the CCSD(T)/aug-cc-pVDZ level of theory.

2.11.4 Additional Details of the Effective Hamiltonian

In this section the derivation of the effective Hamiltonian is given. Starting with the model Hamiltonian from the main text:

$$H = H_1 + H_2 + H_r + H_c , \tag{2.17}$$

$$H_i = \frac{p_i^2}{2} + \frac{\omega_i^2 q_i^2}{2} , \quad i = 1, 2, r , \tag{2.18}$$

and

$$H_c = \frac{\lambda_1 q_1^2 q_r}{2} + \frac{\lambda_2 q_2^2 q_r}{2} , \tag{2.19}$$

where H_1, H_2, and H_r are the Hamiltonians for the OH stretch and rock modes, and H_c is the coupling Hamiltonian. p_i, ω_i, q_i and λ_i are, respectively, the momentum, harmonic frequency, mass-scaled coordinate and cubic coupling constants for mode i.

The effect of the cubic coupling on the frequencies of the OH stretch frequencies can be approximated as a first-order perturbation to the ground state energy.

$$E_i = \frac{\omega_i}{2} + \frac{\lambda_i}{2} \langle 0|q_i^2 q_r|0\rangle = \frac{\omega'_i}{2} , \tag{2.20}$$

where

$$\omega'_i = \omega_i + \frac{\lambda_i q_r}{2\omega_i} , \quad i = 1, 2 . \tag{2.21}$$

Mode	NO$_3^-$·H$_2$O	NO$_3^-$·D$_2$O	NO$_3^-$·HDO	$NO_3^- \cdot DHO$
15	3800^s	2764^s	3572^l	3798^s
14	3571^l	2592^l	2760^s	2598^l
13	1713^b	1412	1541^b	1477^b
12	1405	1343	1401	1397
11	1343	1246^b	1343	1341
10	1038	1038	1038	1038
9	825	825	825	825
8	744	702	718	703
7	703	698	702	698
6	699	542	698	588
5	337	243	255	308
4	288	224	250	247
3	198	190	194	194
2	84	76	78	82
1	38	38	38	38
ZPE	8393	6967	7707	7666

^{b} water bend frequency, ^{l} long OH stretch, ^{s} short OH stretch

Table 2.5: Harmonic vibrational frequencies (cm^{-1}) of the various isotopologues of the water-nitrate complex at the CCSD(T)/aug-cc-pVDZ level of theory.
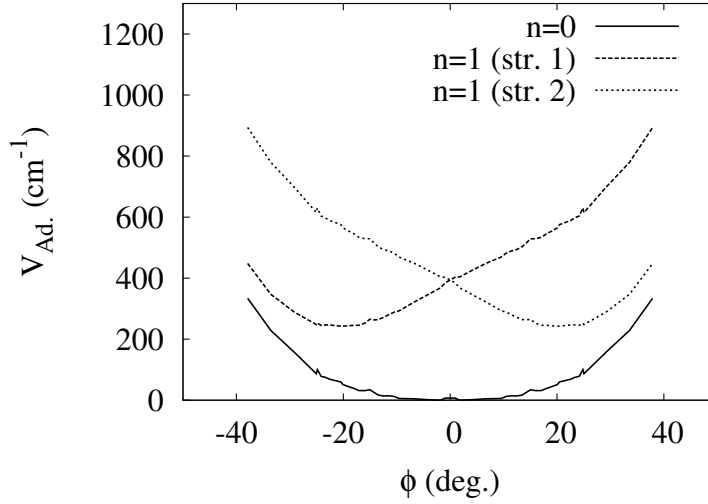
Figure 2.9: Adiabatic rock potentials for the $n_{loc} = 0$ and $n_{loc} = 1$ levels of the OH stretch modes of $NO_3^-{\cdot}H_2O$ calculated at the CCSD(T)-F12b/VDZ-F12 level of theory. The two excited state potentials are depicted in the local mode representation, and excited state potentials have been shifted downwards by 3350 cm^{-1} for convenience.

Assuming that the stretch vibrations behave as harmonic oscillators with the new frequencies ω'_i, the effective Hamiltonian becomes

$$H^{eff} = \frac{p_1^2}{2} + \frac{p_2^2}{2} + \frac{p_r^2}{2}$$
$$+ \frac{\omega'^2_1 q_1^2}{2} + \frac{\omega'^2_2 q_2^2}{2} + \frac{\omega_r^2 q_r^2}{2} \, , \tag{2.22}$$

Up to this point the derivation is the same as that found in the main text. We now continue by finding the stretch-rock potentials and deriving the transition energies. The rock potential including the OH stretch zero-point energy is given by

$$V_{r,0,0} = \frac{\omega_1}{2} + \frac{\omega_2}{2} + \frac{\lambda_1 q_r}{4\omega_1} + \frac{\lambda_2 q_r}{4\omega_2} + \frac{\omega_r^2 q_r^2}{2} \, . \tag{2.23}$$

The minimum of this potential occurs at

$$q_r^{(0,0)} = -\left(\frac{\lambda_1}{4\omega_1\omega_r^2} + \frac{\lambda_2}{4\omega_2\omega_r^2} \right) \, . \tag{2.24}$$

37

This process can be repeated to obtain the rock potential for one quanta in the first OH stretch vibration:

$$V_{r,1,0} = \frac{3\omega_1}{2} + \frac{\omega_2}{2} + \frac{3\lambda_1 q_r}{4\omega_1} + \frac{\lambda_2 q_r}{4\omega_2} + \frac{\omega_r^2 q_r^2}{2} ,$$

(2.25)

which has its minimum at

$$q_r^{(1,0)} = -\left(\frac{3\lambda_1}{4\omega_1\omega_r^2} + \frac{\lambda_2}{4\omega_2\omega_r^2} \right) .$$

(2.26)

By expanding $V_{r,n,m}$ about $q_r^{(n,m)}$, where n and m refers to the excitation level of the OH stretch local modes, and assuming that the OH stretch ground state is initially in the $n_r = 0$ level, the excitation energies are given by

$$\Delta E_1(n_r) = \omega_1 - \frac{\omega_{11r}^2}{4\omega_r} - \frac{\omega_{11r}\omega_{22r}}{8\omega_r} + n_r\omega_r ,$$

(2.27)

and

$$\Delta E_2(n_r) = \omega_2 - \frac{\omega_{22r}^2}{4\omega_r} - \frac{\omega_{11r}\omega_{22r}}{8\omega_r} + n_r\omega_r ,$$

(2.28)

where ω_{11r} and ω_{22r} are the reduced cubic coupling constants in inverse centimeter units,

$$\omega_{iir} = \frac{\lambda_i}{\omega_i\sqrt{\omega_r}} .$$

(2.29)

Eq. 2.27 reduces to

$$\Delta E(n_r) = \omega_1 - \frac{\omega_{11r}^2}{8\omega_r} + n_r\omega_r ,$$

(2.30)

when ω_{11r} and ω_{22r} are of equal magnitude with opposite signs.

2.11.5   Diffusion Monte Carlo Calculations

A B3LYP *ab initio* molecular dynamics simulation was performed for $NO_3^- \cdot H_2O$ employing the *Turbomole* package,[94] which generated 33955 geometries and their corresponding energies. The energies were then recalculated using the CCSD(T)-F12b/VTZ-F12 (F12) method in *MOLPRO*. The F12 potential energy surface (PES) was generated from fits to a permutationally invariant polynomial constructed from Morse-like terms as described by Braams and Bowman[95] and can easily be applied to dynamics or vibrational calculations.

Diffusion Monte Carlo calculations were performed using the algorithm initially described by Anderson.[96,97] The details of the simulation and our implementation can be found in our earlier studies.[50] In the present study, the DMC simulation was run with time steps of 10 atomic units for 51000 time steps with a value of α of 0.01 H. The calculated ground and excited state energies reflect the values obtained by averaging the DMC energies over the last 30000 time steps of the simulation, and taking the average of five such independent simulations. Descendent weighting was used to obtain the probability amplitude.[98] Here the simulation was started from the equilibrated ground state wave function. The DMC was run for an additional 5000 time steps. In addition, the excited state energy and wave function were obtained using the fixed-node approximation in which a node was placed in the wave function when the distances between the two hydrogen atoms in water and the closest oxygen atom in NO_3^- were equal. The other simulation parameters were the same as for the ground state. Based on these calculations, we obtain a zero-point energy (using the CCSD(T)-F12/VTZ-F12 PES) of 8361 ± 5 cm^{-1} and a rock frequency of 81 ± 5 cm^{-1}. The nature of the excited state was verified by examination of plots of the projections of the probability amplitude onto ϕ, defined in the text.

2.11.6   Additional Force Constants and Dipole Derivative Constants

A large number of force and dipole derivative constants were determined for the $NO_3^- \cdot H_2O$ complex, however, only a small number of these constants were employed in the effective Hamiltonian and VCI calculations. Tables 2.6-2.8 list the remaining force, rotational, and dipole derivative constants that are relevant to the four key vibrational modes. Table 2.7

Mode	Frequency	Mode	Frequency
ω_s	3799.85	ω_l	3571.29
ω_b	1713.01	ω_r	84.09
Type	Force Constant	Type	Force Constant
ω_{llr}	242.42	ω_{ssss}	1520.38
ω_{ssr}	-105.65	ω_{llll}	1582.00
ω_{lbb}	151.72	ω_{bbbb}	-60.07
ω_{bbr}	-16.16	ω_{rrrr}	6218.72
ω_{brr}	174.89	ω_{llss}	16.67
ω_{lss}	-189.63	ω_{ssbb}	-255.82
ω_{llb}	-298.69	ω_{ssrr}	-1969.00
ω_{sbb}	-99.33	ω_{llbb}	-308.21
ω_{bbb}	178.96	ω_{llrr}	-1516.09
ω_{sbr}	-725.26	ω_{bbrr}	763.24
ω_{lsr}	1.31	ω_{lll}	-2636.05
ω_{lsb}	-115.13	ω_{sss}	2550.51
ω_{srr}	-2087.90	ω_{rrr}	-90.79
ω_{lrr}	1752.01	ω_{lbr}	-630.76
ω_{ssb}	-258.78	ω_{lls}	-172.51

[a] short stretch (s), long stretch (l), water bend (b), and water rock (r)

Table 2.6: Harmonic frequencies, cubic, and semi-diagonal quartic force constants calculated at the CCSD(T)/aug-cc-pVDZ level of theory.[a] All values are in cm^{-1} and are unscaled.

	x	y
μ_s	0.0145738140	-0.0256012640
μ_l	-0.1182073118	-0.0304721646
μ_b	-0.1049802785	0.0131264608
μ_r	-0.0337812707	-0.1840428733
μ_{ss}	-0.0049592373	-0.0022633775
μ_{ll}	-0.0293876407	-0.0023188771
μ_{bb}	-0.0076918401	-0.0042768314
μ_{rr}	-0.0632807576	-0.0116856099
μ_{ls}	-0.0060339765	0.0016331026
μ_{sb}	0.0033594076	0.0045875584
μ_{sr}	0.0168662346	-0.0101666279
μ_{lb}	-0.0083140295	0.0025163976
μ_{lr}	0.0333614467	0.0064241828
μ_{br}	-0.0002353636	0.0079446227

[a] Molecule located in the xy plane

Table 2.7: Dipole derivative constants calculated at the C_s minimum structure at the CCSD(T)/aug-cc-pVDZ level of theory.[a]

	α	β	γ
B	0.4223	0.09055	0.07456
ζ_{ls}	0.0	0.0	0.02416
ζ_{sb}	0.0	0.0	-0.6984
ζ_{sr}	0.0	0.0	-0.3452
ζ_{lb}	0.0	0.0	-0.7049
ζ_{lr}	0.0	0.0	0.3510
ζ_{br}	0.0	0.0	0.01036

Table 2.8: Rotational and Coriolis coupling constants calculated by the *CFOUR* program at the CCSD(T)/aug-cc-pVDZ level of theory. The symbols α, β, and γ refer to the directions of motion for the asymmetric top.

lists all the dipole derivative constants that can be used in the dipole integrals at the C_s minimum. The rotational constants and Coriolis constants are listed in Table 2.8, however, these have a negligible effect on the frequencies. More force, Coriolis, and dipole derivative constants were computed for these modes, however, the constants are reported only for those that affect only the water stretch, bend, and rock modes.

2.11.7 Adiabatic potentials for $NO_3^-\cdot HDO$

The CCSD(T)/aug-cc-pVDZ adiabatic potentials were also calculated for $NO_3^-\cdot HDO$. While the ground state $NO_3^-\cdot H_2O$ potential is symmetric about $\phi = 0°$, the $NO_3^-\cdot HDO$ ground state potential has a single minimum near $\phi = -13°$. Since the excited state potential for the OH stretch mode has a minimum near $\phi = 20°$, excitations of the OH stretch involve a rearrangement of the complex.
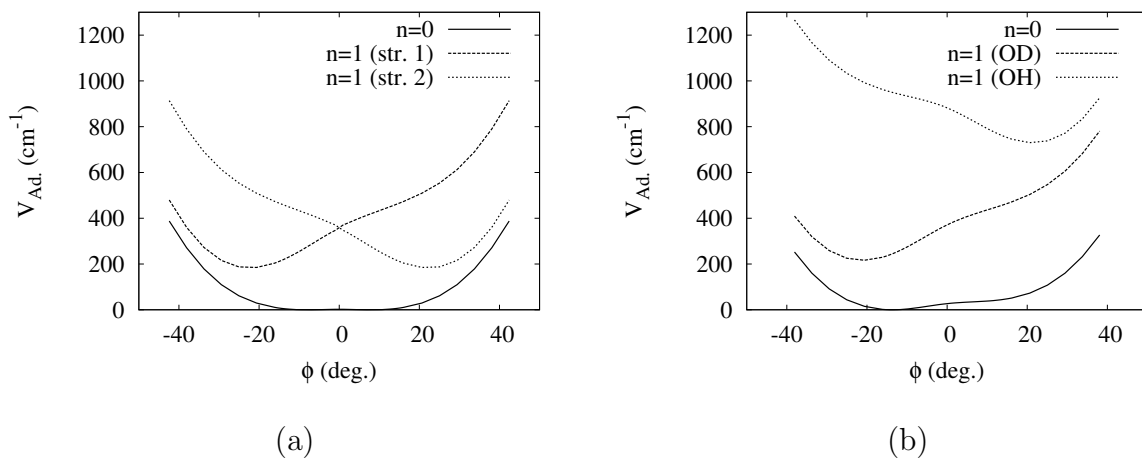
Figure 2.10: CCSD(T)/aug-cc-pVDZ adiabatic potentials calculated for (a) $NO_3^- \cdot H_2O$ and (b) $NO_3^- \cdot HDO$. The deuterated potentials show that the potential energy minima for the ground state and OH stretch are shifted away from $\phi = 0°$.

3.0 EFFECTS OF PROTON DISORDER ON THE CRYSTAL STRUCTURE OF METHANE CLATHRATE HYDRATE

3.1 INTRODUCTION

Methane hydrate has been a popular topic for scientific research in the last 100 years. Despite the large number of papers published on the topic,[99, 100, 101, 102, 103, 104, 105, 36, 37, 43, 106, 107, 108, 109, 110] many of its properties are still not well understood. Methane hydrate is of interest as a potential source of natural gas and is an important agent in climate change. From x-ray crystal structure determinations,[103, 36] it is known that methane hydrate is a type I clathrate hydrate with a cubic unit cell (Pm$\bar{3}$n) containing 46 water and 8 methane molecules. The water molecules are arranged in two small dodecahedral and six large tetradecahedral cages with the methane molecules located at the centers of the cages.

Each water molecule in methane hydrate has four neighboring waters, and, as for ice Ih, there are approximately $[(3/2)^n]$ possible structures with different proton arrangements,[10] where n is the number of water molecules in the cell. Theoretical investigations of ice have found that its structure and properties are sensitive to the order or disorder in the proton arrangement.[15, 32, 111, 30, 3, 112] For example, proton-ordered ice XI ($Cmc2_1$) has a higher thermal conductivity than proton-disordered ice Ih,[30] and some of the ice XI structures are ferroelectric.[3, 112] We expect that proton disorder can similarly impact the properties of methane hydrate.

Due to the relatively large size of the unit cell, one might expect that it is adequate to construct the supercell by replicating either the lowest energy unit cell[113] or a randomly generated unit cell. However, if a single unit cell is replicated to produce the supercell, considerable order results in the positions of the protons, which could impact the values of

the properties of interest. In order to accurately represent the bulk crystal, one has to employ large supercells that do not simply replicate the proton arrangement of the unit cell. In the following sections we explore how the structure and density of the methane hydrate crystal depend on the treatment of proton order and disorder.

3.2   COMPUTATIONAL DETAILS

3.2.1   Crystal Structure

The methane hydrate supercells were constructed starting from a bare oxygen lattice, and the coordinates of the hydrogen atoms were generated semi-randomly according to the Bernal-Fowler rules[2] using the Monte Carlo algorithm of Buch et al.[3] Two different procedures were employed to assign the hydrogen coordinates:

(i) The hydrogen positions were assigned for a single unit cell which was then replicated in all directions to produce proton-ordered crystals.

(ii) The hydrogen positions were assigned for a bare oxygen N_cxN_cxN_c supercell to produce proton-disordered supercells, where N_c is the number of unit cells in the x, y, and z directions.

3.2.2   Optimizations

To represent the interactions of the molecules in the crystal, flexible atomistic potentials were employed for water along with a single Lennard-Jones sphere for each methane molecule.[114] Three different water models were employed in the structural optimizations. The first water force field was q-SPC/FW,[12] which is a flexible variant of the SPC family of water models that was parametrized for use in path integral molecular dynamics simulations. The second water force field was TIP3P with harmonic bond and angle potentials.[7,115] The third force field was the modified central force model (MCFM),[116] which represents the atomic interactions using a pair-potential and utilizes a switching function to smoothly transition between the bonded and non-bonded regimes. For each force field the Wolf method[117] was employed with

Ordered					
Supercell #	a	b	c	$a_c^{\star}$	RMSP†
1	11.6006	11.4774	11.4264	11.5012	6.356×10^{-1}
2	11.6253	11.3576	11.5282	11.5032	9.617×10^{-1}
3	11.4983	11.7440	11.2822	11.5066	0.1640×10^{1}
4	11.6697	11.3480	11.4897	11.5017	0.1145×10^{1}
5	11.5422	11.6590	11.3263	11.5083	0.1197×10^{1}
6	11.7511	11.3995	11.3932	11.5134	0.1453×10^{1}
7	11.5620	11.4395	11.5252	11.5088	4.459×10^{-1}
8	11.5624	11.4002	11.5616	11.5078	6.629×10^{-1}
Avg.	11.6014	11.4781	11.4416	11.5069	0.1018×10^{1}
Disordered					
9	11.5048	11.4964	11.5149	11.5054	6.558×10^{-2}
10	11.4912	11.5418	11.4843	11.5058	2.226×10^{-1}
11	11.4856	11.4853	11.5471	11.5060	2.529×10^{-1}
12	11.5225	11.4990	11.4896	11.5037	1.204×10^{-1}
13	11.4310	11.5053	11.5885	11.5081	5.593×10^{-1}
14	11.5037	11.4977	11.5169	11.5061	6.993×10^{-2}
15	11.5103	11.5081	11.4998	11.5061	3.955×10^{-2}
16	11.4688	11.5362	11.5116	11.5055	2.417×10^{-1}
Avg.	11.4897	11.5087	11.5191	11.5058	1.965×10^{-1}

* $a_c = \sqrt[3]{abc}$, † Root mean squared percent deviation of a, b, and c from a_c.

Table 3.1: Lattice constants (Å) from optimizations of methane hydrate 2x2x2 supercells with different proton arrangements employing the q-SPC/FW potential.
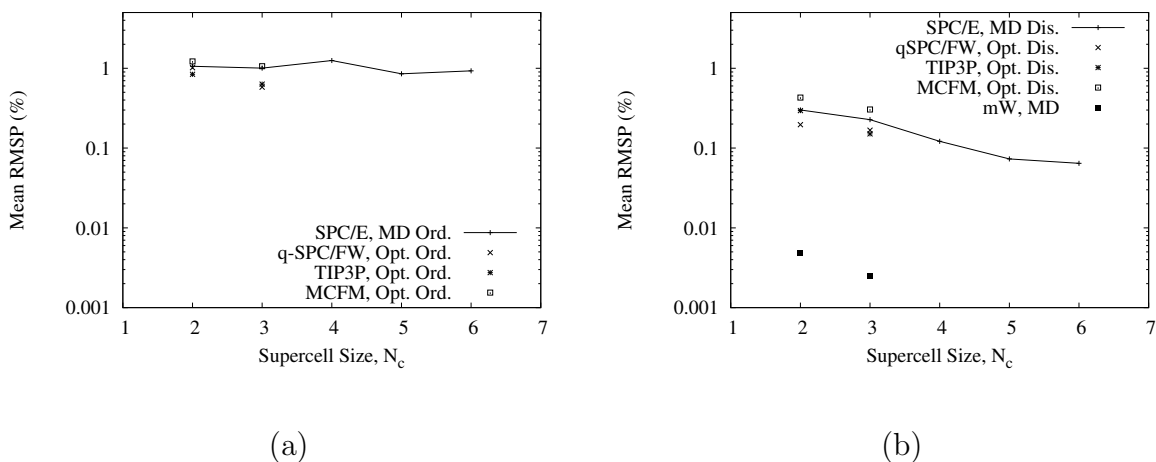
Figure 3.1: Deviations from cubic symmetry as a function of supercell size (N_cxN_cxN_c) for (a) ordered and (b) disordered supercells. The results from simulations employing the SPC/E force field have been connected with lines so that the trends can easily be seen.

a damping parameter of $\alpha = 0.20$ Å^{-1} to treat long-range electrostatics. The cutoffs for Coulomb and Lennard-Jones interactions were chosen to be 10.0 and 9.0 Å, respectively.

Both 2x2x2 and 3x3x3 supercells were used in the structural optimizations ($P = 0$ atm) using the *GULP* simulation package.[118] All optimizations allowed both the atomic positions and the three lattice constants to vary without constraints. In the determination of the optimized lattice constants, results from eight different randomly chosen supercells were used to gather statistics.

3.2.3 Molecular Dynamics

To account for thermal effects on the lattice constants, molecular dynamics (MD) simulations were carried out using the *LAMMPS* simulation package.[115] Two force fields were employed for the MD simulations, the SPC/E rigid monomer model,[119] and the coarse-grained mW model,[6,100] which does not explicitly include hydrogen atoms. MD simulations were performed in the NPT ensemble at $T = 100$ K and $P = 1$ atm using the Nosé-Hoover[57] thermostat and

barostat, with time constants set to 50 and 500 fs, respectively, and a timestep of 0.5 fs. The MD simulations were first equilibrated in a cubic box with isotropic pressure coupling for 1 ps followed by a 50 ps equilibration with anisotropic pressure coupling. The production runs were performed for an additional 50 ps after equilibration with a sampling rate of 5 fs. As for the optimizations described above, eight different supercells were employed in the molecular dynamics simulations.

3.3   RESULTS AND DISCUSSION

The lattice constants from optimizations using the q-SPC/FW potential with eight different proton-ordered and eight different proton-disordered 2x2x2 supercells are reported in Table 3.1. The table also reports the root mean square percent (RMSP) differences of the three lattice constants from that of a cubic structure with the same density, a_c

$$a_c = \sqrt[3]{abc} \; ,$$

where a, b, and c are the orthorhombic lattice constants. Calculations with and without cubic constraints show that a_c is a good estimate of the true cubic lattice constants. In the following discussion we will assume that a_c is the cubic lattice constant.

Several trends apparent upon examination of Table 3.1:

(i) The deviation of the lattice constants from those for cubic symmetry are as large as 0.2 and 0.08 Å for the ordered and disordered supercells, respectively.

(ii) The value of a_c is relatively insensitive to the arrangement of the protons and, hence, the density of the crystal is essentially unaffected by the treatment of proton disorder.

In addition to the lattice constants, the energies from the optimizations were examined, and were found to be uncorrelated with the RMSP deviation from cubic symmetry.

Figure 3.1 reports the mean percent deviations from cubic symmetry obtained from the optimizations and MD simulations with different supercell sizes. Not surprisingly, the mW model, which lacks explicit hydrogen atoms, essentially retains cubic symmetry even when small supercells are employed. The calculations using the SPC/E force field show

similar deviations from cubic structure as found with the flexible water models. The SPC/E simulations were performed on supercell sizes between 2x2x2 and 6x6x6. The simulations show that the proton-disordered supercells converge to a cubic structure as the system grows while the mean RMSP deviation of the lattice constants continue to fluctuate around a mean RMSP of ~1% for the proton-ordered supercells.

Distributions of bond lengths, bond angles, and O-O distances (not shown) were also examined for ordered and disordered orthorhombic structures as well as for structures constrained to a cubic lattice. No statistically significant differences were found between the different types of supercells, and the distributions of geometrical parameters found for methane hydrate with the q-SPC/FW potential are consistent with those found by Kuo et al. for ice.[111]

Our findings for the structural properties of ordered methane hydrate are also consistent with calculations on ice XI. An analysis of DFT optimizations of ice XI performed by Hirsch et al.[15] shows similar deviations from the ideal structure for the 16 proton-ordered supercells (average RMSP: 0.90%). Additionally the average of the ice XI lattice constants give a $c : a$ ratio consistent with experimental and other theoretical results for ice Ih.[32,120,121]

Although the scope of this study was restricted to the lattice constants and density, it is reasonable to assume that the effects of proton disorder could perturb the mechanical and thermodynamic properties of methane hydrate. Thus it is important to use proton-disordered supercells rather than replicating the structure of a particular unit cell when performing calculations on methane hydrate.

3.4   ADDITIONAL FIGURES AND TABLES

While Table 3.1 and Figure 3.1 give a reasonable overview of the results, more detailed figures and tables can be constructed. Figure 3.2 displays the lattice energy of the structures in Table 3.1 and the corresponding percent deviations from the cubic structure. While the proton-ordered structures have larger deviations from cubic symmetry, there does not appear to be any correlation between the RMSP deviation and the potential energy of the structure.

Figure 3.2: Comparison of the lattice energies and the RMS percent deviation from the cubic structure for the q-SPC/FW optimizations in Table 3.1.

Table 3.2 reports some of the largest deviations from cubic symmetry found after optimizing the structures with the q-SPC/FW and TIP3P models. Tables 3.3 and 3.4 report the average lattice constants and mean RMSP deviations from cubic symmetry for the optimizations and molecular dynamics simulations.

Type	Water Model	a	b	c	$a_c^{\dagger}$	RMS
Ord. 2x2x2	q-SPC/FW	11.4983	11.7440	11.2822	11.5066	0.188664
Ord. 2x2x2	q-SPC/FW	11.7511	11.3995	11.3932	11.5134	0.167259
Dis. 2x2x2	q-SPC/FW	11.4856	11.4853	11.5471	11.5060	0.029095
Dis. 2x2x2	q-SPC/FW	11.4310	11.5053	11.5885	11.5081	0.064362
Ord. 3x3x3	q-SPC/FW	11.5483	11.3816	11.5830	11.5040	0.087884
Ord. 3x3x3	q-SPC/FW	11.5214	11.6079	11.3959	11.5081	0.087026
Dis. 3x3x3	q-SPC/FW	11.4745	11.5674	11.4749	11.5055	0.043720
Dis. 3x3x3	q-SPC/FW	11.4652	11.5126	11.5382	11.5053	0.030235
Ord. 2x2x2	TIP3P	11.4884	11.1414	11.3412	11.3228	0.142207
Ord. 2x2x2	TIP3P	11.1514	11.3313	11.5166	11.3321	0.149065
Dis. 2x2x2	TIP3P	11.3370	11.3789	11.2602	11.3253	0.049146
Dis. 2x2x2	TIP3P	11.3921	11.2542	11.3273	11.3244	0.056339
Ord. 3x3x3	TIP3P	11.2188	11.3369	11.4253	11.3267	0.084584
Ord. 3x3x3	TIP3P	11.3246	11.1078	11.5477	11.3253	0.179596
Dis. 3x3x3	TIP3P	11.3615	11.3172	11.2972	11.3253	0.026846
Dis. 3x3x3	TIP3P	11.2979	11.3692	11.3045	11.3238	0.032186

$\dagger$ $a_c = \sqrt[3]{abc}$

Table 3.2: Optimized lattice constants of the two structures with the largest deviations from the cubic structure in the q-SPC/FW and TIP3P data sets.

Type	Water Model	a	b	c	$a_c^\dagger$	Mean RMSP
Ord. 2x2x2	q-SPC/FW	11.6014	11.4781	11.4416	11.5069	0.1018×10^1
Ord. 3x3x3	q-SPC/FW	11.5182	11.4752	11.5202	11.5045	5.796×10^{-1}
Dis. 2x2x2	q-SPC/FW	11.4897	11.5087	11.5191	11.5058	1.965×10^{-1}
Dis. 3x3x3	q-SPC/FW	11.4948	11.5139	11.5084	11.5057	1.676×10^{-1}
Ord. 2x2x2	TIP3P	11.3002	11.2806	11.3892	11.3233	8.404×10^{-1}
Ord. 3x3x3	TIP3P	11.3329	11.2804	11.3652	11.3261	6.335×10^{-1}
Dis. 2x2x2	TIP3P	11.3436	11.3247	11.3066	11.3250	2.948×10^{-1}
Dis. 3x3x3	TIP3P	11.3285	11.3280	11.3156	11.3241	1.507×10^{-1}
Ord. 2x2x2	MCFM	11.9236	12.0378	11.8503	11.9370	0.1221×10^1
Ord. 3x3x3	MCFM	11.9136	11.9494	11.9475	11.9369	0.1062×10^1
Dis. 2x2x2	MCFM	11.9263	11.9509	11.9325	11.9366	4.295×10^{-1}
Dis. 3x3x3	MCFM	11.9172	11.9442	11.9475	11.9363	3.048×10^{-1}

† $a_c = \sqrt[3]{abc}$

Table 3.3: Average orthorhombic lattice constants compared to a cubic structure. Results were obtained by averaging the properties of 8 individual optimizations.

Ordered						
Size	Water Model	a	b	c	$a_c^\dagger$	Mean RMSP
2x2x2	SPC/E	11.8291	11.6733	11.6523	11.7180	0.1060×10^1
3x3x3	SPC/E	11.7886	11.7175	11.6427	11.7161	0.1004×10^1
4x4x4	SPC/E	11.6637	11.7637	11.7211	11.7161	0.1251×10^1
5x5x5	SPC/E	11.7786	11.7426	11.6285	11.7164	8.527×10^{-1}
6x6x6	SPC/E	11.7786	11.6545	11.7183	11.7170	9.284×10^{-1}
Disordered						
2x2x2	mW	11.6899	11.6901	11.6902	11.6901	4.861×10^{-3}
3x3x3	mW	11.6902	11.6901	11.6900	11.6901	2.502×10^{-3}
2x2x2	SPC/E	11.7229	11.7077	11.7183	11.7163	3.005×10^{-1}
3x3x3	SPC/E	11.7179	11.7167	11.7161	11.7169	2.271×10^{-1}
4x4x4	SPC/E	11.7175	11.7203	11.7141	11.7173	1.216×10^{-1}
5x5x5	SPC/E	11.7169	11.7183	11.7161	11.7171	7.318×10^{-2}
6x6x6	SPC/E	11.7174	11.7168	11.7165	11.7169	6.434×10^{-2}

$\dagger \quad a_c = \sqrt[3]{abc}$

Table 3.4: Average orthorhombic lattice constants compared to a cubic structure. Results were obtained by averaging the properties obtained from 8 individual molecular dynamics simulations.

4.0 QUASI-HARMONIC THERMAL EXPANSION AND MECHANICAL PROPERTIES OF ICE IH AND GAS HYDRATES

4.1 INTRODUCTION

Clathrate hydrates are of interest as a possible source of natural gas and due to their role in climate change. Despite the large number of papers published on gas hydrates, [99,100,101,102,103,104,105,122,36,37,43,106,124,125,107,126,108,109,110] there are still many properties of these structures that are not fully understood. One of the complexities of gas hydrates, which is shared by ice Ih, is the existence of an astronomically large number of structures that differ only in the proton arrangement of the waters.

Ice Ih has a hexagonal crystal structure with four water molecules in the unit cell. While there are many other phases of ice, Ih is the most common. Based on x-ray crystal structures,[103] methane and xenon clathrates (MH and XH, respectively) are type I (sI) hydrates with body centered cubic unit cells[36] ($Pm\bar{3}n$) containing forty-six water molecules and eight of the guest species. The water molecules are arranged in two small dodecahedral and six large tetradecahedral cages with the guest species being located at the centers of the cages.

There is significant interest in the thermal and mechanical properties of gas hydrates. An accurate description of the anharmonicity and dynamics of the crystals is required to produce properties consistent with the experiments. Simulations using classical molecular dynamics (MD) include anharmonic effects, but the dynamics lack nuclear quantum effects, and hence, are not accurate at low temperatures. Harmonic lattice dynamics (LD) calculations can be performed by optimizing the structure and applying a normal mode analysis to calculate the properties of the phonons, which are treated as quantum quasi-particles. However,
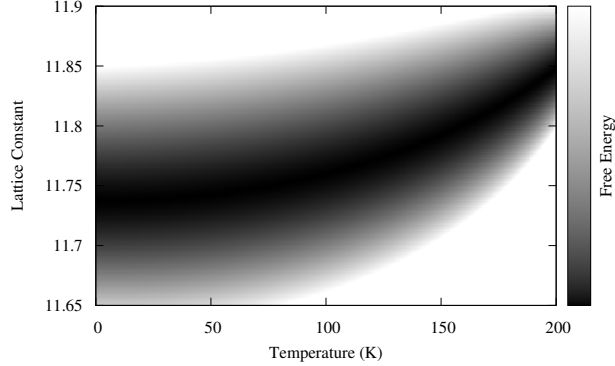
Figure 4.1: Free energy relative to the minimum value at each temperature, $F(a)\Big)_T = F(a, T)/(\min[\{F(T)\}])$.

harmonic lattice dynamics, by definition, does not treat vibrational anharmonicity. A simple method to improve the LD calculations and introduce the effects of finite temperatures is the quasi-harmonic approximation (QHA).[118,54,127] Within the QHA, phonons are assumed to be harmonic and the free energy is used to optimize the structure instead of the potential energy. Since the frequency of the phonons depends on the lattice constants, this approximation allows the anharmonicity to be included, in an effective manner, through volume and temperature dependent changes in the phonon energy and entropy.

In this work the QHA is used to determine the properties of ice Ih, MH, XH, and the hypothetical empty hydrate (EH). Results are presented for the lattice constant, speed of sound, and elastic properties as a function of temperature. These calculations serve as an important test of the approximations and water models.
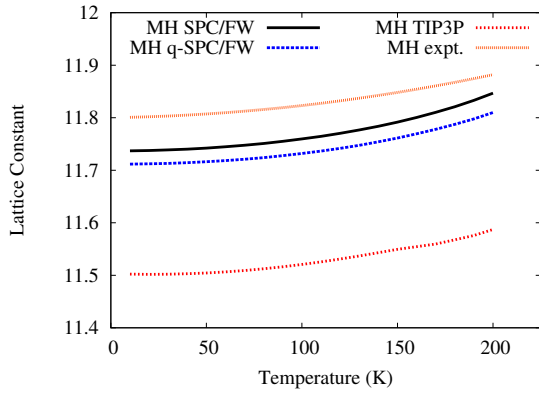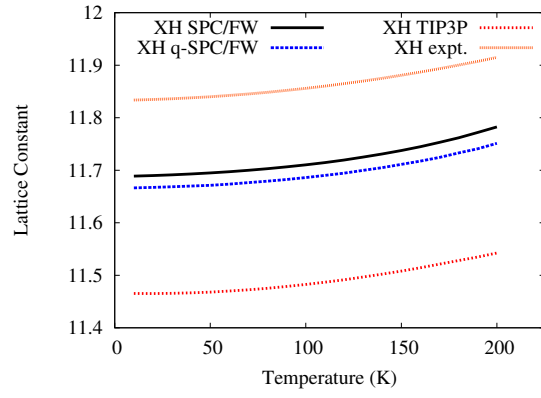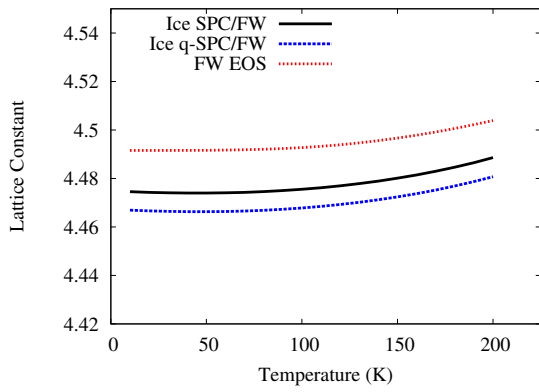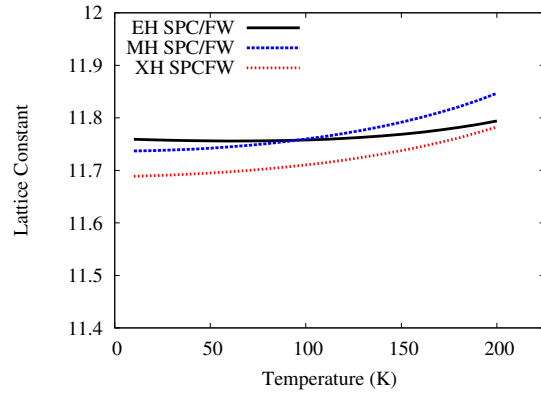
Figure 4.2: Lattice constants for (a) methane hydrate, (b) xenon hydrate, and (c) ice Ih calculated using the SPC/FW, q-SPC/FW, and TIP3P potentials within the QHA. Experimental results are also shown for MH,[43] XH[122] and ice Ih (FW EOS)[123] as well as (d) a comparison between the methane, xenon and empty hydrates. Note that the experiments were performed on the deuterated hydrates.
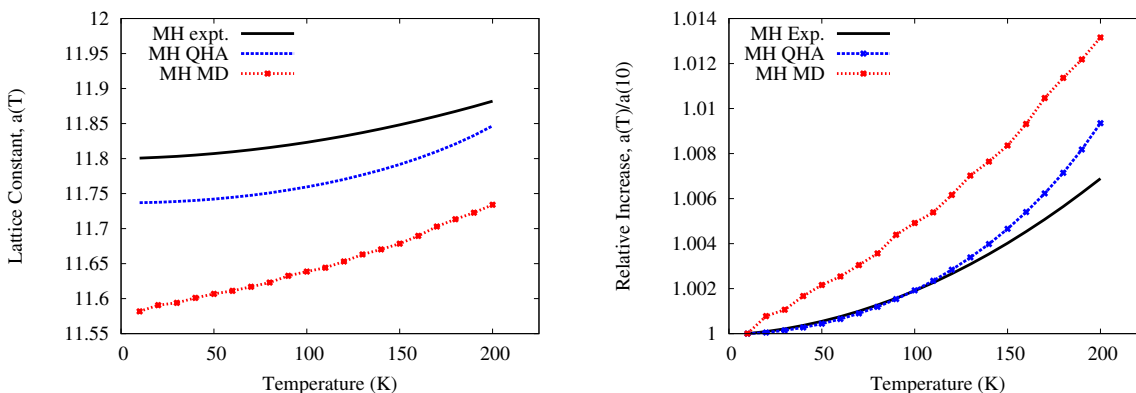
Figure 4.3: Comparison of lattice constants determined using QHA, MD, and diffraction experiments.[43] The QHA calculations show significant improvement compared to the MD simulations. The QHA and MD calculations were performed using the SPC/FW potential. The MD simulations were performed with the *LAMMPS* simulation package[115] at 0 atm.

4.2 COMPUTATIONAL METHODS

4.2.1 Crystal Structures

The gas hydrate structures used in the calculations were constructed as proton disordered 2x2x2 supercells. For ice 5x3x3 proton disordered supercells were generated from an orthorhombic structure[15] with eight water molecules in the unit cell. The sizes of the supercells were chosen so that the gas hydrate and ice structures are approximately the same size. Each cell used in the calculations started as a bare oxygen lattice, which later had the hydrogen atoms added to the structure. The positions of the hydrogens were generated semi-randomly according to the Bernal-Fowler rules[2] using the Monte Carlo algorithm of Buch et al.[3]

4.2.2 Force Fields

To represent the intermolecular interactions in the solids, flexible atomistic potentials were employed for water along with a single Lennard-Jones site for methane and xenon.[114,128,129,101]
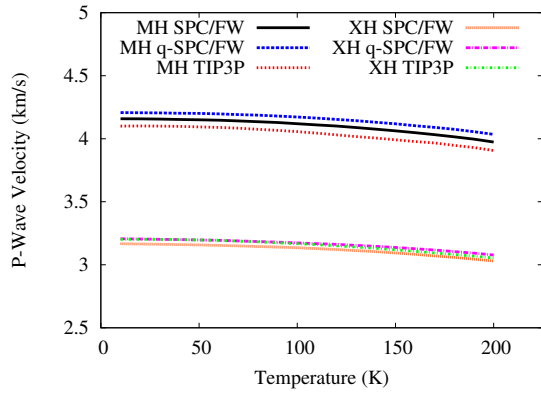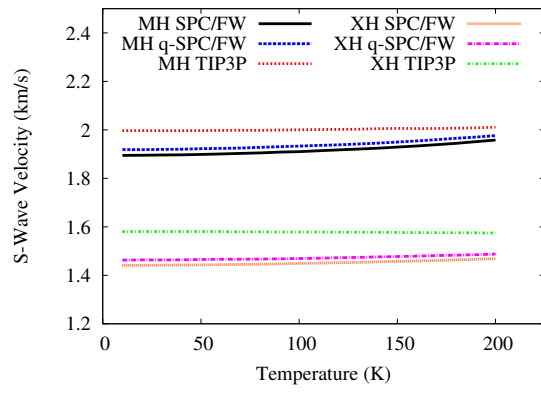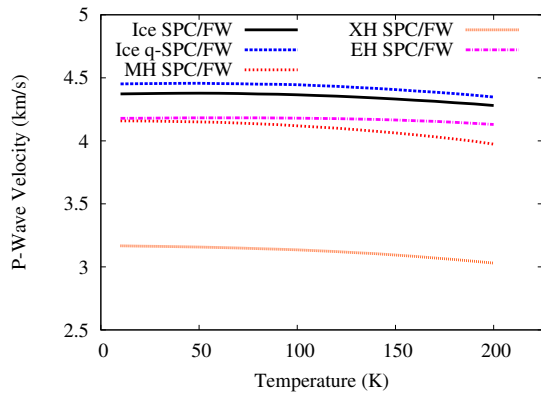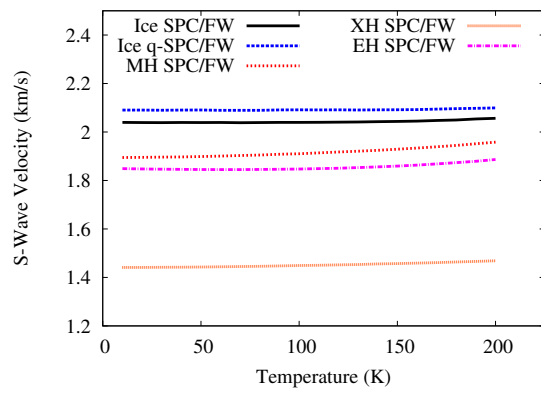
Figure 4.4: Sound speeds for ice Ih and gas hydrates calculated using the SPC/FW, q-SPC/FW, and TIP3P potentials within the QHA. Results are shown for the (a) longitudinal wave velocity of MH and XH, (b) transverse wave velocity of MH and XH, (c) longitudinal wave velocity of ice Ih compared to MH, XH, and EH, and (d) transverse wave velocity of ice Ih compared to MH, XH, and EH.
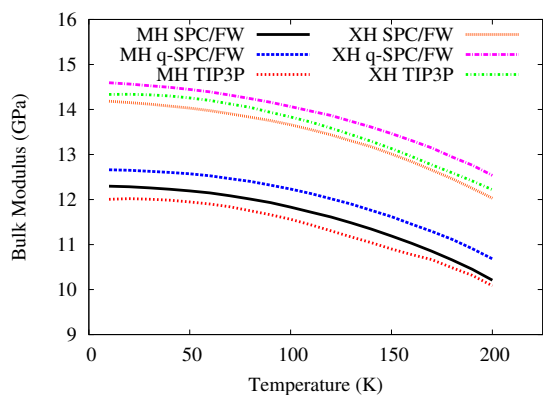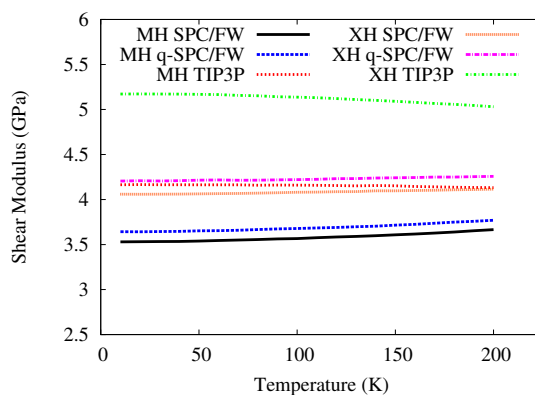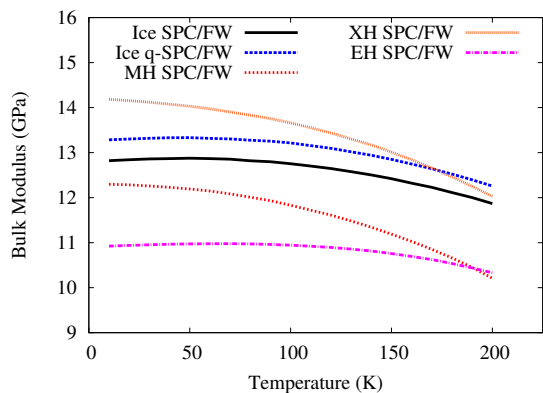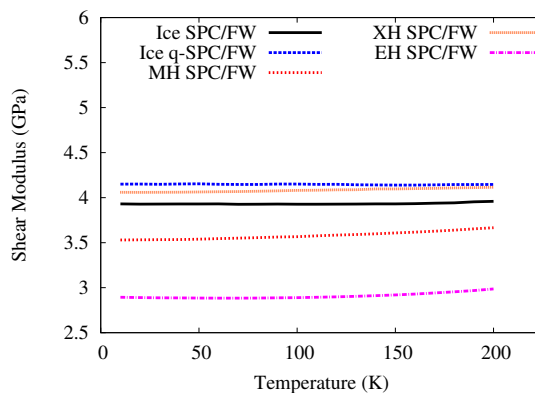
Figure 4.5: Bulk and shear moduli for ice Ih and gas hydrates calculated using the SPC/FW, q-SPC/FW, and TIP3P potentials. Results are shown for (a,b) MH and XH, and (c,d) ice Ih compared with MH, XH, and EH.
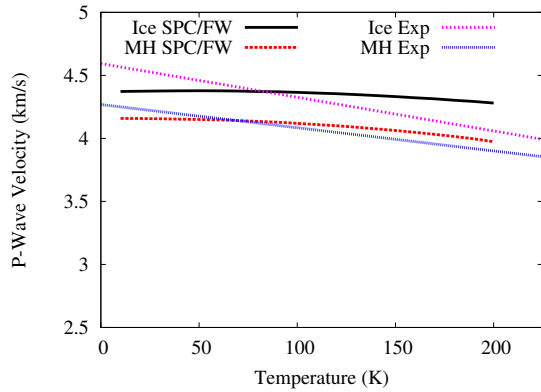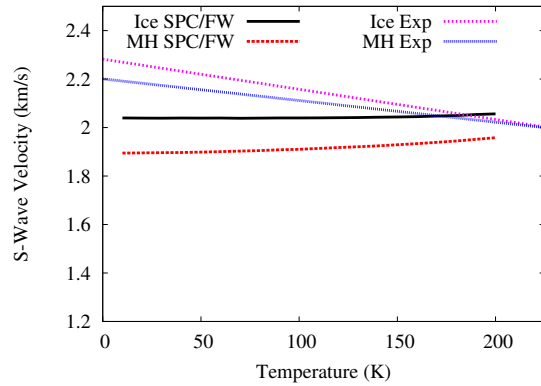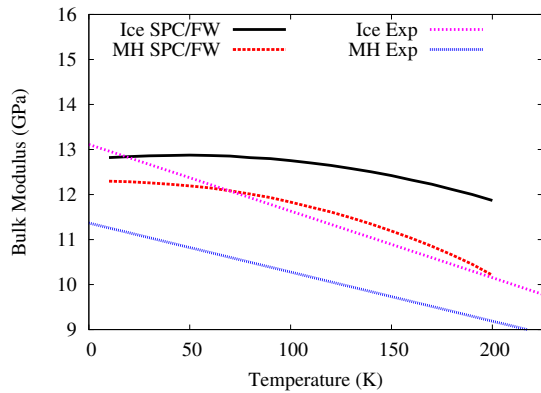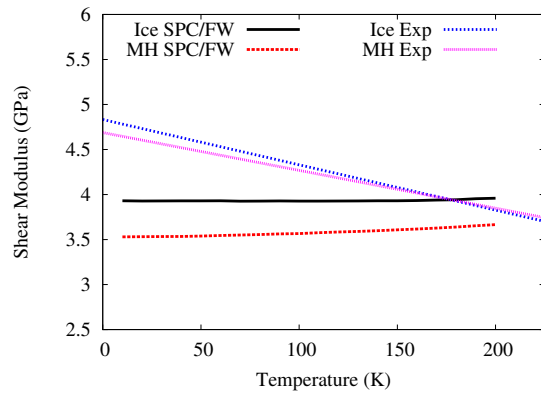
Figure 4.6: Calculated sound velocities and moduli for MH and ice Ih employing the SPC/FW potential compared to extrapolated results taken from Helgerud et al.[35] Note that the experiments were performed above $T = 200$ K.
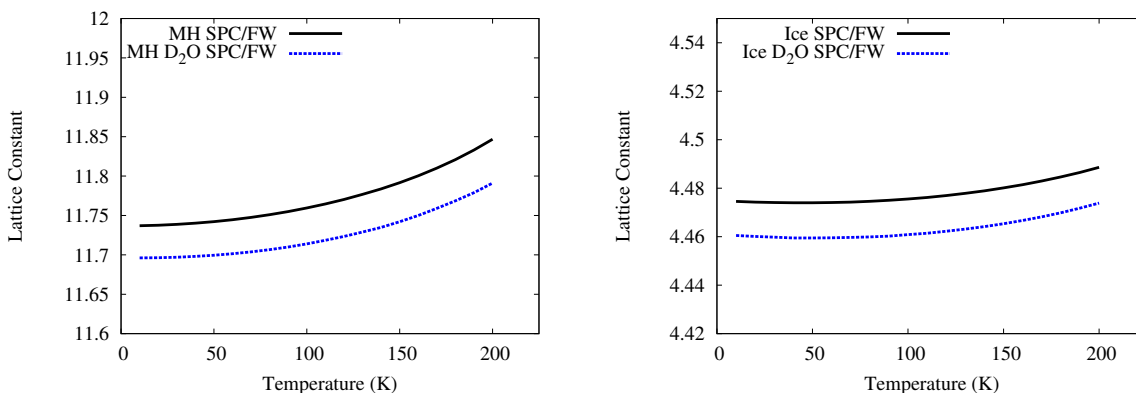
Figure 4.7: Lattice constants for the deuterated crystals calculated using the SPC/FW potential within the QHA. The deuterium substitution causes both ice and gas hydrates to contract.

Three different water models were employed in order to determine how the properties depend on the choice of empirical force field. The first water potential is a flexible variant of the TIP3P model. This model was parametrized for use with long range electrostatics, and has the constraints replaced by harmonic potentials.[115,7] In MD simulations, the use of constraints improves the thermodynamic properties by removing degrees of freedom which are frozen-out at low-temperatures. However, LD calculations include nuclear quantum effects, and hence these degrees of freedom are naturally frozen-out when flexible models are employed. The second water potential is the SPC/FW water model[9] which is a flexible variant in the SPC family of potentials. The third water model is the q-SPC/FW potential of Paesani et al.[12] This model is similar to the SPC/FW water model, but has been parametrized for use in path integral molecular dynamics (PIMD) simulations. Since LD calculations include some nuclear quantum effects, the q-SPC/FW potential is particularly appropriate. In all cases the Wolf electrostatics method[117] was applied with a damping parameter, α, of 0.20 Å^{-1} and the cutoff for Coulomb and Lennard-Jones interactions were set to 10.0 and 9.0 Å, respectively. Although, strictly speaking, force fields should be employed with the

61

same cutoffs and electrostatic methods that were employed during the parametrization, the methods described above were employed for the sake of consistency.

4.2.3 Quasi-Harmonic Lattice Dynamics

To determine the equation of state for the solids, the Helmholtz free energy was calculated on a grid of 51 different lattice constants and 40 different temperatures using the *GULP* simulation package.[118] For ice the lattice constant ranged between 4.350-4.600 Å and for the gas hydrates the lattice constant ranged between 11.45-11.95 Å. These ranges were chosen through exploratory calculations that are not reported here. The atomic positions were optimized at each lattice constant before the phonon calculations are performed. Due to the relatively small size of the supercells, a 5x5x5 grid of wave vectors was employed during the phonon calculations. The Helmholtz free energies from the grid were then fit to a 4th order polynomial, F(V,T). The resulting state equation was minimized at each temperature to determine the thermal expansion. The mechanical properties were determined using the QHA lattice constants. The properties from different proton disordered structures were weighted by the Boltzmann population of the crystal based on the zero-point corrected potential energy.

4.3   RESULTS

4.3.1   Free Energy

Figure 4.1 shows a contour plot of the Helmholtz free energy of methane hydrate as a function of lattice constant and temperature. To make the minimum of the free energy more visible, the free energy at each lattice constant and temperature was scaled by the minimum value for that temperature,

$$F(a)\bigg)_T = F(a, T)/(\min[\{F(T)\}]) , \tag{4.1}$$

where $\min[\{F(T)\}]$ is the minimum of the free energy at temperature T. Although calculations were performed on only 10 structures for each solid, Boltzmann weighting the structures leads to a single structure dominating the averages below 100 K. It is quite likely that repeating

the calculations with larger numbers of supercells would produce many nearly degenerate structures and one structure would to dominate the Boltzmann weighted averages. Despite the relatively small number of structures, the calculations were assumed to be converged since there are only slight variations in the mechanical properties of the different proton disordered structures.

4.3.2 Lattice Constants

Figure 4.2 reports the calculated cubic lattice constant of the gas hydrates as a function of temperature. The low temperature lattice constants for the SPC/FW and q-SPC/FW models are in good agreement with molecular dynamics simulations using the SPC/E force field[101] and the results are also very similar to QHA calculations performed by Shpakov et al. employing the rigid SPC force field.[43] The agreement is not surprising given that the SPC/E, SPC/FW, and q-SPC/FW are all variants of the SPC water model. In the 10-200 K temperature range all of the water models predict an increase of approximately 0.10 Å. The temperature dependence and magnitude of the increase in the lattice constant are in good agreement with the experimental results for the deuterated hydrates which start near 11.80 Å.[105, 122, 43] Compared with MD simulations which predict a nearly linear trend (see Figure 4.3), the QHA lattice constants have a quadratic trend, which improves the agreement between the LD calculations and the experiments at low temperatures. The accuracy of the QHA calculations at low temperatures is due primarily to the inclusion of nuclear quantum effects. At higher temperatures the QHA begins to breakdown and the thermal expansion is overestimated. The beginning of the breakdown of the QHA occurs at approximately half the Debye temperature, which is calculated to be between 208-213 K for methane hydrate while employing the SPC/FW potential.

Although it is difficult to see in Figure 4.2, the SPC/FW calculations predict that ice should contract up to $T = 50$ K followed by thermal expansion for the rest of the temperature range reported here. The equation of state reported by Feistel and Wagner (FW EOS)[123] shows a trend qualitatively similar to the SPC/FW results except the FW EOS lacks the thermal contraction at low temperatures. Feistel and Wagner noted that thermal contraction

is found in some experiments, however, there is significant statistical noise found in that temperature range.

At $T = 10$ K, the EH lattice constant is larger than for either MH or XH and at higher temperatures the magnitude of the thermal expansion is lowest for the guest-free hydrate. This suggests that the guest molecules both make the structure more tightly bound and strongly contribute to phonon anharmonicity. With the SPC/FW potential, both ice Ih and EH exhibit a small degree of thermal contraction at low temperatures, followed by a small amount of thermal expansion of the lattice at higher temperatures.

In addition to the calculations on the standard H_2O based crystals, calculations were also performed on the D_2O variants. The QHA calculations show that both the gas hydrates and ice Ih contract when deuterium is substituted for the hydrogen. This trend is not consistent with experimental results for ice Ih, but is consistent with theoretical results employing empirical force fields.[11] The expansion of D_2O ice Ih is a quantum effect that is not captured by LD or PIMD when empirical force fields[11] are employed in the calculations.

4.3.3 Mechanical Properties

Figure 4.4 reports the temperature dependence of the longitudinal (P-wave) and transverse (S-wave) speeds of sound for the solids. The magnitude of the P-wave velocity is in reasonably good agreement with the results of MD simulations and experiments,[101,36,37,35] and the calculations predict that the P-wave velocity should decrease with temperature. The S-wave velocity is predicted to slowly rise with temperature in calculations with the q-SPC/FW and SPC/FW force fields, while the TIP3P potential predicts that the S-wave velocity is nearly temperature independent. Figure 4.5 shows the bulk and shear moduli for ice Ih and the gas hydrates for temperatures between 10 and 200 K. The bulk modulus of ice Ih is in excellent agreement those from the QHA-LD and PIMD simulations of Ramírez et al.[44] which employed the q-TIP4P/F water model. The calculated moduli are larger than the experimental values reported by Helgerud et al.[37] and Sloan et al,[36] although the experiments were carried out at higher temperatures than the calculations reported here. While experimental results for the speed of sound and other elastic properties are sparse at temperatures below 200 K, the

results of Helgerud et al.[35] can be extended to lower temperatures using the fit to their data. The extrapolated values for the P-wave velocity and bulk modulus shown in Figure 4.6 are in qualitative agreement with the calculations within the QHA and the QHA-LD results predict reasonable magnitudes for all of the elastic properties. However, the S-wave velocity and shear modulus are predicted to rise with temperature for the SPC/FW and q-SPC/FW models, which is not in agreement with the extrapolated results from Helgerud et al. While the experimental measurements predict linear trends for the elastic properties, it should be noted that the measurements were performed on polycrystaline samples in the temperature range of 250-300 K. As found for the thermal expansion, the calculated elastic properties of EH display similar behavior as those found for ice Ih. This is not surprising since the elastic properties are affected by the "softening" of the crystal due to thermal expansion.

4.4   CONCLUSION

The lattice constants and mechanical properties of MH, XH, EH, and ice were determined from LD within the QHA. The calculations are in qualitative agreement with experimental measurements. The TIP3P force field is shown to underestimate the lattice constants for both gas hydrates and ice to a greater extent than those found while employing the SPC based potentials. The QHA-LD lattice constants of XH showed larger deviations from the experimental measurements than those calculated for MH, however, it is possible that this is due to the parameters for the the xenon Lennard-Jones potential which were determined for the gas phase Xe·H_2O system. The calculated lattice constants for all of the crystals were within 1-3% of those measured experimentally.

The QHA properties presented above show that the choice of empirical force field can have a relatively large effect on the results of the calculations. The q-SPC/FW potential is corrected for the nuclear quantum effects and accurately predicts the vibrational density of states, and hence, would be expected to give accurate results for the properties of gas hydrates. However, the rigid SPC water model used by Shpakov et al. predicts lattice constants nearly identical to the experimental results. The large variation in the temperature behavior of the

65

lattice constants and mechanical properties predicted by the SPC, SPC/FW, q-SPC/FW, and TIP3P suggests that care needs to be taken both when choosing a force field and while interpreting the accuracy of the results.

5.0 THERMAL CONDUCTIVITY OF METHANE HYDRATE AND ICE IH FROM COARSE-GRAINED NON-EQUILIBRIUM MOLECULAR DYNAMICS

5.1 INTRODUCTION

Methane hydrate (MH) is a type I (sI) clathrate with the methane molecules trapped inside water cages. The cages are arranged in a body-centered cubic lattice[103,36] (Pm$\bar{3}$n) with the unit cell being comprised of two small dodecahedral and six large tetradecahedral cages. While the heavy atoms in both ice and gas hydrates are arranged in an ordered structure, the hydrogen atoms are disordered. The unusual thermal conductivity of gas hydrates has attracted considerable interest. The thermal conductivity of ice Ih displays, over a wide range of temperatures, a T^{-1} dependence behavior typical of a crystaline solid.[30,130] Gas hydrates, on the other hand, have very low thermal conductivities with a weak temperature dependence, consistent with the behavior of amorphous materials.[106]

Many theoretical studies of the thermal conductivities of ice Ih and MH have been carried out using molecular dynamics simulations and atomistic force fields.[108,109,99,101,102] Due to the computational effort required for either Green-Kubo or non-equilibrium molecular dynamics (NEMD) calculations of the thermal conductivities relatively small supercells have generally been employed. Molinero and coworkers have demonstrated that the coarse-grained mW potential[6,100] is remarkably successful at predicting structural properties of ice and MH. The mW model represents water as a single particle that interacts via the three-body Stillinger-Weber[131] potential. The mW model has also been extended to include methane-methane, and methane-water interactions in methane hydrate.[100]

67
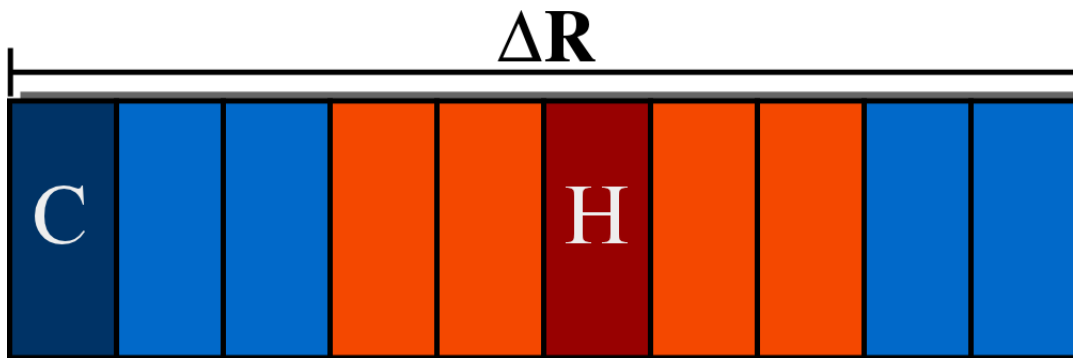
Figure 5.1: Schematic representation of the initial conditions of the simulation box. Here H and C denote the heat source and sink, respectively.

Two mechanisms have frequently been proposed to explain the low thermal conductivity of gas hydrates. One proposal is that the anomalous thermal behavior of MH is a consequence of guest-host coupling.[99, 125, 107, 126, 108, 109] An alternative proposal is that it is an inherent property of the host lattice and that the guest molecules have little or no effect on the thermal transport properties.[101, 102, 108, 109] In this paper we investigate the thermal transport mechanism in ice Ih and MH using non-equilibrium molecular dynamics simulations in conjunction with the coarse-grained mW model which allows us to use much larger simulation cells than have been employed in previous studies.

5.2 COMPUTATIONAL DETAILS

5.2.1 Structures and mW Potential

Within the mW model, the molecular interactions are described as a combination of two and three-body interactions,

$$V = \sum_{i,j} V_{ij} + \sum_{i,j,k} V_{ijk} \ , \tag{5.1}$$

68

	ϵ (kcal/mol)	σ (Å)	λ
H_2OH_2O	6.189	2.3925	23.15
CH_4-CH_4	0.340	4.08	0.0
H_2O-CH_4	0.180	4.00	0.0

Table 5.1: Parameters for the mW model as given by Molinero and coworkers.[6, 100]

where V_{ij} is the two-body potential and V_{ijk} is the three-body potential. Within the Stillinger-Weber potential the components are defined as

$$V_{ij} = A\epsilon \left[B \left(\frac{\sigma}{r_{ij}} \right)^4 - 1 \right] e^{\left(\frac{\sigma}{r_{ij} - a\sigma} \right)} , \tag{5.2}$$

and

$$V_{ijk} = \lambda\epsilon [\cos(\theta_{ijk}) - \cos(\theta_0)]^2$$
$$\times e^{\left(\frac{\gamma\sigma}{r_{ij} - a\sigma} \right)} e^{\left(\frac{\gamma\sigma}{r_{ik} - a\sigma} \right)} , \tag{5.3}$$

where $A = 7.049556277$, $B = 0.6022245584$, $\gamma = 1.2$, $a = 1.8$ is the cutoff parameter, $\theta_0 = 109.47°$ is the ideal tetrahedral angle, σ represents the size of the particle, ϵ is the well depth in the potential, and λ scales the strength of the three-body potential. The three-body term in the potential allows the particle to capture the tetrahedral structure of water while remaining computationally efficient. In the case of the methane-methane and methane-water interactions, only the two-body terms are retained in the potential. The parameters of the model are given in Table 5.1. The coarse-grained nature of this model allows for the use of large simulation boxes and long timescales.

The initial configurations were constructed based on x-ray crystal structures[103, 15] which were then equilibrated at $P = 1$ atm and temperatures between $T = 10$ and 200 K. Molecular dynamics simulations within the NPT ensemble were performed with a 1 fs timestep using the *LAMMPS* simulation package.[115] The Nosé-Hoover thermostat and barostat[57] were employed with time constants of 50.0 and 500.0 fs, respectively. In addition to ice Ih and MH, calculations were performed on the hypothetical empty hydrate (EH). The EH structures were

produced by simply removing the methane molecules from the equilibrated MH structures, which is justified by the small changes in the volume of the unit cell when the guest molecules are removed.

The basic building blocks for constructing the hydrate simulation boxes were 2x2x2 supercells which were then replicated in the long direction. The MH boxes were replicated 2-15 times while EH was replicated 2-20 times. For ice, the simulation boxes were constructed from a 5x3x3 supercell (based on an orthorhombic unit cell containing 8 water molecules[15]) which was then replicated 4-40 times in the long direction. Due to the tensor nature of the thermal conductivity, 3 simulations were performed in the x, y, and z directions for a total of 9 simulations at each temperature and box size. This procedure was used for all of the solids despite the expected isotropic behavior for the cubic hydrates. The sizes of the simulation boxes were determined by running successively larger simulations until the thermal conductivity converged. Larger simulation boxes were employed for ice and EH due to the larger magnitude of the thermal conductivity (phonon lifetimes).

5.3 PHONON PROPERTIES

For the coarse-grained potential to be useful for the determination of the thermal conductivity, it is essential that the model gives a low-frequency phonon spectrum similar to that obtained from atomistic models. To validate the phonon properties, we calculated the velocity-velocity autocorrelation functions and the phonon density of states (DOS) for the coarse-grained solids. The DOS is defined as the normalized Fourier transform the autocorrelation function,

$$\Xi(\omega) = \frac{3N \int \langle m\vec{v}(0) \cdot \vec{v}(t) \rangle e^{-i\omega t} dt}{\int \int \langle m\vec{v}(0) \cdot \vec{v}(t) \rangle e^{-i\omega t} dt d\omega} \, , \tag{5.4}$$

where Ξ is the DOS, m is the mass of the particle, $\vec{v}$ is the velocity vector, ω is the frequency, N is the number of particles, and $\langle \cdots \rangle$ indicates an ensemble average.

Atomistic MH calculations were performed with the *GULP* simulation package[118] employing the SPC/FW potential[9] for water and a single Lennard-Jones site for each methane molecule.[114] Additional details on the atomistic calculations can be found in the supporting
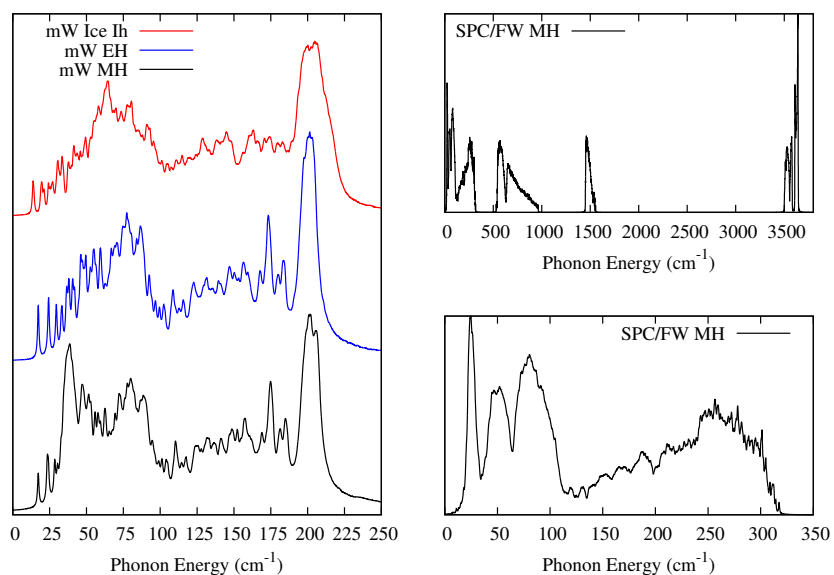
Figure 5.2: The vibrational density of states calculated at $T = 200$ K for ice Ih and methane hydrate as described by the coarse-grained and atomistic models. The SPC/FW potential and a Lennard-Jones potential are employed in the atomistic calculations for water and methane, respectively.
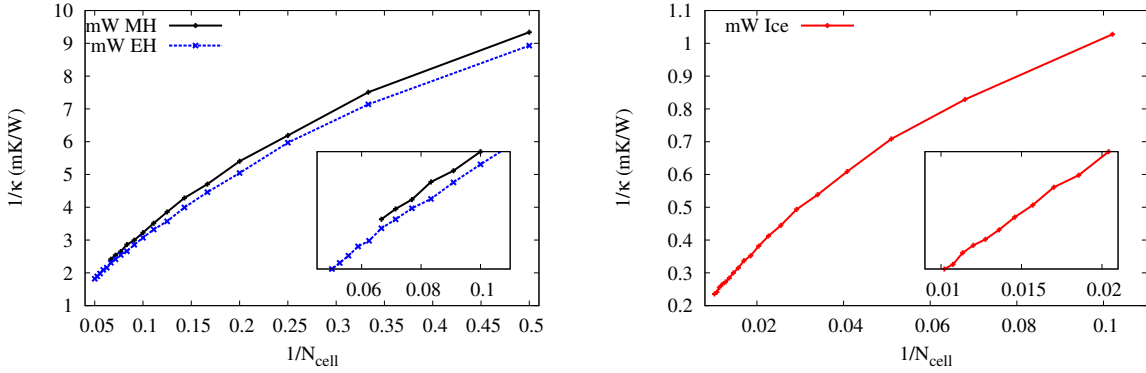
Figure 5.3: Inverse thermal conductivity plotted against the inverse length of the temperature gradient at $T = 100$ K. A strong non-linear trend can be seen when the small simulation boxes are employed. The subset of the data shown in the inserts was extrapolated to calculate the bulk thermal conductivity. The results shown for ice were taken from the simulations in the z direction.

information. The phonon spectra from the coarse-grained and atomistic models are reported in Figure 5.2. The mW potential gives a phonon spectrum of MH in reasonable agreement with that obtained using the SPC/FW model. The DOS calculated for MH and EH are very similar, although the spectrum of the fully-occupied hydrate shows the presence of additional low-frequency methane vibrations that are not observed in the EH spectrum.

5.4 NON-EQUILIBRIUM SIMULATIONS

The NEMD approach is often referred to as the "direct method" since it directly yields the properties measured in the experiments. There are several algorithms that can be utilized for calculating thermal transport properties through NEMD simulations.[59,60,61,62,63,132] A popular procedure is to apply a thermal flux and determine the average temperature gradient, while an older and less popular method is to apply a gradient and measure the average flux.
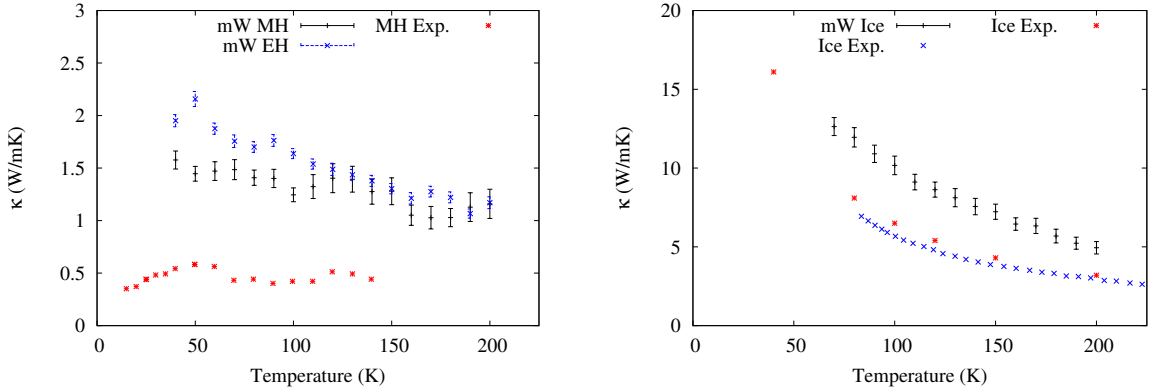
Figure 5.4: Thermal conductivity of ice Ih, methane hydrate, and the hypothetical empty hydrate as a function of temperature. Experimental results are also shown for ice ($\times^{30}$, $*^{130}$) and methane hydrate.[106]

Applying a flux is more popular due to the smaller fluctuations in the measurement of the gradient compared with the flux.[60] However, the application of a gradient is trivially easy to implement, temperature controlled, and the temperature profile can be initialized as gradient to accelerate the formation of steady-state conditions.

The NEMD simulations performed here utilized a periodic rectangular simulation box with one thermostat in the middle and one at the edge (see Figure 5.1). The temperatures in the heat source and heat sink were controlled using the Berendsen thermostat[56] with a time constant of 2.0 fs. The slab was initialized with a partial gradient by setting six regions with different temperatures then propagating the equations of motion for 2 ns. The temperature difference between the thermostats was set to 10 K and the heat flux was determined from the amount of energy added (removed) to the heat source (sink) after 14 ns. The thermal conductivity is determined from

$$J = \frac{|\Delta E_{(\pm)}|}{2\Delta t A} = \kappa \frac{2\Delta T}{\Delta R} \; , \tag{5.5}$$

and

$$\kappa_{(\pm)} = \frac{|\Delta E_{(+)}|\Delta R}{4\Delta t \Delta T A} \; , \tag{5.6}$$

where J is the heat flux, κ is the thermal conductivity, ΔT is the temperature difference between the source and sink, ΔR is the total length of the simulation box, Δt is the simulation time, A is the cross-sectional area, and $\Delta E_{(\pm)}$ is the energy added $(+)$ or removed $(-)$ by the thermostats. The factors of 2 in Eq. 5.5 account for the periodic nature simulation box where the flux is split between the two possible directions of flow and the gradient is across half of the simulation box. Due to statistical fluctuations in the thermostated regions, the values of $\kappa_{(+)}$ and $\kappa_{(-)}$ will be slightly different and this deviation reflects some of the error in the calculated thermal conductivity. In the limit of an infinitely long simulation, the two thermal conductivities will be identical.

Due to boundary scattering at the heat source and sink, the thermal conductivity from NEMD simulations is dependent on the length of the simulation boxes. To correct for the boundary scattering, the thermal conductivity must be determined for a series of progressively larger simulation boxes and then extrapolated to infinite length. The values of the thermal conductivity were obtained by extrapolating the set $\kappa_{(\pm)}^{-1}$ versus N_{cell}^{-1},

$$\frac{1}{\kappa} = \frac{\alpha}{N_{cell}} + \frac{1}{\kappa_{\infty}} \tag{5.7}$$

where N_{cell} is the number of unit cells between the source and sink, α is the slope, and κ_{∞} is the bulk thermal conductivity. Employing both the $(+)$ and $(-)$ values of the thermal conductivity allows the statistical errors of the individual simulations to be taken into account during the extrapolation procedure. Tests of the convergence of the calculations with the system size can be found in the supporting information.

5.5 SIMULATION RESULTS

Figure 5.3 reports the inverse thermal conductivity of the solids plotted against N_{cell}^{-1}. The thermal conductivities are found to have a very non-linear trend with respects to the box size, however, Eq. 5.7 assumes that the boundary scattering varies linearly with the length of the temperature gradient. In order to perform a linear extrapolation, data needs to be only taken from simulations that are sufficiently large. We have found that simulation boxes with

at least 50 unit cells between the source and sink need to be utilized for ice, while at least 10 cells need to be utilized for MH and EH. The simulation boxes used to converge the values of the thermal conductivity are much larger than those used in previous studies.[101,102] The linear regions used to extrapolate the thermal conductivity are shown in the inserts of Figure 5.3.

The thermal conductivity determined from from the NEMD simulations of MH and EH are reported in Figure 5.4a and the results for ice are are given in Figure 5.4b. For comparison, the corresponding experimental measurements are given for ice and MH.[30,106,130] Most significantly, the calculations predict the thermal conductivity to be much larger for ice than for MH. The calculations give a T^{-1} dependence in each case, although the slope is very low for MH and EH. Qualitatively, these trends are in good agreement with experimental measurements. The simulations using the mW potential overestimate the thermal conductivity for ice and MH by a factor of 2-3, however, similar behavior is found for silicon as described by the Stillinger-Weber model.[133,61,62,63] It was found previously that atomistic simulations with the SPC/E model also overestimate the thermal conductivity of MH by a factor of ~ 2, depending on the temperature. A more thorough description of the effects of coarse-graining are included in the supporting information.

The conductivity calculated for EH is found to be slightly larger than that found for MH. This suggests that the low thermal conductivity found for MH is not due only to the guest-host coupling, however, the methane-water interactions do play a role in the mechanism. Experimental measurements show that the thermal conductivity of MH is nearly constant over a wide temperature range, consistent with an amorphous material.[106] The simulations show that the thermal conductivity of both ice and MH have a T^{-1} dependence, although the slope is smaller for MH. It is possible that the neglect of the hydrogen atoms is causing the coarse-grained hydrates to behave as a crystaline solid. Earlier SPC/E NEMD simulations of MH showed an extremely weak T^{-1} dependence of the thermal conductivity.

5.6 CONCLUSION

In this work it has been demonstrated that the coarse-grained mW potential qualitatively reproduces the experimental thermal conductivity measurements for both ice Ih and methane hydrate. Larger supercells are required to obtain converged values of the thermal conductivity from the simulations than have been found to be necessary when using atomistic models. This suggests that there are important scattering processes that are lacking in the coarse-grained model.

The thermal conductivity calculations suggest that the low thermal conductivity in gas hydrates is due to the molecular structure of the gas hydrates as well as guest-host coupling. This is evident by the similar conductivities of the filled and empty hydrates and the large difference between the conductivities of ice Ih and the hydrates. The thermal conductivity is slightly higher for EH than MH, which suggests that the methane-water interaction decreases the thermal conductivity, however, the difference between EH and ice is still quite large. The vacancies in the EH crystal likely scatter phonons or cause the heat to flow around the structural cavities.

5.7 SUPPORTING INFORMATION

5.7.1 Atomistic DOS and Heat Capacity

The interactions of the crystals were represented using the SPC/FW water model[9] with a single Lennard-Jones sphere for methane. The methane-methane and methane-water interactions were modeled using the OPLS united atom potential.[114] The methane hydrate crystals were constructed as 2x2x2 supercells with the hydrogen positions assigned using the Monte Carlo algorithm of Buch et al.[3]

The lattice constants of methane hydrate at $P = 0$ atm were determined through a free energy equation of state. To determine the equation of state for the solids, the Helmholtz free energy was calculated on a grid of 51 different lattice constants (11.45-11.95 Å) and
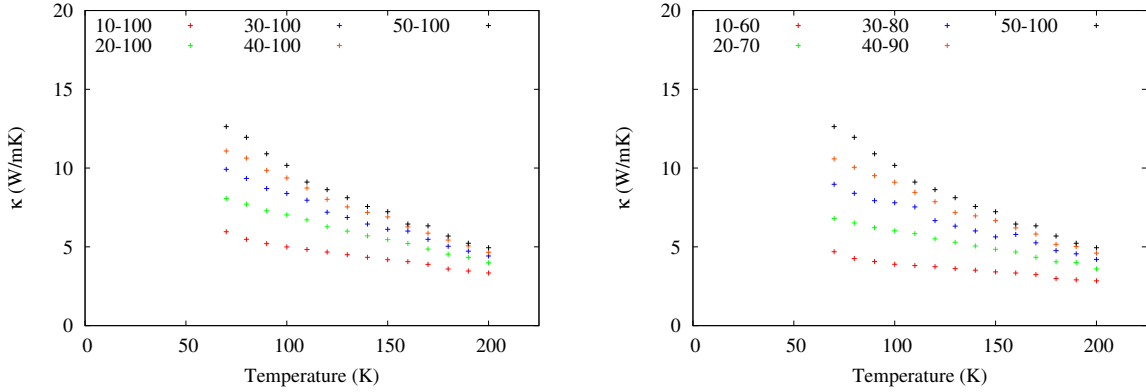
Figure 5.5: Thermal conductivity of ice determined from several different sets of system sizes. As the smallest simulations are removed, the thermal conductivity increases.

40 different temperatures (10-200 K) using the *GULP* simulation package.[118] Due to the relatively small size of the supercells, a 5x5x5 grid of wave vectors was employed during the phonon calculations. The Helmholtz free energies from the grid were then fit to a 4th order polynomial, F(V,T). The vibrational DOS and heat capacity were determined between 10 and 200 K while employing a 5x5x5 grid of wave vectors. Since lattice dynamics calculations only gives discrete harmonic frequencies, each vibrational mode was given a Lorentzian line width of 0.5 cm^{-1} and the density of states was normalized to $3N$, where N is the number of atoms in the unit cell.

5.7.2 Extrapolation Tests

To test the convergence of the non-equilibrium simulations, the extrapolation procedures were repeated for different sets of simulation data (Figure 5.5). As the smallest simulations are removed from the data set, the thermal conductivity continues to rise. It is possible that the calculations are not yet converged for all temperatures, however, the high temperature simulations are effectively converged. In addition to size effects from calculations that are not sufficiently large, it has been shown that thermal conductivity calculations can diverge if the aspect ratio is too small.[134] Figure 5.6 reports the thermal conductivity determined
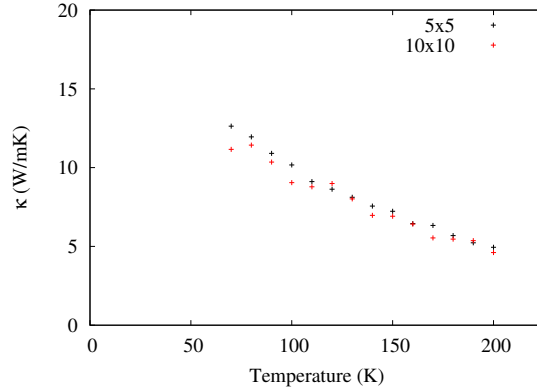
Figure 5.6: Thermal conductivity of ice calculated with different cross-sectional areas: 5x5 and 10x10 unit cells. The simulations with the lower aspect ratios show nearly the same thermal conductivity as the simulations reported in the main paper.

from simulations with two different aspect ratios. Ice simulations using a cross-sectional area of 5x5 ice unit cells and 10x10 unit cells show similar results. The 10x10 simulations show significant noise since the simulations were performed only for simulation boxes of lengths 50, 75, and 100 unit cells.

5.7.3   Mechanism Fine Details

In addition to the overestimation of the Stillinger-Weber potential, several general aspects of coarse-graining could alter the thermal conductivity. At first glance, the fact that the mW model gives reasonable results for thermal transport is somewhat surprising. It appears that the success of the coarse-grained model is partially due to cancellation of error between the reduction in the number of degrees of freedom and the neglect of nuclear quantum effects. To see why this is the case we examine a simple expression for the thermal conductivity given by[127,54]

$$\kappa \approx \frac{1}{3V} C_V \nu_{eff}^2 \tau_{eff} \,, \tag{5.8}$$

where C_V is the heat capacity, ν_{eff} is the effective velocity of the phonons, τ_{eff} is the effective lifetime of the phonons, and V is the volume. For a typical crystaline solid, the heat capacity
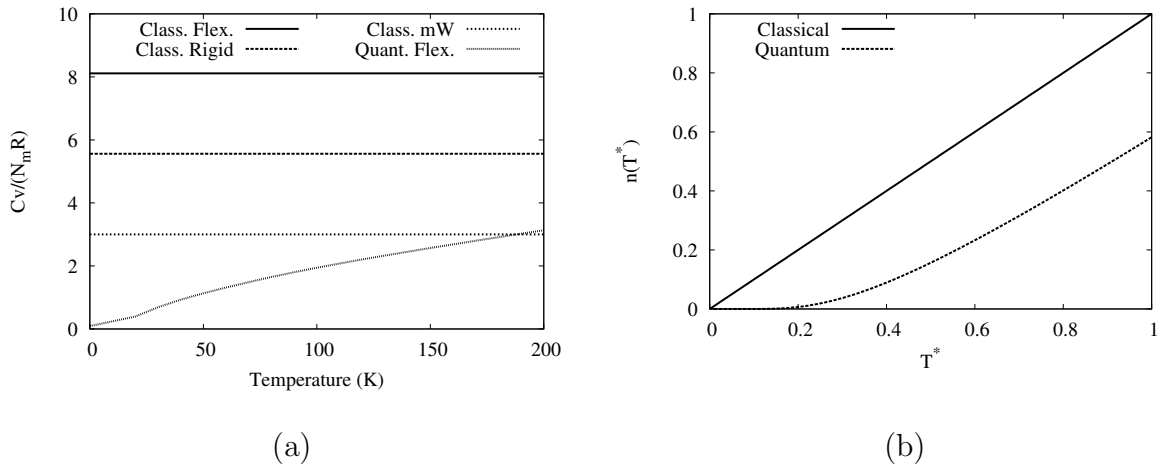
Figure 5.7: Comparison of the heat capacities for methane hydrate with classical flexible water, classical rigid water, classical coarse-grained water and quantum SPC/FW water. In all cases the methane molecule is assumed to be a spherical particle. Here N_m is the number of molecules in a unit cell. The figure on the right shows the differences between the semi-classical and quantum phonon populations as a function of reduced temperature, $T^* = kT/\hbar\omega$.

increases with temperature until it reaches the classical value of $3Nk$, where N is the number of particles and k is the Boltzmann constant. The increase in the heat capacity causes the thermal conductivity to increase as well. Meanwhile, due to anharmonic effects, the effective lifetime of the phonons decreases with temperature. These trends cause the thermal conductivity to increase with temperature up to a peak, then decrease as $\sim T^{-1}$. However, in a classical simulation the heat capacity is approximately $3Nk$ and, hence, the thermal conductivity starts at infinity and then decreases as the temperature rises. Figure 5.7a shows the classical heat capacities of methane hydrate using a fully flexible water model, a rigid water model, and the mW water model. For comparison, the figure shows the heat capacity of atomistic methane hydrate determined from vibrational calculations which are described above. These results suggest that the mW potential benefits from a favorable cancellation of error in the heat capacity. Since the thermal conductivity is approximately proportional to the heat capacity, the cancellation of error can improve the agreement between the classical and quantum regimes.

In addition to the heat capacity, Figure 5.7b reports the semi-classical,

$$n(T) = \frac{kT}{\hbar\omega} \ , \tag{5.9}$$

and quantum,

$$n(T) = \frac{1}{(exp(\hbar\omega/kT) - 1)} \ , \tag{5.10}$$

phonon populations as a function of temperature. The semi-classical population is based on the equipartition theorem, and the quantum population is the Bose-Einstein distribution. In principle, if Eq. 5.8 is to be believed, the phonon lifetimes must be lower in simulations using rigid or flexible water models to produce the correct thermal conductivity. The vibrational states of the semi-classical system are over-populated and, hence, the thermal transport due to the phonons will be overestimated unless the classical scattering rates are higher than those found in the quantum regime.

On the other hand, the mW model is missing hydrogen atoms which introduce proton and mass disorder into the atomistic simulations. The lack of disorder in the mW model causes a reduction in the number of scattering events and raises the phonon lifetimes. This effect

would presumably cause the thermal conductivity to be higher in coarse-grained simulations than in atomistic simulations when the correct phonon populations are employed.

6.0 QUALITATIVE STUDY OF THE THERMAL TRANSPORT IN GAS HYDRATES AND ICE IH

6.1 INTRODUCTION

The unit cell of type I gas hydrates consists of six tetradecahedral and two dodecahedral water cages in a cubic arrangement which enclose the guest species.[103, 36] The most important type I hydrate is methane hydrate which is of interest as possible sources of natural gas. Measurements of the thermal conductivity of gas hydrates have shown that the hydrate conductivity has an anomalous temperature dependence when compared to ice. The thermal conductivity of ice Ih behaves as a typical crystal and displays a T^{-1} dependence.[30, 130] Gas hydrates, on the other hand, exhibit low thermal conductivity consistent with an amorphous material.[106]

Theoretical studies of the thermal conductivity of gas hydrates have been conducted through classical molecular dynamics simulations employing the Green-Kubo[108, 109, 107, 102] or non-equilibrium[101, 102] formalisms. The calculations often overestimate the thermal conductivity of hydrates, however, the hydrate conductivity is calculated to be much lower than that found for ice, in qualitative agreement with experiments. Many models exist to predict the thermodynamic behavior of solids.[127, 54] The models are typically designed to represent simple elastic continuum solids or crystals with no molecular structure. While the approximations are often semi-empirical in nature and only give qualitative information, the models are an important first step towards understanding the mechanisms at play. In the following sections, we discuss the application of a simple analytic lattice dynamics model to qualitatively reproduce the thermal transport properties of ice Ih, methane hydrate (MH), xenon hydrate (XH), and the hypothetical empty hydrate (EH).
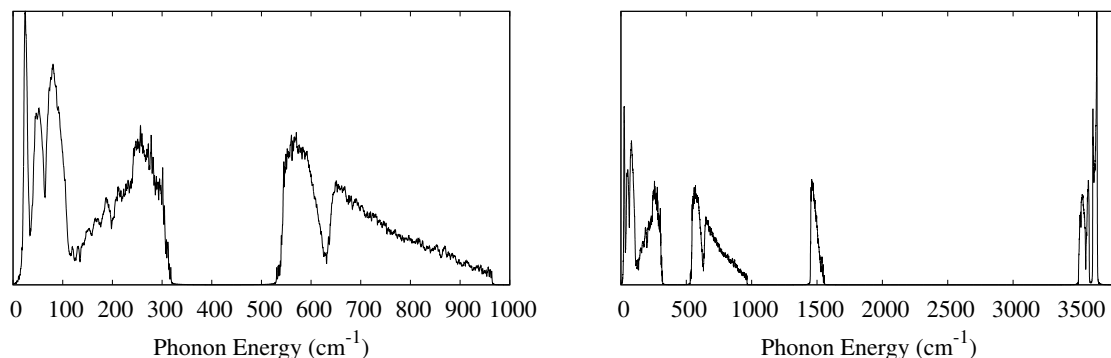
Figure 6.1: The calculated MH density of states at $T = 200$ K calculated with lattice dynamics within the quasi-harmonic approximation and using the SPC/FW force field. The DOS displays 4 distinct regions: translational (0-350), librational (500-1000), HOH bend (1400-1600), and OH stretch (3500-3700).

6.2 COMPUTATIONAL METHODS

6.2.1 Structures and Force Fields

The gas hydrate structures were constructed as proton-disordered 2x2x2 supercells, while the ice crystals were generated from an orthorhombic structure[15] to form proton-disordered 5x3x3 supercells. The positions of the hydrogens were assigned semi-randomly according to the Bernal-Fowler rules[2] employing the Monte Carlo algorithm of Buch et al.[3] The lattice constants and mechanical properties were determined through lattice dynamics within the quasi-harmonic approximation (QHA-LD). The properties were determined as a function of temperature by optimizing the Helmholtz free energy. The full details of the free energy calculations can be found in the supporting information.

The water interactions were modeled with the SPC/FW potential, which is a flexible variant of the simple point charge model (SPC). To simplify the guest-host interactions, methane and xenon were represented by Lennard-Jones spheres.[114,128,129,101] The Wolf
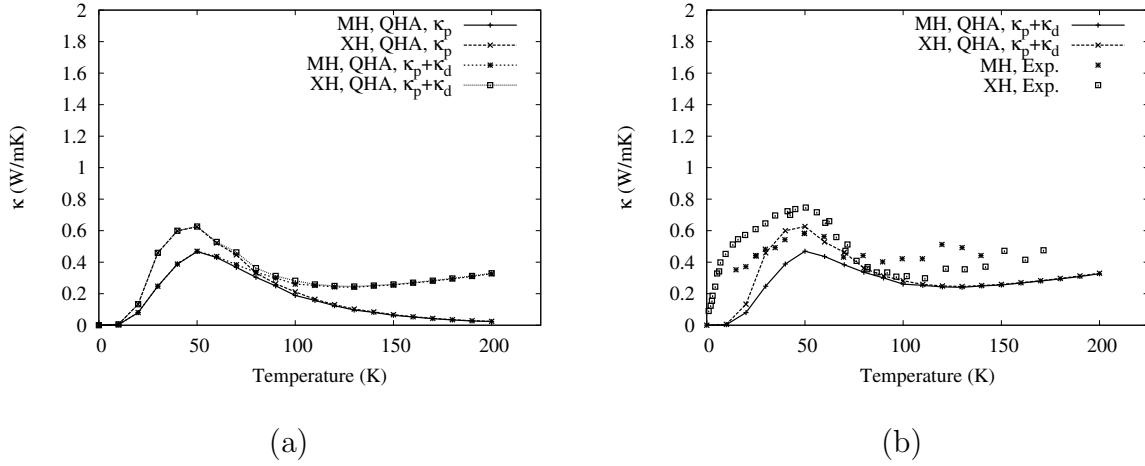
Figure 6.2: Thermal conductivity due to propagating phonons and thermal diffusion calculated for MH and XH. Results are shown for (a) the model with and without thermal diffusion, and (b) the model compared to experimental measurements.[106]
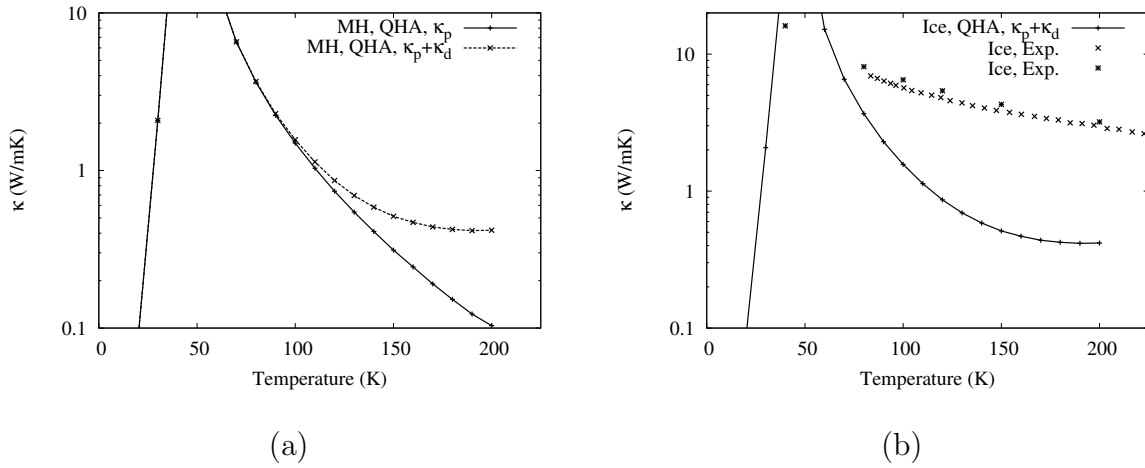
Figure 6.3: Thermal conductivity due to propagating phonons and thermal diffusion calculated for ice Ih. Results are shown for (a) the model with and without thermal diffusion, and (b) the model compared to experimental measurements ($\times^{30}$,$*^{130}$).
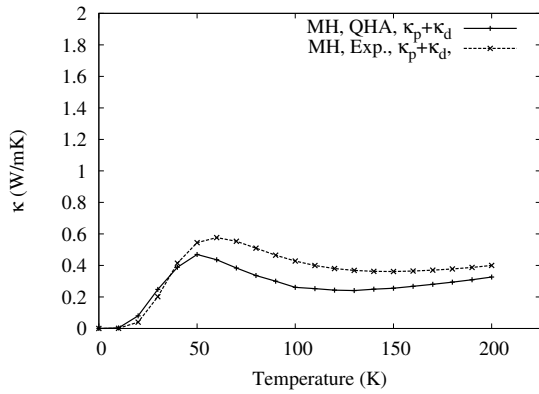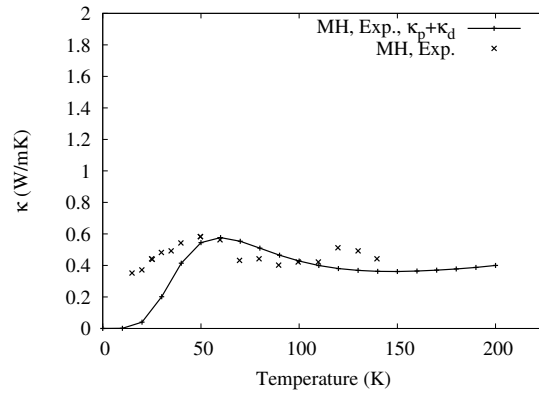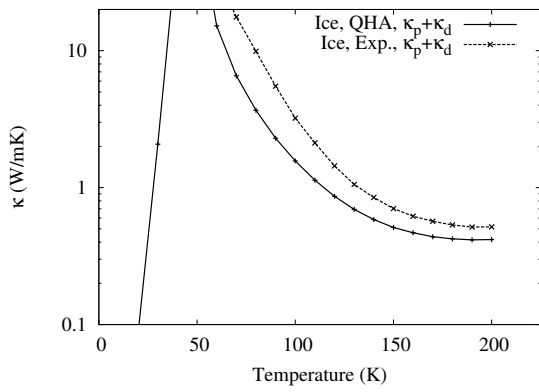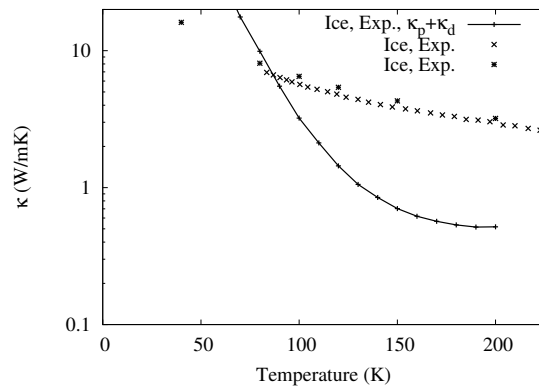
Figure 6.4: Comparison of the thermal conductivity calculated for MH and ice while employing (a) QHA lattice constants and (b) lattice constants taken from experiments (MH,[43] ice[123]).

(a)

(b)
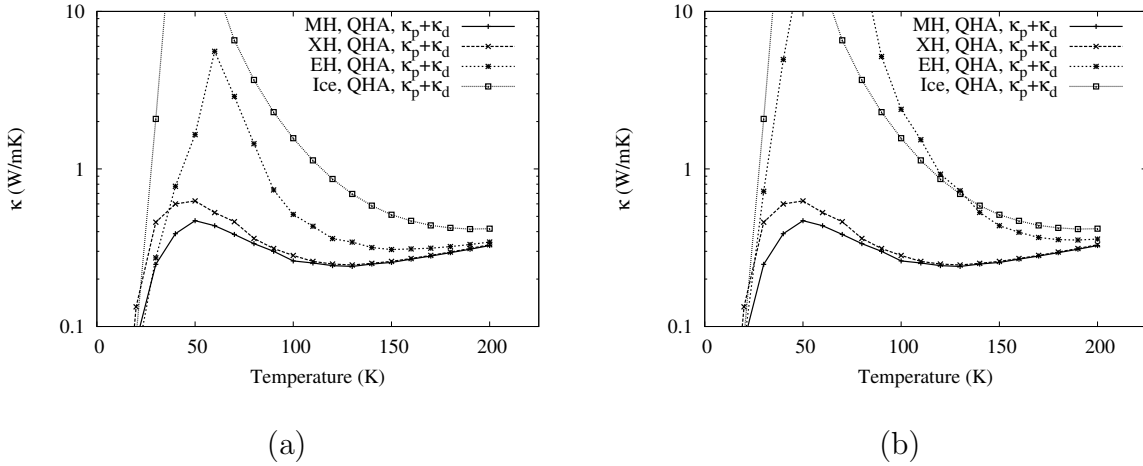
Figure 6.5: Results of the model (a) with vacancy defects for EH and (b) without vacancy defects. Assuming that each empty cage is a vacancy defect has a large effect on the thermal transport properties, however, the effect is not large enough to produce amorphous behavior.
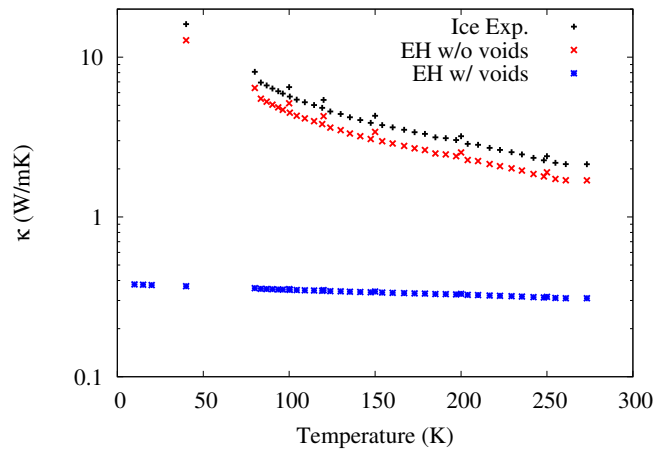
Figure 6.6: Thermal conductivity of EH modeled as an ice-like solid with void defects. The phonon scattering due to anharmonicity was estimated using the measured thermal conductivity of ice Ih and combined with the elastic properties of EH and scattering due to 3.816 Å voids.

86

electrostatics method[117] was applied with $\alpha = 0.20$ Å^{-1}, and the cutoff for Coulomb and Lennard-Jones interactions were set to 10.0 and 9.0 Å, respectively.

6.2.2 Model Density of States

As can be seen in Figure 6.1, the DOS for the hydrates is divided into roughly 4 regions. The first region contains the low-frequency acoustic modes and modes consisting of center-of-mass translations of molecules. The second region consists of the librational degrees of freedom, and the last two regions contain combinations of intramolecular bending and stretching modes of molecules. The phonon density of states (DOS) was modeled as a Debye continuum for the translational degrees of freedom combined with Einstein oscillators for the librational, water bend, and OH stretch modes.[127] This treatment only requires a Debye cutoff frequency, ω_D, and three Einstein frequencies to represent the entire DOS. The motivation for dividing the frequencies this way is to separate the propagating and non-propagating phonons in the DOS. The low-frequency vibrations are approximately center-of-mass motions of molecules which can propagate through the crystal and are represented by the Debye continuum. The high-frequency modes are motions of the hydrogen atoms which are distributed semi-randomly in the solid. The disordered nature of the hydrogens prevents the high-frequency modes from propagating effectively in the crystal and, thus, these modes only carry heat through random-walk diffusion.

The characteristic frequencies of the solids were determined from the mechanical and vibrational properties calculated within the quasi-harmonic approximation. The Debye model was used to calculate ω_D with the number of molecules replacing the number of atoms in the standard formula.[54] For the Einstein oscillators, the average frequencies were taken from each region of the gamma point DOS calculated with the SPC/FW model (Figure 6.1). While the model DOS only qualitatively resembles the atomistic DOS, the model greatly simplifies the thermal conductivity calculations discussed below.

6.2.3 Boltzmann Transport Equation

The thermal conductivity of a material can be calculated with the Boltzmann transport equation (BTE),[53,52]

$$\nu_s \nabla T \left(\frac{\partial n_t}{\partial T} \right) = \left(\frac{\partial n_t}{\partial t} \right)_{coll} , \tag{6.1}$$

$$n_t = n + n' \quad , \quad n = \frac{1}{e^x - 1} , \tag{6.2}$$

where ν_s is the speed of sound, n_t is the non-equilibrium phonon distribution function, n is the equilibrium Bose-Einstein distribution function, n' is the fluctuation of the distribution function away from equilibrium, $x = \hbar\omega/kT$, and $(\frac{\partial n_t}{\partial t})_{coll}$ represents the collisions of phonons. The collision term of the BTE can be approximated using the relaxation time approximation (RTA). Under the RTA, the n_t is expected to relax to the equilibrium distribution within a characteristic phonon relaxation time, τ,

$$\nu_s \nabla T \left(\frac{\partial n_t}{\partial T} \right) = \frac{n - n_t}{\tau} . \tag{6.3}$$

The relaxation time depends on the frequency of the phonon and the anharmonicity of the mode. The RTA-BTE can be applied to Fourier's law to calculate the thermal conductivity,[53,54,135,136,137,138]

$$\kappa \approx \frac{1}{3V} \sum_i C_V(x_i)\nu_s^2\tau(x_i) , \tag{6.4}$$

where κ is the thermal conductivity, C_V is the heat capacity of phonon i, and V is the volume. If the spacing between the phonon frequencies is sufficiently small and an analytic expression for the relaxation time is employed, the summation in Eq. 6.4 can be replaced by an integral over a classical elastic continuum.

6.2.4 Thermal Transport

The thermal conductivity was modeled using the Klemens-Callaway expression[139] combined with Einstein diffusion[140] for the high-frequency modes. The two transport components are given by

$$\kappa_p = \frac{k^4 T^3}{8\pi^2 \hbar^3 \nu_s} \int_0^{X_D} \frac{x^4 \tau(x)}{\sinh^2(x/2)} dx , \tag{6.5}$$

$$\kappa_d = \frac{k}{24a} \sum_i \frac{\sqrt[3]{N_i}\omega_i x_i^2}{\sinh^2(x_i/2)} , \qquad (6.6)$$

and

$$\kappa = \kappa_p + \kappa_d , \qquad (6.7)$$

where κ_p is the thermal conductivity due to propagating phonons, κ_d is the thermal conductivity due to random-walk diffusion, X_D is the Debye cutoff, a is the lattice constant, and N_i is the number of oscillators with frequency ω_i.

In this approximation, the diffusion is restricted to certain regions of the DOS. For instance, librational modes can transfer energy to other librational modes but not to the translational degrees of freedom. The separation of the translational, librational, bending, and stretching modes greatly simplifies the model.

6.2.5 Phonon Scattering

The scattering rates of the propagating phonons is divided into two mechanisms: inelastic Umklapp scattering and vacancy scattering,

$$\frac{1}{\tau} = \frac{1}{\tau_u} + \frac{1}{\tau_v} , \qquad (6.8)$$

where τ_u is the relaxation time for Umklapp processes[139] and τ_v is the relaxation time for scattering off of vacancies or voids in the crystal.[135, 136] In this model vacancy scattering only occurs in EH, while Umklapp scattering occurs in all crystals. The two inverse relaxation times are combined through Matthiessen's rule to determine the total inverse relaxation time.

The scattering rates are defined as

$$\frac{1}{\tau_u} = \frac{2\alpha^2 V N_a k T \omega^2}{C_V^2 B_T^2 \mu \omega_D} , \qquad (6.9)$$

and

$$\frac{1}{\tau_v} = \begin{cases} \frac{9V f \omega^4}{4\pi N_m \nu_s^3} & \text{Vacancy scattering} \\ \frac{N_{void}\pi \nu_s r_{void}^2}{V} & \text{Void scattering} \end{cases} , \qquad (6.10)$$

where μ is the shear modulus, α is the volumetric thermal expansion coefficient, B_T is the isothermal compressibility, N_a is the number of atoms in the unit cell, N_m is the number of

molecules in the unit cell, r_{void} is the radius of the voids, N_{void} is the number of voids in the cell, f is the ratio of vacancies to the number of molecules in the perfect crystal. Both ω_D and C_V are determined from the Debye model with only translational degrees of freedom. The vacancy concentration, f is zero for ice and the fully occupied MH. In the model, cavities in EH are treated as defects which can cause phonons to scatter. The anharmonic scattering term takes advantage of a high temperature approximation[139] which simplifies the equations by making Eq. 6.5 a single integral over the DOS. Unfortunately, Eq. 6.9 is not a unique expression.[137] In a more accurate treatment of the scattering, the factor of 2 would be replaced by $A\exp(-b\Theta_D/T)$, where A and b are parameters that depend on the symmetry of the crystal and Θ_D is the Debye temperature. The expression in Eq. 6.9 was chosen for simplicity and so that the treatment of cubic hydrates and hexagonal ice would be equivalent.

6.3   RESULTS

6.3.1   Thermal Diffusion

Thermal conductivity in crystaline solids is typically dominated the propagation of low-frequency phonons while transport in amorphous solids is dominated by thermal diffusion of non-propagating modes.[54,127,140] Ice and gas hydrates have ordered oxygen lattices that would support propagating phonons and a disordered hydrogen arrangement that would produce non-propagating modes. Since there is a large mass difference between the hydrogen and heavy atoms, the librational and intramolecular vibrational modes are effectively the motions of hydrogen atoms. The results of calculations with and without the thermal diffusion component are reported in Figure 6.2b. As the temperature is increased, phonon propagation rapidly deteriorates due to phonon anharmonicity. Meanwhile, the higher frequency modes start to become populated and carry heat through diffusion. The combination of the crystaline and amorphous transport causes the hydrate thermal conductivity to increase to a peak, decrease until ∼100 K, where it starts to increase again. Since the intramolecular vibrations

have very high frequencies, these modes are essentially frozen-out in the calculations, while the librational modes dominate the thermal diffusion component.

6.3.2 Comparison to Experiments

The lattice dynamics (LD) calculations for MH and XH (Figure 6.2a) display several key features of the experimental measurements. Specifically, the calculations reproduce thermal conductivity maxima near $T = 50$ K as well as the increasing thermal conductivity above $T = 100$ K. Ice Ih shares many properties with gas hydrates: The crystals have ordered oxygen lattices, similar mechanical properties, and both ice and gas hydrates exhibit proton-disorder. Thus, one would expect the solids to have similar transport properties as well. However, thermal transport in ice exhibits purely crystaline behavior while MH and XH have trends seen in both crystals and amorphous solids. Within the LD model the trends can be explained by the differences in the magnitude of the thermal expansion, which is related to the anharmonicity. Since the thermal conductivity in ice Ih is an order of magnitude larger than that found for the hydrates, the increase due to thermal diffusion is obscured by the rapid decrease of the thermal transport through propagating phonons.

6.3.3 Role of Mechanical Properties

The mechanical properties of the solids only contribute to the scattering of propagating phonons in the model. Most of the properties of MH, XH, EH, and ice Ih are strikingly similar and the thermal expansion coefficient dominates the Umklapp scattering term. Ice and EH have greatly reduced thermal expansion coefficients when compared with MH and XH. This suggests that the phonon frequencies are more nearly harmonic without the presence of the guest species. Since the thermal expansion coefficient is vital to the Umklapp scattering rate, the calculations were repeated using input from experimental measurements. Figure 6.4 compares the results of the model using lattice constants taken from either QHA calculations or experimental measurements.[43] The improvement of the results when the experimental lattice constants are employed likely highlights the breakdown of the QHA above half the Debye temperature.[118]

6.3.4 Vacancy and Void Scattering

Since the low thermal expansion coefficient causes ice Ih to have higher thermal conductivity than the hydrates, it would be expected that the low thermal expansion in EH would cause its conductivity to be similar to that found for ice Ih. However, classical simulations show that EH has a conductivity similar to that found for MH and XH.[101,102] The solution to this contradiction lies in the structure of the hydrates. Although the guests make the phonons in the hydrates more anharmonic, they also keep the entire structure filled. When the guests are removed from the clathrate structure, defects are introduced. Since phonons can scatter off of both defects and other phonons, the vacancies cause the thermal conductivity to decrease. In order for the conductivity of MH and EH to be of nearly that same magnitude, the vacancy scattering must be nearly as strong as the scattering caused by the guest-host coupling. Figure 6.5 reports the thermal conductivity calculated for all of the solids with and without vacancy defects for EH. It is clear that vacancy defects reduce the thermal conductivity, however, the effect is not strong enough to produce a thermal conductivity consistent with that found for other gas hydrates.

An alternative analysis can be performed by employing the expression for void scattering. Since the void scattering has no frequency dependence, it is essentially a constant shift in the thermal conductivity. If we assume that EH has anharmonic scattering rates similar to that for ice Ih, the thermal conductivity of EH can be estimated from experimental measurements on ice. If the heat capacity, sound velocity, and volume of ice are known, then the phonon lifetime is given by

$$\kappa_{ice} = \frac{C_V \nu_{ice}^2 \tau_{ice}}{3V_{ice}} \rightarrow \tau_{ice} = \frac{\kappa_{ice} V_{ice}}{N_{ice} k_b \nu_{ice}^2} \ . \tag{6.11}$$

For simplicity, the sound velocity and volume can be taken to be the thermal averages from the QHA-LD calculations and we will take the heat capacity to be equal to $3N_{ice}k_b$. The phonon relaxation time of ice can be combined with the expression for void scattering via Matthiessen's rule

$$\frac{1}{\tau_{EH}} = \frac{1}{\tau_{ice}} + \frac{1}{\tau_{void}} = \frac{N_{ice} k_b \nu_{ice}^2}{\kappa_{ice} V_{ice}} + \frac{8\pi \nu_{EH} r_{void}^2}{V_{EH}} \ , \tag{6.12}$$

where r_{void} is taken to be the average σ from the methane and xenon Lennard-Jones potentials, and the EH volume and sound velocity are taken to be the thermal averages from QHA-LD

calculations. The thermal conductivity of EH is then given by

$$\kappa_{EH} = \frac{N_{EH}k_b\nu_{EH}^2\tau_{EH}}{V_{EH}} \; , \tag{6.13}$$

or by grouping the constant terms,

$$\kappa_{EH} = C_1\left(\frac{C_2}{\kappa_{ice}} + C_3\right) \; , \tag{6.14}$$

where

$$C_1 = \frac{N_{EH}k_b\nu_{EH}^2}{V_{EH}} \; , \; C_2 = \frac{N_{ice}k_b\nu_{ice}^2}{V_{ice}} \; , \; C_3 = \frac{8\pi\nu_{EH}r_{void}^2}{V_{EH}} \; . \tag{6.15}$$

This analysis yields a relatively simplistic conversion from measurements of the thermal conductivity of ice to the thermal conductivity of EH. Figure 6.6 reports the EH thermal conductivity determined from Eq. 6.14. While phonon scattering due to vacancies and voids can reduce the thermal conductivity of ice to a magnitude consistent with the conductivity of gas hydrates, the scattering rates assume that the defects are positioned randomly throughout the crystal.

6.4   CONCLUSION

We have shown, through a simple lattice dynamics model, that the thermal transport in ice and gas hydrates is due to a combination of propagating low-frequency phonons and thermal diffusion through higher frequency modes. Despite the apparent differences between the behavior seen in the experimental measurements of ice and gas hydrates, the mechanism proposed here can adequately explain the observations. The thermal conductivity in ice, MH, XH, and EH can be qualitatively explained through anharmonic phonon scattering, scattering from defects, and thermal diffusion in high frequency modes.

6.5   SUPPORTING INFORMATION

6.5.1   Quasi-Harmonic Lattice Dynamics

The lattice constants of the crystals at $P = 0$ atm were determined through a free energy equation of state. To determine the equation of state for the solids, the Helmholtz free energy was calculated on a grid of 51 different lattice constants (11.45-11.95 Å and 4.350-4.600 Å for the hydrates and ice, respectively) and 40 different temperatures (10-200 K) using the $GULP$ simulation package.[118] Due to the small size of the supercells, a 5x5x5 grid of wave vectors was employed during the phonon calculations. The Helmholtz free energies from the grid were then fit to a 4th order polynomial, F(V,T). The vibrational DOS and mechanical properties were determined between 10 and 200 K. Since lattice dynamics calculations only give discrete frequencies, each vibrational mode in the DOS was broadened with a Lorentzian line width of 0.5 cm^{-1} and the DOS was normalized to $3N$, where N is the number of atoms in the unit cell.

6.5.2   Characteristic Frequencies

The Debye cutoff frequency was determined with the standard formula[54]

$$\omega_D^3 = \frac{6\pi^2 v_s^3 N_m}{V} \ ,$$

(6.16)

where v_s is the speed of sound, V is the volume of the unit cell, and N_m is the number of molecules in the unit cell. The number of molecules is employed in the formula so that the Debye continuum only includes frequencies translational degrees of freedom. The frequencies of the Einstein oscillators were determined by calculating the average frequency in the three high energy regions of the DOS between $T = 10$-200 K. The three Einstein oscillator frequencies were assumed to be constants in the model.

7.0 SUMMARY OF THE DISSERTATION

7.1 CONCLUSION

In this dissertation, the vibrational and thermodynamic properties of the water-nitrate complex, methane hydrate, xenon hydrate, and ice Ih have been discussed. Chapter 2 examines anharmonic coupling between the OH stretch and water rock degrees of freedom in the $NO_3^-{\cdot}H_2O$ complex. Effective Hamiltonian and vibrational configuration interaction calculations confirm that the IRMPD spectrum of the dimer displays a Frank-Condon-like progression in the water rock mode built on top of the OH stretch fundamental. Additionally, the analysis shows that a Fermi resonance between the OH stretch fundamental and the water bend overtone causes the first member of the progression to split into a strong doublet, in the $NO_3^-{\cdot}H_2O$ and $NO_3^-{\cdot}D_2O$ isotopologues.

In Chapter 3 it is shown that the proton arrangement in gas hydrates can perturb the structure of the crystal. The lattice constants of proton-ordered methane hydrate deviate from the observed cubic symmetry by approximately 1%, independent of the size of the supercell. While this effect is relatively small, the lattice constants of proton-disordered methane hydrate converge to cubic symmetry as the size of the supercell is increased. Chapter 4 examines the properties of methane hydrate, xenon hydrate, empty hydrate, and ice Ih through quasi-harmonic lattice dynamics calculations. The thermal expansion and elastic properties of the solids determined using the QHA-LD approach are in qualitative agreement with experiments and show that the phonons have more anharmonic character in the methane hydrate and xenon hydrate than those in either empty hydrate or ice Ih.

In Chapter 5, the results of coarse-grained non-equilibrium molecular dynamics simulations are reported for methane hydrate, empty hydrate, and ice Ih. While the thermal conductivity

of all three solids exhibits a T^{-1} dependence consistent with crystaline solids, the coarse-grained model reproduces the large difference in the magnitude of the thermal conductivity of gas hydrates and ice. Finally in Chapter 6, the thermal transport mechanism in methane hydrate, xenon hydrate, empty hydrate, and ice Ih is examined by employing a simplified phonon density of states combined with analytic scattering approximations. The analytic model suggests that in all four solids the low-frequency phonons produce a crystal-like T^{-1} dependence of the thermal conductivity combined with thermal diffusion through the the librational degrees of freedom.

7.2   NOTES ON THE METHODS

While performing calculations on complex system, approximations are required to make the equations tractable. I comment here on the algorithms and parameters employed during the coarse-grained NEMD simulations. The coarse-grained NEMD simulations were initially intended to be a tool to compare different approaches for the calculation of the thermal conductivity (e.g. coarse-grained lattice dynamics, NEMD, and Green-Kubo simulations). However, the early success of the NEMD simulations and the observation of strong size effects lead to a full investigation of the thermal conductivity employing the coarse-grained model. Since the size effects were first observed during tests of the computational methodologies, some less common algorithms and simulation parameters were employed in the simulations. For example, the time-constant of the Berendsen thermostat at the heat source and sink was taken to be 2 fs. This extremely fast relaxation rate of the thermostat was employed while trying to reduce the error bars on the extrapolated data, however, the effect of the time-constant was not fully tested in the simulations. It is possible that a larger time-constant (weaker coupling between the system and bath) would have produced different results. It should be noted that the simulation boxes ranged from ~40-1000 Å in length, while only ~7 Å was included in the thermostated regions. Hence, the thermostats affected only small portions of the whole simulation boxes.

The use of two thermostats in the NEMD simulations can introduce statistical noise into the calculated thermal conductivities. The preferred method for NEMD simulations (Reverse NEMD, RNEMD) involves the application of a fixed thermal flux and the measurement of the temperature gradient. RNEMD reduces the error present in the measurement of the thermal conductivity by measuring a property that is essentially constant at steady-state (the temperature gradient) and applying the flux. However, the system is initialized at a uniform temperature and the system must form the steady-state temperature gradient before data can be collected. One of the objectives of the NEMD method comparisons was to determine if efficient simulations could be performed by initializing the non-equilibrium simulation box with a temperature gradient to reduce the computational cost of reaching the steady-state. Since the early NEMD simulations produced promising results, this approach was used in the subsequent calculations.

7.3   FUTURE WORK

The research presented in this dissertation suggest several directions for future study. For example, would be instructive to recalculate the vibrational spectrum of $NO_3^- \cdot H_2O$ employing a more accurate potential energy surface (PES). The vibrational CI and effective Hamiltonian approaches employed in this dissertation utilized only a small subset of the anharmonic force constants and a wave function based on a harmonic oscillator reference. The full PES (see Appendix A) could be utilized in diffusion Monte Carlo simulations or CI calculations based on a vibrational self-consistent field (VSCF) reference wave function.

The calculations of the thermal conductivity of gas hydrates and ice can be improved by performing anharmonic lattice dynamics calculations and atomistic NEMD simulations. Lattice dynamics calculations would aid in deciphering the thermal conductivity mechanism by identifying individual phonons with long relaxation times (large contributions to the thermal conductivity). By comparing the results of anharmonic lattice dynamics to atomistic NEMD simulations with flexible water models and the coarse-grained NEMD simulations

presented in this dissertation, the fine details of the thermal conductivity mechanism should become clear.

APPENDIX A

AB INITIO WATER-NITRATE POTENTIAL ENERGY SURFACE

A.1   ACKNOWLEDGEMENTS

This chapter describes unpublished work performed in collaboration with Dr. Daniel Schofield (a former Jordan group post-doctoral fellow, currently a professor at Seattle Pacific University) and Alan Nichol in the Csányi group at Cambridge.

A.2   INITIAL B3LYP AND CCSD(T)-F12 SURFACES

B3LYP/6-31+G(d) Born-Oppenheimer molecular dynamics simulations were performed for $NO_3^-{\cdot}H_2O$ employing the *Turbomole* package.[94] The simulations were performed within the microcanonical (NVE) ensemble using five different starting geometries. The trajectory was sampled every 10 timesteps, which produced a data set containing 33955 geometries and their corresponding energies. After removing duplicate structures, 31442 single point energy calculations were performed at the CCSD(T)-F12b[88]/VTZ-F12[89] (F12) level of theory in *MOLPRO*.[90] The potential energy surface (PES) was generated by fitting a permutationally invariant polynomial constructed from Morse-like terms as described by Braams and Bowman.[95] As in Chapter 2, the distortion from C_{2v} symmetry is examined by defining the angle, ϕ, between the vectors bisecting the HOH angle of the water molecule and the ONO angle of the nitrate ion. The vectors are oriented so that the angle between them is $0°$ for the C_{2v}

Mode	$NO_3^-\cdot H_2O$	$NO_3^-\cdot D_2O$	$NO_3^-\cdot HDO$	$NO_3^- \cdot DHO$
15	3768	2742	3699	3766
14	3700	2683	2739	2690
13	1710	1441	1518	1501
12	1434	1373	1427	1425
11	1374	1247	1373	1372
10	1062	1062	1062	1062
9	830	829	829	829
8	735	720	720	720
7	720	715	716	716
6	716	537	672	634
5	369	265	292	309
4	246	203	221	219
3	194	186	190	189
2	38	37	37	38
1	29	26	27	27
ZPE	8462	7033	7761	7749

Table A1: Harmonic vibrational frequencies (cm^{-1}) of the isotopologues of the water-nitrate complex at the CCSD(T)-F12/VTZ-F12 surface level of theory.

structure. Geometry optimizations employing the F12 surface predicted a structure with $\phi \approx 4°$, which is much lower than the angle predicted at the CCSD(T)/aug-cc-pVDZ level of theory using analytical gradients.

Diffusion Monte Carlo calculations employing the fit surface (see Chapter 2) identified 212 geometries with energies thousands of wavenumbers below the *ab initio* global minimum of the complex. The geometries of the molecules at these "bad points" were essentially atomized. Table A1 reports the harmonic frequencies of the water-nitrate isotopologues calculated using the F12 surface. The most of the frequencies and the ZPEs are in good agreement with those calculated at the CCSD(T)/aug-cc-pVDZ level of theory (Table 2.5), however, the OH stretch and water rock frequencies are significantly different due to the above-mentioned change in the ϕ angle.

A.3   AUGMENTATION OF THE SURFACE

The geometry and vibrational frequencies calculated using the F12 surface were in good agreement with those obtained at the B3LYP/6-31+G(d) level of theory. However, the geometry and key vibrational frequencies differ appreciably from the results obtained analytically at the CCSD(T)/aug-cc-pVDZ level of theory. To ensure that the F12 calculations were predicting the correct structures, additional single point energy calculations were performed based on optimized geometries from different levels of theory, walks along the vibrational modes, the "bad points", and random geometries near the stationary points. A total of 4943 geometries and energies were added to the F12 surface, however, the predicted geometries and frequencies were essentially unchanged. To further test the accuracy of the F12 surface, an alternative F12 surface was fit using only the 4943 new data points. Surfaces fit with the original 31442 F12 data points, only the 4943 extra data points, and the total 36385 data points produced nearly identical geometries and frequencies. The geometry optimizations and frequency calculations employing the augmented F12 surface confirm that the F12 surface is very accurate near the potential energy minimum.

Method	r_1	r_2	Δr	ϕ	ω_r	ω_b	ω_l	ω_s
B3LYP/6-31+G(d)[a] Surf	2.71	2.84	0.13	4.36	38	1744	3601	3684
B3LYP/aug-cc-pVDZ	2.58	3.06	0.48	15.82	50	1700	3490	3809
B3LYP/aug-cc-pVTZ	2.58	3.09	0.50	16.50	73	1701	3486	3807
B3LYP/aug-cc-pVQZ	2.59	3.05	0.46	14.88	89	1708	3514	3814
B3LYP/aug-cc-pV5Z	2.59	3.06	0.47	15.29	-	-	-	-
MP2/6-31+G(d)	2.74	2.86	0.12	3.87	41	1768	3647	3723
MP2/aug-cc-pVDZ	2.56	3.03	0.48	15.68	89	1700	3522	3828
MP2/aug-cc-pVTZ	2.56	3.00	0.44	14.49	81	1699	3539	3831
MP2/aug-cc-pVQZ	2.58	2.92	0.34	11.05	66	1703	3596	3828
CCSD/aug-cc-pVDZ	2.59	3.05	0.46	15.05	86	1727	3621	3851
CCSD(T)/aug-cc-pVDZ	2.58	3.00	0.41	13.50	88	1713	3567	3800
CCSD/aug-cc-pVTZ[b]	2.60	2.99	0.39	12.86	78	1731	3664	3865
CCSD(T)/aug-cc-pVTZ	2.59	2.92	0.33	10.80	-	-	-	-
CCSD(T)-F12/VDZ-F12	2.64	2.84	0.21	6.80	22	1717	3666	3796
CCSD(T)-F12/VTZ-F12 Surf	2.68	2.79	0.11	3.58	35	1710	3700	3768

[a] Calculated with *Turbomole*, [b] Calculated with *CFOUR*

Table A2: Comparison of the geometries and frequencies calculated at different levels of theory. The geometries are specified by the hydrogen-nitrogen distances (r_1 and r_2), the difference between them ($\Delta r = |r_1 - r_2|$), and the ϕ angle. The geometry optimizations were performed with the *MOLPRO* package except where otherwise noted.

It should be noted that calculations performed with a small basis set, such as 6-31+G(d), predict a nearly C_{2v} geometry for the $NO_3^- \cdot H_2O$ complex while calculations with larger aug-cc-pVnZ (n=D,T,Q) basis sets predict a more highly distorted structure. However, in comparing calculations employing the surfaces and *ab initio* methods, it became clear that there is a strong basis set dependence and that the structure of the complex would have C_{2v} symmetry in the complete basis set limit (Table A2).

A.4 GAUSSIAN APPROXIMATION POTENTIAL

Csányi and coworkers[141, 16, 142] developed the Gaussian approximation potential (GAP) to generate accurate potential energy surfaces. The GAP method estimates the potential energy based on the similarity of the structure to those in a library of *ab initio* geometries, energies, and forces. The energy is inferred based on Gaussian process regression employing the known energies. The surface can be systematically improved by adding to the data in the library and the use of probabilities allows the surface to identify regions where the uncertainty is high.

The 33955 B3LYP and 36597 CCSD(T)-F12 geometries and energies were sent to the Csányi group (Cambridge) so that a GAP surface could be generated for the $NO_3^- \cdot H_2O$ complex. The dimer PES is constructed using two surfaces representing the isolated water and nitrate molecules, along with a surface representing the interaction of the two monomers. The water monomer surface was constructed as a GAP surface on top of the Partridge-Schwenke[143] potential for water. The nitrate monomer surface was created using the GAP method and additional single-point energy calculations on the nitrate ion geometries at the CCSD(T)-F12 level of theory. The monomer-monomer interactions are modeled using electrostatic interactions between the molecules with corrections from a GAP surface based on the interaction energies calculated at the CCSD(T)-F12 level of theory. The final combined GAP surface is expected to be a significant improvement over the original F12 surface.

APPENDIX B

NOTES ON THE FOLLOWING APPENDICES

The following chapters contain results from coarse-grained simulations of self-assembly. The results were obtained under the guidance of Dr. David Earl at the University of Pittsburgh between 2009 and 2010. Although the methodologies are consistent with the chapters above, the simulations are unrelated to vibrational anharmonicity and thermal transport.

APPENDIX C

SELF-ASSEMBLY OF DISCOTIC MOLECULES

C.1   INTRODUCTION

C.1.1   Self-Assembly

Many molecular systems self-assemble into more complex superstructures, and these systems are important in technological and biological fields of research. Control of self-assembly is an important goal in science and research often focuses on designing molecules to self-assemble into a particular structure. In addition it would be valuable to design molecules in which the self-assembly could be switched on and off. Both experiments and theory can be used to design new molecules that take a desired structure. Cui et al.[144] designed a system of rod-like molecules that assemble into a crystal at high concentrations, but can be assembled at lower concentrations by exposing the molecules to x-ray radiation. Yan et al.[145] used coarse-grained simulations to study a bent liquid crystal molecule that self-assembles into a chiral column of random chirality, but could be doped to produce a consistent chirality.

One class of self-assembling molecules are discotic liquid crystals, which are rigid disk-like structures. These molecules can assemble into columnar, nematic, and isotropic phases and are often made up of molecules with an aromatic core. Figure C1 shows an example of the structural order in the columnar and nematic phases. The isotopic phase is disordered in all directions, the nematic phase has order in layers, and in the columnar phase the disks grouped into stacks of molecules. Many different types of disk-like molecules are studied
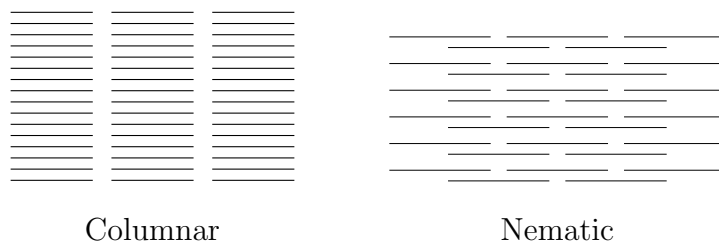
Columnar   Nematic

Figure C1: 2D representations of the columnar and nematic phases.

with experimental and theoretical investigations, and the assembled structures can be quite varied. Maeda et al.[146] studied a system of half-disk molecules which combine to form whole disks that stack into a columnar phase, and Mourad et al.[147] studied a system of metal hydroxyl ions that separates into a nematic and isotropic phase. Aida and coworkers[148,149] experimented with hexa-peri-hexabenzocoronene with a two $C_{12}H_{25}$ chains on one side and two (C_6H_4)-$(OCH_2CH_2)_3$-(OCH_3) chains on the opposite side. They found that this system self assembles into a nanotube with a 14 Å cavity in tetrahydrofuran. Andrienko et al.[150] used atomistic simulations to study hexabenzocoronene with aliphatic tails around the edges of the disks. This system forms a columnar phase with several different packing structures, however, the simulations of the disks were biased by starting with either a hexagonal or rectangular columnar arrangement. A columnar liquid crystal phase can also show chirality. One example is from the work of Barberá et al.,[151] a melamine molecule hydrogen bonds to three bent molecules made up of benzoic acid units. This hydrogen-bonded complex stacks into columns and the bent molecules can twist so the whole complex takes on a propeller-like shape.

Coarse-grained models are useful for studying systems that assemble into molecular superstructures. Modeling self-assembly dynamics can be complicated due to the large number of atoms in biological and liquid crystal forming molecules. By simplifying the models used to represent the discotic molecules, simulations can be done on larger systems and larger time scales. Cinacchi and Duijneveldt[152] studied a system of contact lens-like particles which form a isotropic phase, a nematic phase, and a cluster phase. The contact lens-like particles were modeled as infinitely thin rigid particles, and the Monte Carlo simulations produced

several phases observed in experiments. A single-bead model is the simplest method for studying disk-like molecules, however, using more beads can add detail to the molecules being studied.

C.1.2 Coarse-Grained Models

Coarse-grained models are a useful tool for studying complex systems and have several advantages over atomistic models. A coarse-grained model reduces the number of particles in the system and the number of interactions in the potential. This is usually accomplished by combining several atoms into one larger bead and representing most of the long-range interactions as a Lennard-Jones, (LJ), potential

$$E_{LJ}(r) = 4\epsilon \left(\frac{\sigma^{12}}{r^{12}} - \frac{\sigma^6}{r^6} \right) , \qquad (C.1)$$

where ϵ is the depth of the well in the potential, σ represents the radius of the particle, and E_{LJ} is the interaction energy. The LJ potential is attractive when r is greater than $\sqrt[6]{2}\sigma$, and repulsive when r is less than $\sqrt[6]{2}\sigma$. In atomistic models this potential is used to represent the van der Waals forces due to excluded volume, dipole-dipole interactions, induced dipole interactions, and dispersion interactions, however, in coarse-grained simulations it is used to represent hydrophobic, hydrophilic, and hydrogen-bonding interactions as well. Another common potential is the Weeks-Chandler-Andersen, (WCA), potential. The form of the WCA potential is almost identical to the LJ potential, except that it is shifted and truncated so that the potential is purely repulsive,

$$E_{WCA}(r) = \begin{cases} 4\epsilon \left(\frac{\sigma^{12}}{r^{12}} - \frac{\sigma^6}{r^6} \right) + \epsilon & r < \sqrt[6]{2}\sigma \\ 0 & r \geq \sqrt[6]{2}\sigma \end{cases} . \qquad (C.2)$$

The WCA potential is useful for two reasons, the first being that it is shorter range than the LJ potential, and the second being that the WCA potential can keep particles from overlapping without adding attractive forces. Representing all the possible long-range interactions of a molecule as LJ and WCA interactions allows for simpler force field interactions and the forces interact at a shorter range than force fields constructed using both the LJ and Coulomb potentials.

Coarse-grained models can be designed to represent both rigid and flexible regions of the molecules. Rigid structures are useful when modeling molecules with a specific geometry or when it is beneficial to limit the degrees of freedom in the simulation. However, there are some regions in many molecules that require flexible chains of particles, and the chemical bonds are typically modeled with a simple harmonic bond potential

$$E_{harm}(r) = \frac{k}{2}(r - r_0)^2 \ , \tag{C.3}$$

where k is the spring force constant, r_0 is the bond length, r is the distance between the beads, and E_{harm} is the bond energy. This equation can also be used to restrain angles, θ in calculations by replacing $(r - r_0)$ with $(\theta - \theta_0)$, and using the small angle approximation

$$E_{bend}(\theta) = \frac{k}{2}(\theta - \theta_0)^2 \ . \tag{C.4}$$

Other interactions can be modeled in force fields using Coulomb, dihedral angle, and hydrogen-bonding potential terms. Neglecting the electrostatic interactions tends to speed up a calculation since electrostatics are calculated using a potential proportional to $\frac{1}{r}$, which requires a large cutoff in a neighbor list. The dihedral angle potentials are generally neglected in coarse-grained models for simplicity and the fact that many of the particles in atomistic simulations are included in larger beads.

Since coarse-grained models often employ the LJ potential to represent all of the molecular interactions, the macroscopic properties are often defined in terms of σ and ϵ. The reduced temperature $(T^\star)$ and pressure $(P^\star)$ are defined as

$$T^\star = \frac{Tk_b}{\epsilon} \ , \tag{C.5}$$

and

$$P^\star = \frac{P\sigma^3}{\epsilon} \ . \tag{C.6}$$
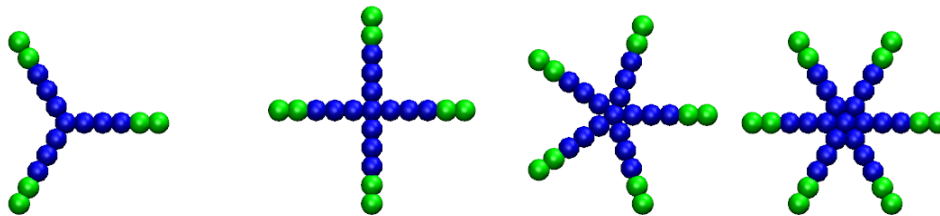
Figure C2: Structures of the four generic disks.

C.2 GENERAL DISKS

C.2.1 Description

Several general disk-like molecules were studied using molecular dynamics simulations in the NPT and NVT ensembles. The disks were represented as rigid molecules with a central bead and several branches, each branch consisted of three LJ beads (type A) followed by two WCA beads (B) on the end. The first branches were evenly spaced starting with three branches in a "Y" shape, then four branches in a "+" shape, and so forth. Figure C2 shows the shapes of the four generic disks that were used in the simulations. The beads on the outside are the solvophilic B beads, and the inner beads are the solvophobic A beads. For the general disks, all σ and ϵ values were kept at a value of 1.0, and simulations were preformed with and without solvent. When solvent was included, 20,000 beads of type B were used as the solvent. Beads of type A were LJ attractive to other A beads, and all other interactions were WCA repulsive. The various shapes are named based on the number of branches in the core of the molecules by using a prefix (e.g. tri-branched).

Most of the simulations were performed at six different reduced temperatures between $T^\star = 0.5$ and $T^\star = 3.0$ in increments of 0.5, while the reduced pressure was gradually increased. In addition to the pressure annealing simulations, the tri-branch disks were also simulated at a constant pressure while the the temperature was gradually decreased. The tri-branch simulations were performed first and since the six pressure annealing simulations seemed to produce the best results, all other simulations were performed under the same conditions

and the pressure dependence of all the systems seemed to be small. The observations and plotted data discussed below are all based on the same procedure of six simulations with the pressure increasing slowly. These pressure-annealing simulations allowed for large portions of phase-space to be sampled.

Simulations were performed using an in house code, *Pittsburgh Molecular Modeling*. Each simulation had 5,000,000-15,000,000 simulation steps and all plots were produced under the same conditions. Each unsolvated simulation contained 1000-3000 disks, each solvated simulation contained 500 disks and the number of disks included the unsolvated simulations did not seem to have a strong effect on the structures. The simulation time step was 3 fs, the temperature and pressure were controlled using the Nosé-Hoover thermostat and barostat and data was printed every 10,000 time steps to save disk space. Since the simulations were coarse-grained, the temperature, pressure, and energies were all in reduced units. The reduced units cause all physical properties to be relative to force field parameters and kT, however, the trends remain the same in real units. The temperature and pressure range used in most of the simulations kept the system as a liquid, and freezing was observed only at very high reduced pressures.

C.2.2   Tri-branch

Simulations of the tri-branch disks with no solvent formed either an isotropic phase or clustered into a micelle-like phase. No long column phase was observed, however some of the disks did stack on top of one another, and more disks appear to stack as the temperature was increased. Simulations including solvent show the tri-branch disks forming clusters at low temperatures, and an isotropic mixture at high temperatures. Two types of clusters were observed in the simulations. The first type appeared in very low temperature simulations, and consisted of an elongated cluster with little overall order to the structure. The second type appeared in slightly higher temperature simulations, and consisted of micelle-like structures where several stacks of 2-3 tri-branch disks would interlock to form a micelle-like structure.

C.2.3 Quad-branch

Simulations of the quad-branch disks showed the formation of short stacks of about 3-5 molecules in the absence of solvent. The solvated quad-branch disks showed a tendency to form elongated clusters at low temperatures, and then form short columns that grouped together. The grouped columns alternated direction and sometimes formed a structure that resembles a branched column. The stacks and columns got longer as the temperature was increased, but then started getting shorter and the higher temperature systems moved towards an isotropic mixture.

C.2.4 Penta-branch

Simulations of the unsolvated penta-branch disks showed the formation of short columns at low temperatures and the formation of long columns at higher temperatures. The columns that formed were randomly oriented, and no highly ordered columnar phase was observed. The solvated penta-branch disks formed short columns at low temperatures and the columns got longer as the temperature was increased. The columns were not ordered in any way, but rather formed in random directions.

C.2.5 Hexa-branch

Simulations of unsolvated hexa-branch disks showed the formation of columns at all temperatures. The columns were randomly oriented, and became longer at higher temperatures. The solvated hexa-branch disks form short stacks at low temperatures and then form long columns at higher temperatures. Simulations at higher temperatures formed columns that spanned almost the entire box length.

C.2.6 Results

Simulations of the tri-branch disks showed formation of only clusters and micelles, while the penta-branch and hexa-branch disks formed long columns. The quad-branch disks were in between the tri-branch and penta-branch disks and formed short stacks and long clusters. None
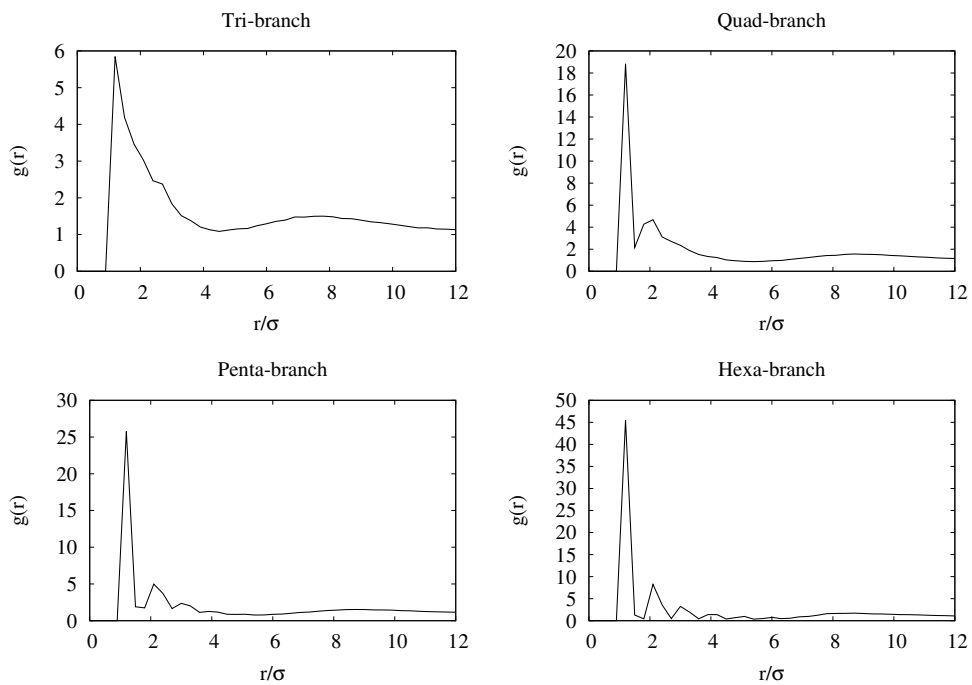
Figure C3: Radial distribution function for the four unsolvated generic disks at a reduced temperature of $T^\star = 1.5$.
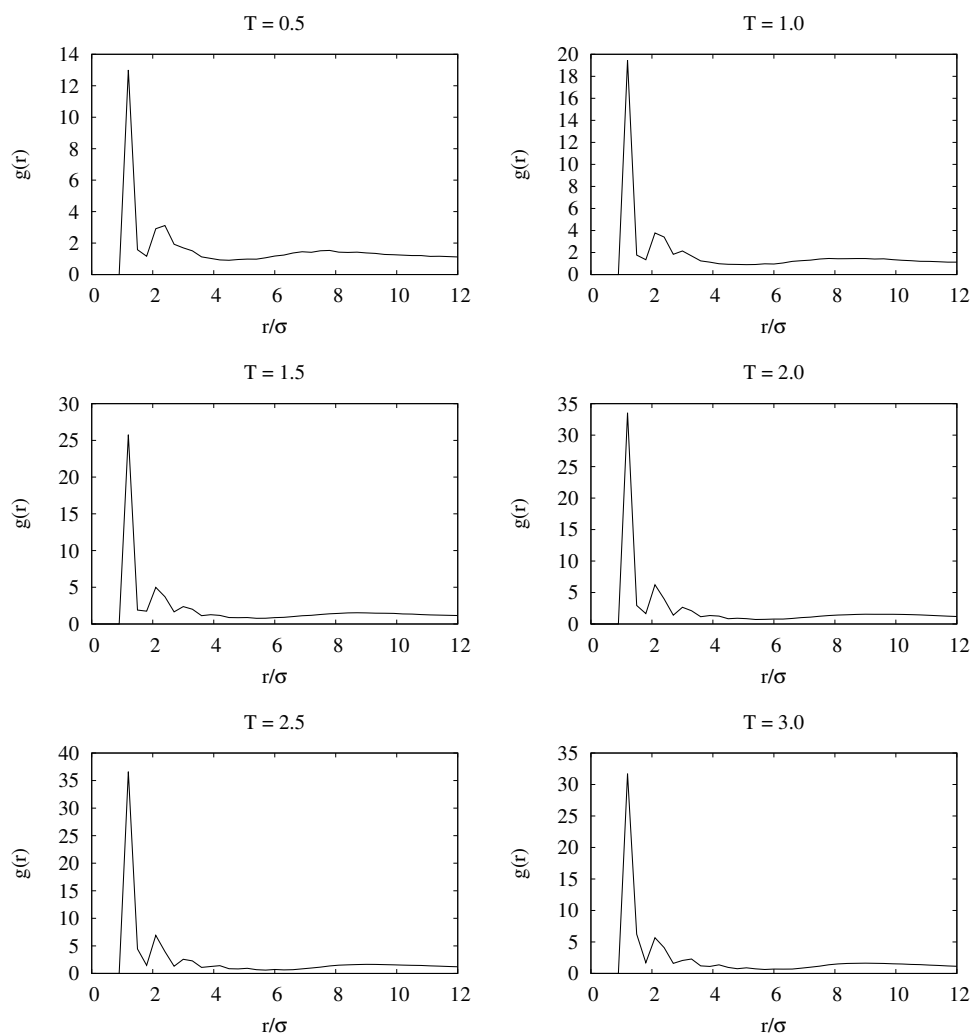
Figure C4: Radial distribution function for the six unsolvated penta-branch simulations at different reduced temperatures.

of these discotic molecules formed the highly ordered columnar phase observed in experiments and atomistic models. Experimental results for discotic molecules show the formation of a hexagonal columnar phase and a nematic phase.[153] According to Chandrasekhar et al.,[153] the nematic phase is less common than the columnar phase for discotic liquid crystals. The experimental results also show that long side chains are required for the formation of liquid crystal phases and that realistic models need to account for the flexible side chains. There are several possible explanations for the difference between the generic disks and experimental results, first, all forces in this model are spherically symmetric, while atomistic models and experiments have directional forces such as $\pi - \pi$ stacking. Second these disks have no flexible side chains, the side chains are rigid WCA repulsive particles which do not allow the columns to get close together. Third, the generic disks had very short side chains, not the long chains in the experimental systems. The generic disks studied in this work do show some general trends. As the temperature was increased, the molecules switch from forming clusters and small stacks to forming long columns. The columns appear to get longer as the simulation temperature is increased, but then the length starts to decrease again. If the temperature increase was continued the disks would be expected to return to an isotropic phase. All the geometries appeared to form columns at different temperatures, but the general trend is that the molecules with more branches form more stable columns.

The radial distribution function, $g(r)$, was calculated for the unsolvated generic disks by using the distribution of the center bead of each disk.

$$g(r) = \frac{\rho_{shell}}{\rho_{ideal}} = \frac{N_{shell}V_T}{N_T V_{shell}} \tag{C.7}$$

Here ρ_{shell} is the density of the shell between r and dr, ρ_{ideal} is the density of the whole system, N_{shell} is the number of particles in the shell, V_{shell} is the volume of the shell, V_T is the total volume, and N_T is the total number of particles. The plots in Figure C3 show an increasing number of peaks as the number of branches in the disk increases which implies that the disks with more branches form structures with longer ranged order. The $g(r)$ plots also shows an increasing peak heights as the branches are increased which is due to more of the disks being in a column-like structure. The $g(r)$ plots in Figure C4 show that as the temperature increases, columns get longer, but then start to shorten again as can be seen in

the plots of the unsolvated penta-branch disk at the six simulation temperatures. The peak height and number of peaks increases between $T = 0.5$ and $T = 2.5$, but then the plot for $T = 3.0$ has peaks that are similar to $T = 2.0$.

C.3   EXPERIMENTAL DISKS

C.3.1   Description

Two of the experimental systems listed above were also studied using coarse-grained models. The first system was the hexabenzocoronene with $C_{12}H_{25}$ chains on one side of the molecule and (C_6H_4)-$(OCH_2CH_2)_3$-(OCH_3) chains on the other side, which will be referred to as HBC. Several models were used to study the HBC molecules, most of the models represented each aromatic ring as one bead and each chain as three beads, which produces a thirteen bead hexagonal disk with solvophobic chains on one end and solvophilic chains on the other end. The experimental and coarse-grained structures are shown in Figure C5. The models that were used in the simulations can be viewed as a progression towards greater detail. The simplest model is a hexa-branch disk altered so that one half of the disk is solvophobic and the other half of the disk is solvophilic, which creates a generic disk with symmetry similar to the experimental HBC disk. The rest of the HBC models have the geometry of the experimental structure shown in Figure C5b. One model is completely rigid with all σ and ϵ values set to 1.0, another is the same except the chains attached to the disk are flexible, and the other two are parametrized with experimental thermodynamic data.

The second experimental system is based on a system that consists of a melamine core with three bent molecules hydrogen bonded to the core, and this hydrogen-bonded complex will be referred to as a propeller molecule. The propeller system was represented as a three bead triangle for the core, with the bent molecules having one bead for each benzoic acid unit, and two flexible beads for the carbon tails on the bent portion. The model was also parametrized using experimental thermodynamic data.

115
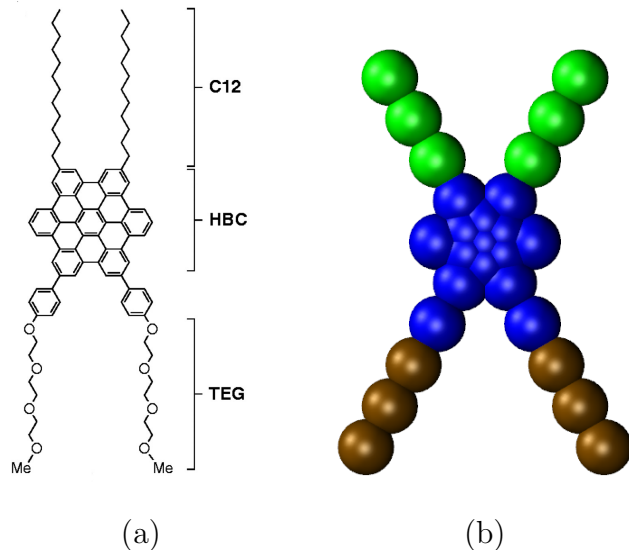
Figure C5: (a) Experimental and (b) coarse-grained HBC molecules.

Most simulations of the experimental disks were performed under the same conditions as the six pressure annealing simulations for the generic disks discussed above. Additional low density simulations were performed for the HBC molecules using the NVT ensemble with Brownian dynamics so that the solvent effects were represented as a frictional term and force with a random magnitude and direction. For the propeller molecules a wider temperature range was used since the experimenters reported the formation of the super-structures at high temperatures.

C.3.2   Generic HBC Molecules

Parameters and interactions for the first HBC model are show in Table C1. The atom types are as follows: G represents the aromatic core, I represents the solvophilic regions, B represents the solvophobic regions, and S represents the tetrahydrofuran solvent. For simplicity, all σ, ϵ, and mass values were set to 1.0.

Simulations of the rigid HBC disks with no solvent showed the formation of columns that spanned most of the box, although the orientations of the columns were distributed randomly. Simulations of the solvated rigid HBC disks resulted in the formation of clusters

Type	Mass	σ	ϵ	Type	G	I	B	S
G	1.00	1.00	1.00	G	LJ	WCA	WCA	WCA
I	1.00	1.00	1.00	I	WCA	LJ	WCA	LJ
B	1.00	1.00	1.00	B	WCA	WCA	LJ	WCA
S	1.00	1.00	1.00	S	WCA	WCA	WCA	WCA

Table C1: Parameters (right) and interaction table (left) for the basic model of HBC.

at low temperatures and long columns at mid to high temperatures. The columns would form clusters of 2-3 columns where the solvophobic tails were in the middle of the cluster of columns. The columns were mostly oriented in the same direction in the highest temperature simulation.

Simulations of solvated flexible HBC showed small layer-like structures, short columns, and clusters at low temperatures and large bilayers, monolayers, and columns formed at higher temperatures. In the mid temperature range the most stable structure was either a monolayer made from 2-3 columns or a bilayer made from two monolayers. As the temperature increased, columns with the solvophobic regions paired up started to appear, and in the highest temperature simulation only these paired columns were present.

Simulations of the hexa-branch disks with one half of the disk solvophobic and the other half solvophilic where performed in solvent. Low temperature simulations of this model produced short columns that sometimes clustered so the solvophilic parts were together. Simulations with mid to high temperatures showed the formation of long columns that grouped into clusters of 3-6 columns to shield the solvophobic beads from the solvent.

C.3.3 Parametrized HBC Molecules

The HBC disks were parametrized so that the ϵ values were not the same among different types of particles. Thermodynamic data from the literature was employed to estimate the ϵ values of each bead. The ϵ values for the interaction of two different types of beads were

117

Type	Mass	σ	ϵ	Type	G	I	B	S
G	1.00	1.00	1.44	G	LJ	WCA	WCA	WCA
I	1.00	1.00	1.06	I	WCA	LJ	WCA	LJ
B	1.00	1.00	1.00	B	WCA	WCA	LJ	WCA
S	1.00	1.00	1.55	S	WCA	WCA	WCA	WCA

Table C2: Parameters (right) and interaction table (left) for the parametrized HBC model.

generated using the combination rule $\epsilon_{ij} = \sqrt{\epsilon_{ii}\epsilon_{jj}}$. The data used to generate the values came from the standard state enthalpy of vaporization or sublimation of compounds similar to the four particle types. For instance, the core of the HBC molecule is made up of fifteen aromatic rings, so the enthalpies of aromatic compounds were divided by the number of aromatic rings and averaged to estimate the well depth of the aromatic ring LJ interaction. After the well depths for each bead were determined, all the energies were divided by the smallest value to produce relative interaction energies. The result was a series of ϵ values near 1.0, but different for each bead. Table C2 shows the parameters and interactions that resulted from this process.

Solvated simulations of HBC with this force field produced small bilayers at low temperatures, large bilayers at mid temperatures, then long unpaired columns at the highest temperature. This force field produced a wide range of structures, the smallest bilayers were about the size of a micelle, while the largest had almost every molecule in one bilayer. As the temperature increased monolayers, bilayers, and paired columns started to form, only to be replaced by long columns at the highest simulation temperature.

C.3.4   Re-parametrization

The second parametrization method divided the aromatic ring beads into three different types. Different regions of the aromatic core were given different interaction strengths, the center bead and the six surrounding beads were parametrized using coronene, the two lone

Type	Mass	σ	ϵ
G	1.32	1.00	1.31
A	1.34	1.00	1.08
C	1.40	1.00	1.16
I	1.00	1.00	1.01
B	1.04	1.00	1.00
S	1.33	1.00	1.23

Table C3: Parameters for the re-parametrized model of HBC.

aromatic rings attached to the solvophobic tails were parametrized using benzene, and to account for the hydrogens on the outside of the disk, the outer six aromatic beads were parametrized with hexane. After the new set of ϵ values were generated, the masses of each bead were changed so that each bead had a mass appropriate for its composition. Table C3 shows the parameters for the new beads. In the new model A represents the aromatic beads on the outer edge of the core, and C represents the aromatic rings attached to the solvophilic tails. Table C4 shows the interaction types for the different beads.

The solvated simulations using this force field produced mostly small bilayers. The higher temperature simulations showed some larger bilayers, columns, and monolayers, but majority of the molecules were in small bilayers.

C.3.5   Results

The simulations using the first parametrized force field appeared to capture structures closer to the experimental structures than the other models for HBC. Due to the large size of the experimental structure, none of the simulations contained enough molecules to form the whole graphitic nanotube. Since the tube is made up of a large bilayer, the formation of bilayers and paired columns is similar to the experimental structures, however, larger simulations

Type	G	A	C	I	B	S
G	LJ	LJ	LJ	WCA	WCA	WCA
A	LJ	LJ	LJ	WCA	WCA	WCA
C	LJ	LJ	LJ	WCA	WCA	WCA
I	WCA	WCA	WCA	LJ	WCA	LJ
B	WCA	WCA	WCA	WCA	LJ	WCA
S	WCA	WCA	WCA	WCA	WCA	WCA

Table C4: Interaction table for the re-parametrized model of HBC.

would be required to see the layers or columns twisting into a tube or forming a bilayer which exhibits curvature.

C.3.6   Propeller

The coarse-grained model for the propeller molecule was parametrized by using benzoic acid for the beads on the bent molecule and using melamine for the core. The core had three beads to represent the ring and one bent molecule was bonded to each ring bead. The bent molecules were made up of five benzoic acid beads in a "V" shape, and two carbon chain beads at the end of each side of the V. The bent molecules were held in place via a harmonic bond to the ring and two harmonic angle terms between the ring, bent molecule, and a dummy atom. The model was designed to approximately hold the whole molecule planar, but allow the V shaped parts to rotate.

C.3.7   Results

In the lowest temperature simulation, the propeller molecules separated from the solvent and as the temperature increased the molecules formed clusters, pairs, and long column-like structures. The column-like structures that formed were not columns of the disk-like core, but

rather elongated structures with no overall order to the disk-like cores. No chiral structures were observed, even when just two molecules were stacked into a pair.

APPENDIX D

SELF-ASSEMBLY OF PEPTIDE AMPHIPHILES

D.1   INTRODUCTION

D.1.1   Description

Peptide amphiphiles are an important class of molecules for self-assembly research. Experiments have shown peptide amphiphiles can assemble into layers, fibers, micelles, and helical structures. Chen et al.[154] designed peptide amphiphiles that self-assemble with gold nanoparticles to form double helices. The nanoparticle-amphiphiles building blocks consist of $C_{11}H_{23}CO$-AYSSGAPPMPPF chains attached to gold nanoparticles. The double helix consists of two ribbons of the amphiphile with the the hydrophobic tails of the ribbons paired up. The double ribbon then twists into a helix, with the nanoparticles on the outside.

Research by Meister et al.[155] also showed the formation of a helical structure using amphiphiles and gold nanoparticles. The amphiphile used in their work was a bipolar phospholipid, resembling a bola, which form a fiber structure containing a helical arrangement of molecules. The achiral molecules were shown to form this chiral structure in both the experiments and Monte Carlo simulations containing only two atom types. The atom types included in the simulations were large hydrophilic head beads and smaller hydrophobic spacer beads.

Purely theoretical models have been developed based on physical properties, coarse-grained simulations, and atomistic simulations.[156,157] The complexity of the model used

has a direct impact on the information that can be extracted from the research. Simple models can be created by writing Hamiltonians or free energies in terms of system properties, environmental conditions, and concentrations of molecules. Designing equations to model the system is efficient, however, the approach focuses on bulk properties instead of giving detailed chemical insight. More complex models have been developed that focus on entropic and geometric effects, these models can show which structures are likely to form, even in the absence of chemical detail. Snir and Kamien[158] showed that a column could adopt a helical structure with just a hard sphere model to represent the interactions of particles, and Tsonchev et al.[159] showed that micelles have a higher factional density than other possible structures which makes that structure very stable.

Simple coarse-grained models of amphiphiles can also be developed based lattice Monte Carlo simulations. Panagiotopoulos and coworkers[160,161] used grand canonical Monte Carlo simulations to study the structure formation of rigid nanoparticles with flexible tails. These simulations were used to produce phase diagrams, calculate free energies, and calculate osmotic pressures of the various shapes and sizes of nanoparticles. Lattice models have an advantage over atomistic and other coarse-grained models due to the lower computational cost of Monte Carlo simulations on a lattice. Since the distance between lattice points is already known, costly distance calculations are unnecessary, and larger systems or longer simulation times can be achieved. However, since lattice models restrict where a particle can be located, structural details such as chirality may be lost.

Ratner and coworkers[159,162,163,164] used atomistic molecular dynamics simulations to study the structure formation of Zwitterionic peptide amphiphiles. Their work showed that the structure formation was due to a combination of the hydrogen bonding of the region near the carbon tail, the dipole of the head group, and the hydrophobic and hydrophilic effects. Their work produced phase diagrams for the amphiphiles based on the pH and composition of the mixture, as well as showing that a curved structure is more stable than an uncurved structure.

D.1.2   MARTINI Force field

Marrink and coworkers[165, 166, 167] have developed the coarse-grained MARTINI force field which attempts to capture atomistic detail while still being efficient enough to be useful for studying large systems and biologically important molecules. The model was originally designed to study the self-assembly of lipids and surfactants, however, it was later extended to amino acids and proteins. The model uses approximately four heavy atoms per bead, and represents most interactions with the Lennard-Jones and harmonic bond potentials. Charges can be added to some of the beads to represent the effects of pH on structure formation, and dihedral angle potentials can be used to include geometric details such as a ring being planar and an amino acid sequence having a helical conformation. This model is simple, 5-10 times faster than atomistic simulations, has faster diffusion and kinetics, and reproduces structures and phases consistent with experimental observations.

D.2   MARTINI PEPTIDES

D.2.1   Methods

Molecular dynamics simulations of $C_{11}H_{23}CO$-AYSSGAPPMPPF were preformed using the MARTINI force field and the GROMACS software package while varying the concentration of amphiphiles, system size, and pH. The pH was varied by simulating both the protonated and deprotonated forms of the amphiphile, and the deprotonation was assumed to occur at the last amino acid in the chain. Both NVT and NPT simulations were used for comparison and the simulation size was changed to test for size effects on the structure formation. Three different mole fractions (0.005, 0.010, and 0.030) of amphiphiles were used in the simulations.

In addition to the simulations of $C_{11}H_{23}CO$-AYSSGAPPMPPF, calculations were performed with variations of the peptide amphiphile structure. Extra alanines were added to the start of the peptide near the carbonyl, the AYSS sequence was repeated, and the carbon tail was lengthened. These changes were made so the effects of the hydrophobic interaction

and the formation of beta sheets could be assessed (the AYSS sequence was thought to form a beta sheet in the double helix structure).

D.2.2 Results

The structures of the MARTINI peptide amphiphile is shown in Figure D1a, the four beads on the left represent the hydrophobic tails, the eight beads arranged with triangular arrangement represent the ring structures, and the remaining beads represent the amino acids and their side chains.

Several different phases and structures were found in an analysis of the simulations, including an isotropic phase, columns, layers, micelles, and a network structure. Both the column and layer structures had two variations, the protonated molecules formed flat layers and straight columns, while the deprotonated molecules formed a wavy layer and a column that appeared to have either a wave or a twist. With the exception of the network structure, all of the simulation structures corresponded to a structure seen experimentally, however, the structures found in the simulations displayed some unusual properties. For instance, both layers and wavy layers are seen experimentally, however, the layers from the MARTINI peptides had some of the hydrophobic beads exposed to the solvent. The layer seemed to be made up of peptide regions with hydrophobic pockets distributed across the surface. Additionally, the other structures had the hydrophobic regions exposed to the solvent instead of being shielded by the hydrophilic regions. The network structure seemed to form in the higher concentration and larger simulation boxes, and was characterized as having all the amphiphiles along the edges of the simulation box.

The amphiphiles constructed with the MARTINI force field systems did model self-assembly and produced structures with superficial similarities to experimental work, however, the results were not accurate enough to give insight or predict properties. Since the MARTINI model does produce accurate simulations of lipid bilayer formation, it can be concluded that peptide amphiphiles are too far removed from the molecules used to parametrize the MARTINI model.
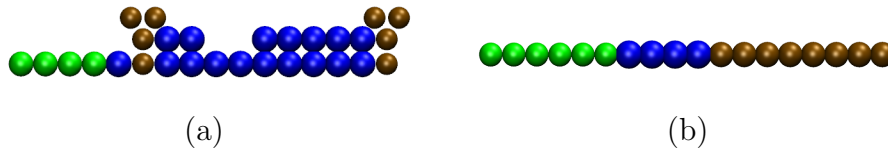
Figure D1: (a) MARTINI and (b) Monte Carlo versions of $C_{11}H_{23}$CO-AYSSGAPPMPPF.

D.3   OTHER MODELS

Two models that are more coarse-grained than the MARTINI force field, but tailored towards $C_{11}H_{23}$CO-AYSSGAPPMPPF were designed using just four atom types. The first type was hydrophobic beads for the tail that interacted with themselves via the LJ potential, and the WCA potential for all other beads. The second type was a protein bead that was LJ attractive to the solvent and other protein beads, but WCA repulsive to the hydrophobic beads. The third type was a solvent bead, and the last bead was a beta sheet forming bead. The beta sheet forming bead was constructed so that it was LJ attractive to itself in one direction and WCA repulsive to itself in the perpendicular direction. The model also had the option of turning on dipole forces on the protein beads. The $C_{11}H_{23}$CO-AYSSGAPPMPPF structure under this model would become CCCCC-BBBBPPPPPPPP, and could capture the hydrophobic, hydrophilic, hydrogen bonding, and dipoles deemed important in the literature. This model is shown in Figure D1b, the six beads on the left represent the hydrophobic tails, the four beads in the middle represent the peptides that want to form beta sheets, and the eight beads on the right represent the hydrophilic peptides.

The difference in the two models was the choice of simulation methods. The first model used molecular dynamics simulations to study the self-assembly while the second model used a lattice Monte Carlo method. The purpose of these models was to test if the four interactions mentioned above were enough to form either the ribbon or double helix structures reported by Chen et al., however, the parameterization was never completed during the course of this research.

126

BIBLIOGRAPHY

[1] C. Vega, J. L. F. Abascal, M. M. Conde, and J. L. Aragones. What ice can teach us about water interactions: A critical comparison of the performance of different water models. Faraday Discuss., 141(0):251–276, 2009.

[2] J. D. Bernal and R. H. Fowler. A theory of water and ionic solution, with particular reference to hydrogen and hydroxyl ions. J. Chem. Phys., 1(8):515–548, August 1933.

[3] V. Buch, P. Sandler, and J. Sadlej. Simulations of h$_2$o solid, liquid, and clusters, with an emphasis on ferroelectric ordering transition in hexagonal ice. J. Phys. Chem. B, 102(44):8641–8653, October 1998.

[4] Swaroop Chatterjee, Pablo G. Debenedetti, Frank H. Stillinger, and Ruth M. Lynden-Bell. A computational investigation of thermodynamics, structure, dynamics and solvation behavior in modified water models. J. Chem. Phys., 128(12):124511–9, March 2008.

[5] Phillip L. Geissler, Christoph Dellago, David Chandler, Jurg Hutter, and Michele Parrinello. Autoionization in liquid water. Science, 291(5511):2121–2124, 2001.

[6] Valeria Molinero and Emily B. Moore. Water modeled as an intermediate element between carbon and silicon. J. Phys. Chem. B, 113(13):4008–4016, April 2009.

[7] Daniel J. Price and Charles L. Brooks III. A modified tip3p water potential for simulation with ewald summation. J. Chem. Phys., 121(20):10096–10103, November 2004.

[8] Kahled Toukan and Aneesur Rahman. Molecular-dynamics study of atomic motions in water. Phys. Rev. B, 31(5):2643, March 1985.

[9] Yujie Wu, Harald L. Tepper, and Gregory A. Voth. Flexible simple point-charge water model with improved liquid-state properties. J. Chem. Phys., 124(2):024503, January 2006.

[10] Linus Pauling. The structure and entropy of ice and of other crystals with some randomness of atomic arrangement. J. Am. Chem. Soc., 57(12):2680–2684, December 1935.

[11] B. Pamuk, J. M. Soler, R. Ramirez, C. P. Herrero, P. W. Stephens, P. B. Allen, and M.-V. Fernandez-Serra. Anomalous nuclear quantum effects in ice. Phys. Rev. Lett., 108(19):193003, May 2012.

[12] Francesco Paesani, Wei Zhang, David A. Case, Thomas E. Cheatham, and Gregory A. Voth. An accurate and simple quantum model for liquid water. J. Chem. Phys., 125(18):184507, November 2006.

[13] Scott Habershon, Thomas E. Markland, and David E. Manolopoulos. Competing quantum effects in the dynamics of a flexible water model. J. Chem. Phys., 131(2):–, 2009.

[14] Francesco Paesani and Gregory A. Voth. Quantum effects strongly influence the surface premelting of ice. J. Phys. Chem. C, 112(2):324–327, December 2007.

[15] Tomas K. Hirsch and Lars Ojamae. Quantum-chemical and force-field investigations of ice ih: Computation of proton-ordered structures and prediction of their lattice energies. J. Phys. Chem. B, 108(40):15856–15864, September 2004.

[16] Albert P. Bartók, Michael J. Gillan, Frederick R. Manby, and Gábor Csányi. Machine-learning approach for one- and two-body corrections to density functional theory: Applications to molecular and condensed water. Phys. Rev. B, 88(5):054104, August 2013.

[17] Revati Kumar, Fang-Fang Wang, Glen R. Jenness, and Kenneth D. Jordan. A second generation distributed point polarizable water model. J. Chem. Phys., 132(1), 2010.

[18] Ling Jiang, Torsten Wende, Risshu Bergmann, Gerard Meijer, and Knut R. Asmis. Gas-phase vibrational spectroscopy of microhydrated magnesium nitrate ions $[MgNO_3(H_2O)_{1-4}]^+$. J. Am. Chem. Soc., 132(21):7398–7404, 2010. PMID: 20459103.

[19] Sai G. Ramesh, Suyong Re, and James T. Hynes. Charge transfer and oh vibrational frequency red shifts in nitrate-water clusters. J. Phys. Chem. A, 112(15):3391–3398, March 2008.

[20] Eloy Ramos-Cordoba, Daniel S. Lambrecht, and Martin Head-Gordon. Charge-transfer and the hydrogen bond: Spectroscopic and structural implications from electronic structure calculations. Faraday Discuss., 150(0):345–362, 2011.

[21] Mingzuo Shen, Yaoming Xie, Henry F. Schaefer, and Carol A. Deakyne. Hydrogen bonding between the nitrate anion (conventional and peroxy forms) and the water molecule. J. Chem. Phys., 93(5):3379–3388, 1990.

[22] O. Vendrell, F. Gatti, and H.-D. Meyer. Dynamics and infrared spectroscopy of the protonated water dimer. Ange. Chem.Int. Ed., 46(36):6918–6921, 2007.

[23] Xue-Bin Wang, Xin Yang, Lai-Sheng Wang, and John B. Nicholas. Photodetachment and theoretical study of free and water-solvated nitrate anions, $no_3^- \cdot (h_2o)_n$ (n=0-6). J. Chem. Phys., 116(2):561–570, 2002.

[24] Mark R. Waterland, David Stockwell, and Anne Myers Kelley. Symmetry breaking effects in no_3^-: Raman spectra of nitrate salts and ab initio resonance raman spectra of nitrate-water complexes. J. Chem. Phys., 114(14):6249–6258, 2001.

[25] D. Blume and K. B. Whaley. Tunneling splittings in water trimer by projector monte carlo. J. Chem. Phys., 112(5):2218–2226, February 2000.

[26] Christoph Ebner, Roland Sansone, and Michael Probst. Quantum chemical study of the interaction of nitrate anion with water. Int. J. Quantum Chem., 70(4-5):877–886, 1998.

[27] Daniel J. Goebbert, Etienne Garand, Torsten Wende, Risshu Bergmann, Gerard Meijer, Knut R. Asmis, and Daniel M. Neumark. Infrared spectroscopy of the microhydrated nitrate ions $NO_3^-(H_2O)_{1-6}$. J. Phys. Chem. A, 113(26):7584–7592, July 2009.

[28] Jan Thogersen, Julien Rehault, Michael Odelius, Tom Ogden, Naresh K. Jena, Svend J. Knak Jensen, Søren R. Keiding, and Jan Helbing. Hydration dynamics of aqueous nitrate. J. Phys. Chem. B, 117(12):3376–3388, March 2013.

[29] Evgeniy M. Myshakin, Kenneth D. Jordan, Edwin L. Sibert III, and Mark A. Johnson. Large anharmonic effects in the infrared spectra of the symmetrical $CH_3NO_2^- \cdot H_2O$ and $CH_3CO_2^- \cdot H_2O$ complexes. J. Chem. Phys., 119(19):10138–10145, 2003.

[30] O. Andersson and H. Suga. Thermal conductivity of the ih and xi phases of ice. Phys. Rev. B, 50(10):6583–6588, September 1994.

[31] Niall J. English and John S. Tse. Thermal conduction and phonon propagation in pressure-amorphized ices. Phys. Rev. B, 83(18):184114–, May 2011.

[32] Steven W. Rick. Simulations of proton order and disorder in ice ih. J. Chem. Phys., 122(9):094504, 2005.

[33] R. Ramírez, N. Neuerburg, and C. P. Herrero. The phase diagram of ice: A quasi-harmonic study based on a flexible water model. J. Chem. Phys., 139(8), 2013.

[34] R. Ramírez, N. Neuerburg, and C. P. Herrero. The phase diagram of ice ih, ii, and iii: A quasi-harmonic study. J. Chem. Phys., 137(13), 2012.

[35] M. B. Helgerud, W. F. Waite, S. H. Kirby, and A. Nur. Elastic wave speeds and moduli in polycrystalline ice ih, si methane hydrate, and sii methane-ethane hydrate. J. Geophys. Res., 114(B2):B02212, 2009.

[36] E. Dendy Sloan. Gas hydrates: Review of physical/chemical properties. Energy Fuels, 12(2):191–196, February 1998.

[37] M. B. Helgerud, J. Dvorkin, A. Nur, A. Sakai, and T. Collett. Elastic wave velocity in marine sediments with gas hydrates: Effective medium modeling. Geophys. Res. Lett., 26(13):2021–2024, 1999.

[38] Keith A. Kvenvolden. Methane hydrate - a major reservoir of carbon in the shallow geosphere? Chem. Geo., 71(1–3):41–51, December 1988.

[39] Bruce Buffett and David Archer. Global inventory of methane clathrate: Sensitivity to changes in the deep ocean. Earth Plan. Sci. Lett., 227(3):185–199, November 2004.

[40] E. G. Hammerschmidt. Formation of gas hydrates in natural gas transmission lines. Ind. Eng. Chem., 26(8):851–855, August 1934.

[41] Daniel A. Lashof and Dilip R. Ahuja. Relative contributions of greenhouse gas emissions to global warming. Nature, 344(6266):529–531, April 1990.

[42] J. E. Turney, A. J. H. McGaughey, and C. H. Amon. Assessing the applicability of quantum corrections to classical thermal conductivity predictions. Phys. Rev. B, 79(22):224305, June 2009.

[43] V.P. Shpakov, J.S. Tse, C.A. Tulk, B. Kvamme, and V.R. Belosludov. Elastic moduli calculation and instability in structure i methane clathrate hydrate. Chem. Phys. Lett., 282(2):107–114, January 1998.

[44] R. Ramírez, N. Neuerburg, M.-V. Fernández-Serra, and C. P. Herrero. Quasi-harmonic approximation of thermodynamic properties of ice ih, ii, and iii. J.Chem. Phys., 137(4), 2012.

[45] Karl K. Irikura, Russell D. Johnson, and Raghu N. Kacker. Uncertainties in scaling factors for ab initio vibrational frequencies. J. Phys. Chem. A, 109(37):8430–8437, August 2005.

[46] Joel M. Bowman, Stuart Carter, and Xinchuan Huang. Multimode: a code to calculate rovibrational energies of polyatomic molecules. Int. Rev. Phys. Chem., 22(3):533–549, 2003.

[47] R. D. Amos, N. C. Handy, W. H. Green, D. Jayatilaka, A. Willetts, and P. Palmieri. Anharmonic vibrational properties of CH_2F_2: A comparison of theory and experiment. J. Chem. Phys., 95(11):8323–8336, 1991.

[48] Yimin Wang, Stuart Carter, Bastiaan J. Braams, and Joel M. Bowman. Multimode quantum calculations of intramolecular vibrational energies of the water dimer and trimer using ab initio-based potential energy surfaces. J. Chem. Phys., 128(7):071101–5, February 2008.

[49] Mauricio D. Coutinho-Neto, Alexandra Viel, and Uwe Manthe. The ground state tunneling splitting of malonaldehyde: Accurate full dimensional quantum dynamics calculations. J. Chem. Phys., 121(19):9207–9210, November 2004.

[50] Anne B. McCoy. Diffusion monte carlo approaches for investigating the structure and vibrational spectra of fluxional systems. Int. Rev. in Phys. Chem., 25(1-2):77–107, January 2006.

[51] J. E. Turney, A. J. H. McGaughey, and C. H. Amon. In-plane phonon transport in thin films. J. Appl. Phys., 107(2):024317–8, January 2010.

[52] D. A. Broido, A. Ward, and N. Mingo. Lattice thermal conductivity of silicon from empirical interatomic potentials. Phys. Rev. B, 72(1):014308, July 2005.

[53] J. E. Turney, E. S. Landry, A. J. H. McGaughey, and C. H. Amon. Predicting phonon properties and thermal conductivity from anharmonic lattice dynamics calculations and molecular dynamics simulations. Phys. Rev. B, 79(6):064301, February 2009.

[54] Charles Kittel. Introduction to Solid State Physics. John Wiley and Sons, Inc., eighth edition, 2005.

[55] Loup Verlet. Computer "experiments" on classical fluids. i. thermodynamical properties of lennard-jones molecules. Phys. Rev., 159(1):98–103, July 1967.

[56] H. J. C. Berendsen, J. P. M. Postma, W. F. van Gunsteren, A. DiNola, and J. R. Haak. Molecular dynamics with coupling to an external bath. J. Chem. Phys., 81(8):3684–3690, October 1984.

[57] Glenn J. Martyna, Douglas J. Tobias, and Michael L. Klein. Constant pressure molecular dynamics algorithms. J. Chem. Phys., 101(5):4177–4189, September 1994.

[58] T. Schneider and E. Stoll. Molecular-dynamics study of a three-dimensional one-component model for distortive phase transitions. Phys. Rev. B, 17(3):1302–1322, February 1978.

[59] Tamio Ikeshoji and Bjorn Hafskjold. Non-equilibrium molecular dynamics calculation of heat conduction in liquid and through liquid-gas interface. Mol. Phys., 81(2):251–261, February 1994.

[60] Florian Muller-Plathe. A simple nonequilibrium molecular dynamics method for calculating the thermal conductivity. J. Chem. Phys., 106(14):6082–6085, April 1997.

[61] P. C. Howell. Thermal conductivity calculation with the molecular dynamics direct method i: More robust simulations of solid materials. J. Comp. Theor. Nanosci., 8(10):2129–2143, 2011.

[62] P. C. Howell. Thermal conductivity calculation with the molecular dynamics direct method ii: Improving the computational efficiency. J. Comp. Theor. Nanosci., 8(10):2144–2154, 2011.

[63] P. C. Howell. Comparison of molecular dynamics methods and interatomic potentials for calculating the thermal conductivity of silicon. J. Chem. Phys., 137(22), 2012.

[64] Florent Domine and Paul B. Shepson. Air-snow interactions and atmospheric chemistry. Science, 297(5586):1506–1510, 2002.

[65] H. Heitmann and F. Arnold. Composition measurements of tropospheric ions. Nature, 306(5945):747–751, December 1983.

[66] Kimberly A. Prather, Courtney D. Hatch, and Vicki H. Grassian. Analysis of atmospheric aerosols. Annu. Rev. Anal. Chem., 1(1):485–514, June 2008.

[67] Man Xu, Cheng Y. Tang, Aaron M. Jubb, Xiangke Chen, and Heather C. Allen. Nitrate anions and ion pairing at the air-aqueous interface. J. Phys. Chem. C, 113(6):2082–2087, December 2008.

[68] Gil Markovich, Stuart Pollack, Rina Giniger, and Ori Cheshnovsky. Photoelectron spectroscopy of cl$^-$, br$^-$, and i$^-$ solvated in water clusters. J. Chem. Phys., 101(11):9344–9353, 1994.

[69] Orlando M. Cabarcos, Corey J. Weinheimer, James M. Lisy, and Sotiris S. Xantheas. Microscopic hydration of the fluoride anion. J. Chem. Phys., 110(1):5–8, 1999.

[70] William H. Robertson and Mark A. Johnson. Molecular aspects of halide ion hydration: The cluster approach. Annu. Rev. Phys. Chem., 54(1):173–213, October 2003.

[71] Xue-Bin Wang, Xin Yang, and Lai-Sheng Wang. Probing solution-phase species and chemistry in the gas phase. Int. Rev. Phys. Chem., 21(3):473–498, July 2002.

[72] Knut R. Asmis and Daniel M. Neumark. Vibrational spectroscopy of microhydrated conjugate base anions. Acc. Chem. Res., 45(1):43–52, June 2011.

[73] Helen K. Gerardi, Andrew F. DeBlase, Xiaoge Su, Kenneth D. Jordan, Anne B. McCoy, and Mark A. Johnson. Unraveling the anomalous solvatochromic response of the formate ion vibrational spectrum: An infrared, ar-tagging study of the HCO_2^-, DCO_2^-, and $HCO_2^- \cdot H_2O$ ions. J. Phys. Chem. Lett., 2(19):2437–2441, August 2011.

[74] William H. Robertson, Erica A. Price, J. Mathias Weber, Joong-Won Shin, Gary H. Weddle, and Mark A. Johnson. Infrared signatures of a water molecule attached to triatomic domains of molecular anions: Evolution of the H-bonding configuration with domain length. J. Phys. Chem. A, 107(34):6527–6532, August 2003.

[75] Holger Schneider, A. Daniel Boese, and J. Mathias Weber. Unusual hydrogen bonding behavior in binary complexes of coinage metal anions with water. J. Chem. Phys., 123(8), 2005.

[76] A. K. Pathak, T. Mukherjee, and D. K. Maity. Microhydration of no3-: A theoretical study on structure, stability and ir spectra. J. Phys. Chem. A, 112(15):3399–3408, March 2008.

132

[77] J. M. Howell, A. M. Sapse, E. Singman, and G. Snyder. Ab initio scf calculations of $no_2^-(h_2o)_n$ and $no_3^-(h_2o)_n$ clusters. J. Phys. Chem., 86(13):2345–2349, June 1982.

[78] Daniel J. Goebbert, Gerard Meijer, and Knut R. Asmis. 10 k ring electrode trap-tandem mass spectrometer for infrared spectroscopy of mass selected ions. AIP Conf. Proc., 1104(1):22–29, March 2009.

[79] W. R. Bosenberg and Dean R. Guyer. Broadly tunable, single-frequency optical parametric frequency-conversion system. J. Opt. Soc. Am. B, 10(9):1716–1722, September 1993.

[80] T. Wende. Gas Phase Infrared Photodissociation Spectroscopy of Mass-Selected Ionic Clusters: Metal Oxides and Microhydrated Anions. PhD thesis, Freie Universitat Berlin, 2012.

[81] G. Herzberg. Molecular Spectra and Molecular Structure, volume 2. Van Nostrand, 1966.

[82] Patrick Ayotte, Jude A. Kelley, Steen B. Nielsen, and Mark A. Johnson. Vibrational spectroscopy of the $f^-\cdot h_2o$ complex via argon predissociation: Photoinduced, intracluster proton transfer? Chem. Phys. Lett., 316(5-6):455–459, January 2000.

[83] Rodney J. Bartlett, J.D. Watts, S.A. Kucharski, and J. Noga. Non-iterative fifth-order triple and quadruple excitation energy corrections in correlated methods. Chem. Phys. Lett., 165(6):513–522, February 1990.

[84] Krishnan Raghavachari, Gary W. Trucks, John A. Pople, and Martin Head-Gordon. A fifth-order perturbation comparison of electron correlation theories. Chem. Phys. Lett., 157(6):479–483, May 1989.

[85] Rick A. Kendall, Thom H. Dunning, Jr., and Robert J. Harrison. Electron affinities of the first-row atoms revisited. systematic basis sets and wave functions. J. Chem. Phys., 96(9):6796–6806, May 1992.

[86] Thom H. Dunning, Jr. Gaussian basis sets for use in correlated molecular calculations. i. the atoms boron through neon and hydrogen. J. Chem. Phys., 90(2):1007–1023, January 1989.

[87] Michael E. Harding, Thorsten Metzroth, Jurgen Gauss, and Alexander A. Auer. Parallel calculation of CCSD and CCSD(T) analytic first and second derivatives. J. Chem. Theor. Comp., 4(1):64–74, January 2008.

[88] Thomas B. Adler, Gerald Knizia, and Hans-Joachim Werner. A simple and efficient ccsd(t)-f12 approximation. J. Chem. Phys., 127(22):221106, December 2007.

[89] Kirk A. Peterson, Thomas B. Adler, and Hans-Joachim Werner. Systematically convergent basis sets for explicitly correlated wavefunctions: The atoms h, he, b-ne, and al-ar. J. Chem. Phys., 128(8):084102, February 2008.

[90] H.-J. Werner, P. J. Knowles, G. Knizia, F. R. Manby, M. Schütz, and Others. Molpro, version 2009.1, a package of ab initio programs, 2009. see http://www.molpro.net.

[91] Bogumil Jeziorski, Robert Moszynski, and Krzysztof Szalewicz. Perturbation theory approach to intermolecular potential energy surfaces of van der waals complexes. Chem. Rev., 94(7):1887–1930, November 1994.

[92] Justin M. Turney, Andrew C. Simmonett, Robert M. Parrish, Edward G. Hohenstein, Francesco A. Evangelista, Justin T. Fermann, Benjamin J. Mintz, Lori A. Burns, Jeremiah J. Wilke, Micah L. Abrams, Nicholas J. Russ, Matthew L. Leininger, Curtis L. Janssen, Edward T. Seidl, Wesley D. Allen, Henry F. Schaefer, Rollin A. King, Edward F. Valeev, C. David Sherrill, and T. Daniel Crawford. Psi4: An open-source ab initio electronic structure program. WIREs Comput. Mol. Sci., 2(4):556–565, 2012.

[93] Anthony J. Stone and Alston J. Misquitta. Charge-transfer in symmetry-adapted perturbation theory. Chem. Phys. Lett., 473(1–3):201–205, April 2009.

[94] Reinhart Ahlrichs, Michael Bar, Marco Haser, Hans Horn, and Christoph Kolmel. Electronic structure calculations on workstation computers: The program system turbomole. Chem. Phys. Lett., 162(3):165–169, October 1989.

[95] Bastiaan J. Braams and Joel M. Bowman. Permutationally invariant potential energy surfaces in high dimensionality. Int. Rev. Phys. Chem., 28(4):577–606, 2009.

[96] James B. Anderson. A random walk simulation of the schrödinger equation: H_3^+. J. Chem. Phys., 63(4):1499–1503, 1975.

[97] James B. Anderson. Quantum chemistry by random walk. H ^{2}P, H_3^+ D_{3h} ^{1}A'$_1$, H_2 $^3\Sigma_u^+$, H_4 $^1\Sigma_g^+$, Be ^{1}S. J. Chem. Phys., 65(10):4121–4127, 1976.

[98] Martin A. Suhm and Robert O. Watts. Quantum monte carlo studies of vibrational states in molecules and clusters. Phys. Rep., 204(4):293–329, June 1991.

[99] Niall J. English and J. M. D. Macelroy. Structural and dynamical properties of methane clathrate hydrates. J. Comp. Chem., 24(13):1569–1581, 2003.

[100] Liam C. Jacobson and Valeria Molinero. A methane-water model for coarse-grained simulations of solutions and clathrate hydrates. J. Phys. Chem. B, 114(21):7302–7311, May 2010.

[101] H. Jiang and K. D. Jordan. Comparison of the properties of xenon, methane, and carbon dioxide hydrates from equilibrium and nonequilibrium molecular dynamics simulations. J. Phys. Chem. C, 114(12):5555–5564, April 2010.

[102] Hao Jiang, Evgeniy M. Myshakin, Kenneth D. Jordan, and Robert P. Warzinski. Molecular dynamics simulations of the thermal conductivity of methane hydrate. J. Phys. Chem. B, 112(33):10207–10216, July 2008.

[103] Michael T. Kirchner, Roland Boese, W. Edward Billups, and Lewis R. Norman. Gas hydrate single-crystal structure analyses. J. Am. Chem. Soc., 126(30):9407–9412, July 2004.

[104] Sapna Sarupria and Pablo G. Debenedetti. Homogeneous nucleation of methane hydrate in microsecond molecular dynamics simulations. J. Phys. Chem. Lett., 3(20):2942–2947, September 2012.

[105] C. Gutt, B. Asmussen, W. Press, M. R. Johnson, Y. P. Handa, and J. S. Tse. The structure of deuterated methane-hydrate. J. Chem. Phys., 113(11):4713–4721, September 2000.

[106] A. I. Krivchikov, B. Ya. Gorodilov, O. A. Korolyuk, V. G. Manzhelii, H. Conrad, and W. Press. Thermal conductivity of methane-hydrate. J. Low Temp. Phys., 139(5-6):693–702, 2005.

[107] Eilis J. Rosenbaum, Niall J. English, J. Karl Johnson, David W. Shaw, and Robert P. Warzinski. Thermal conductivity of methane hydrate from experiment and molecular simulation. J. Phys. Chem. B, 111(46):13194–13205, October 2007.

[108] Niall J. English and John S. Tse. Mechanisms for thermal conduction in methane hydrate. Phys. Rev. Lett., 103(1):015901, June 2009.

[109] Niall J. English, John S. Tse, and Declan J. Carey. Mechanisms for thermal conduction in various polymorphs of methane hydrate. Phys. Rev. B, 80(13):134306, October 2009.

[110] Niall J. English and John S. Tse. Perspectives on hydrate thermal conductivity. Energies, 3(12):1934–1942, 2010.

[111] Jer-Lai Kuo, Michael L. Klein, and Werner F. Kuhs. The effect of proton disorder on the structure of ice-ih: A theoretical study. J. Chem. Phys., 123(13):134505, 2005.

[112] S. M. Jackson, V. M. Nield, R. W. Whitworth, M. Oguro, and C. C. Wilson. Single-crystal neutron diffraction studies of the structure of ice xi. J. Phys. Chem. B, 101(32):6142–6145, August 1997.

[113] Yamato Okano and Kenji Yasuoka. Free-energy calculation of structure-h hydrates. J. Chem. Phys., 124(2):024510, 2006.

[114] William L. Jorgensen, Jeffry D. Madura, and Carol J. Swenson. Optimized intermolecular potential functions for liquid hydrocarbons. J. Am. Chem. Soc., 106(22):6638–6646, October 1984.

[115] Steve Plimpton. Fast parallel algorithms for short-range molecular dynamics. J. Comp. Phys., 117(1):1–19, March 1995.

[116] Fernando Bresme. Equilibrium and nonequilibrium molecular-dynamics simulations of the central force model of water. J. Chem. Phys., 115(16):7564–7574, 2001.

[117] D. Wolf, P. Keblinski, S. R. Phillpot, and J. Eggebrecht. Exact method for the simulation of coulombic systems by spherically truncated, pairwise r^{-1} summation. J. Chem. Phys., 110(17):8254–8282, May 1999.

[118] Julian D. Gale. Gulp: A computer program for the symmetry-adapted simulation of solids. J. Chem. Soc., Faraday Trans., 93(4):629–637, 1997.

[119] H. J. C. Berendsen, J. R. Grigera, and T. P. Straatsma. The missing term in effective pair potentials. J. Phys. Chem., 91(24):6269–6271, November 1987.

[120] A. J. Leadbetter, R. C. Ward, J. W. Clark, P. A. Tucker, T. Matsuo, and H. Suga. The equilibrium low-temperature structure of ice. J. Chem. Phys., 82(1):424–428, 1985.

[121] Christina M. B. Line and R. W. Whitworth. A high resolution neutron powder diffraction study of D_2O ice xi. J. Chem. Phys., 104(24):10008–10013, 1996.

[122] Tomoko Ikeda, Shinji Mae, Osamu Yamamuro, Takasuke Matsuo, Susumu Ikeda, and Richard M. Ibberson. Distortion of host lattice in clathrate hydrate as a function of guest molecule and temperature. J. Phys. Chem. A, 104(46):10623–10630, October 2000.

[123] Rainer Feistel and Wolfgang Wagner. A new equation of state for h_2o ice ih. J. Phys. Chem. Ref. Data, 35(2):1021–1047, June 2006.

[124] A. I. Krivchikov, B. Ya. Gorodilov, O. A. Korolyuk, V. G. Manzhelii, O. O. Romantsova, H. Conrad, W. Press, J. S. Tse, and D. D. Klug. Thermal conductivity of xe clathrate hydrate at low temperatures. Phys. Rev. B, 73(6):064203, February 2006.

[125] Ryoji Inoue, Hideki Tanaka, and Koichiro Nakanishi. Molecular dynamics simulation study of the anomalous thermal conductivity of clathrate hydrates. J. Chem. Phys., 104(23):9569–9577, June 1996.

[126] John S. Tse and Mary Anne White. Origin of glassy crystalline behavior in the thermal properties of clathrate hydrates: A thermal conductivity study of tetrahydrofuran hydrate. J. Phys. Chem., 92(17):5006–5011, August 1988.

[127] Martin T.. Dove. Introduction to Lattice Dynamics. Cambridge University Press, 1993.

[128] Qing Wen and Wolfgang Jager. Rotational spectroscopic and ab initio studies of the xe-h_2o van der waals dimer. J. Phys. Chem. A, 110(24):7560–7567, June 2006.

[129] Jadran Vrabec, Jürgen Stoll, and Hans Hasse. A set of molecular models for symmetric quadrupolar fluids. J. Phys. Chem. B, 105(48):12126–12133, November 2001.

[130] Glen A. Slack. Thermal conductivity of ice. Phys. Rev. B, 22(6):3065–3071, September 1980.

[131] Frank H. Stillinger and Thomas A. Weber. Computer simulation of local order in condensed phases of silicon. Phys. Rev. B, 31(8):5262, April 1985.

[132] Patrick K. Schelling, Simon R. Phillpot, and Pawel Keblinski. Comparison of atomic-level simulation methods for computing thermal conductivity. Phys. Rev. B, 65(14):144306, April 2002.

[133] D. P. Sellan, E. S. Landry, J. E. Turney, A. J. H. McGaughey, and C. H. Amon. Size effects in molecular dynamics thermal conductivity predictions. Phys. Rev. B, 81(21):214305, June 2010.

[134] L. Hu, W. J. Evans, and P. Keblinski. One-dimensional phonon effects in direct molecular dynamics method for thermal conductivity determination. J. of App. Phys., 110(11), 2011.

[135] P. G. Klemens. Thermal resistance due to point defects at high temperatures. Phys. Rev., 119(2):507–509, July 1960.

[136] G.D. Samolyuk, S.I. Golubov, Y.N. Osetsky, and R.E. Stoller. Molecular dynamics study of influence of vacancy types defects on thermal conductivity of β-SiC. J. Nucl. Mater., 418:174–181, November 2011.

[137] Glen A. Slack and S. Galginaitis. Thermal conductivity and phonon scattering by magnetic impurities in CdTe. Phys. Rev., 133(1A):A253–A268, January 1964.

[138] L.L. Snead, S.J. Zinkle, and D.P. White. Thermal conductivity degradation of ceramic materials due to low temperature, low dose neutron irradiation. J. Nucl. Mater., 340:187–202, April 2005.

[139] Jie Zou and Alexander Balandin. Phonon heat conduction in a semiconductor nanowire. J. Appl. Phys., 89(5):2932–2938, 2001.

[140] David G. Cahill and R.O. Pohl. Heat flow and lattice vibrations in glasses. Solid State Comm., 70(10):927–930, June 1989.

[141] Albert P. Bartók, Mike C. Payne, Risi Kondor, and Gábor Csányi. Gaussian approximation potentials: The accuracy of quantum mechanics, without the electrons. Phys. Rev. Lett., 104(13):136403, April 2010.

[142] Albert P. Bartók, Risi Kondor, and Gábor Csányi. On representing chemical environments. Phys. Rev. B, 87(18):184115, May 2013.

[143] Harry Partridge and David W. Schwenke. The determination of an accurate isotope dependent potential energy surface for water from extensive ab initio calculations and experimental data. J. Chem. Phys., 106(11):4618–4639, 1997.

[144] Honggang Cui, E. Thomas Pashuck, Yuri S. Velichko, Steven J. Weigand, Andrew G. Cheetham, Christina J. Newcomb, and Samuel I. Stupp. Spontaneous and x-ray-triggered crystallization at long range in self-assembling filament networks. Science, 327(5965):555–559, 2010.

[145] Fangyong Yan, Christopher Adam Hixson, and David J. Earl. Self-assembled chiral superstructures composed of rigid achiral molecules and molecular scale chiral induction by dopants. Phys. Rev. Lett., 101(15):157801, October 2008.

[146] Hiromitsu Maeda, Yoshitaka Terashima, Yohei Haketa, Atsushi Asano, Yoshihito Honsho, Shu Seki, Masahiro Shimizu, Hidetomo Mukai, and Kazuchika Ohta. Discotic columnar mesophases derived from 'rod-like'pi-conjugated anion-responsive acyclic oligopyrroles. Chem Commun (Camb), 46(25):4559–4561, Jul 2010.

[147] Maurice C. D. Mourad, Edwin J. Devid, Matti M. van Schooneveld, Chantal Vonk, and Henk N. W. Lekkerkerker. Formation of nematic liquid crystals of sterically stabilized layered double hydroxide platelets. The Journal of Physical Chemistry B, 112(33):10142–10152, August 2008.

[148] Jonathan P. Hill, Wusong Jin, Atsuko Kosaka, Takanori Fukushima, Hideki Ichihara, Takeshi Shimomura, Kohzo Ito, Tomihiro Hashizume, Noriyuki Ishii, and Takuzo Aida. Self-assembled hexa-peri-hexabenzocoronene graphitic nanotube. Science, 304(5676):1481–1483, 2004.

[149] Wusong Jin, Takanori Fukushima, Makiko Niki, Atsuko Kosaka, Noriyuki Ishii, and Takuzo Aida. Self-assembled graphitic nanotubes with one-handed helical arrays of a chiral amphiphilic molecular graphene. Proc. Nat. Acad. Sci. U.S.A, 102(31):10801–10806, 2005.

[150] Denis Andrienko, Valentina Marcon, and Kurt Kremer. Atomistic simulation of structure and dynamics of columnar phases of hexabenzocoronene derivatives. J. Chem. Phys., 125(12):124902–8, September 2006.

[151] Joaquin Barbera, Laura Puig, Pilar Romero, Jose Luis Serrano, and Teresa Sierra. Propeller-like hydrogen-bonded banana-melamine complexes inducing helical supramolecular organizations. J. Am. Chem. Soc., 128(13):4487–4492, April 2006.

[152] Giorgio Cinacchi and Jeroen S. van Duijneveldt. Phase behavior of contact lens-like particles: Entropy-driven competition between isotropic-nematic phase separation and clustering. The Journal of Physical Chemistry Letters, 1(4):787–791, February 2010.

[153] S Chandrasekhar and G S Ranganath. Discotic liquid crystals. Rep. Prog. Phys., 53(1):57, 1990.

[154] Chun-Long Chen, Peijun Zhang, and Nathaniel L. Rosi. A new peptide-based method for the design and synthesis of nanoparticle superstructures: Construction of highly

ordered gold nanoparticle double helices. Journal of the American Chemical Society, 130(41):13555–13557, October 2008.

[155] Annette Meister, Simon Drescher, Ingo Mey, Mirco Wahab, Gesche Graf, Vasil M. Garamus, Gerd Hause, Hans-Jorg Mogel, Andreas Janshoff, Bodo Dobner, and Alfred Blume. Helical nanofibers of self-assembled bipolar phospholipids as template for gold nanoparticles. J. Phys. Chem. B, 112(15):4506–4511, April 2008.

[156] F. Schmid. Toy amphiphiles on the computer: What can we learn from generic models? Macromol. Rapid Commun., 30(9-10):741–751, 2009.

[157] Martin McCullagh, Tatiana Prytkova, Stefano Tonzani, Nicolas D. Winter, and George C. Schatz. Modeling self-assembly processes driven by nonbonded interactions in soft materials. The Journal of Physical Chemistry B, 112(34):10388–10398, August 2008.

[158] Yehuda Snir and Randall D. Kamien. Entropically driven helix formation. Science, 307(5712):1067–, 2005.

[159] Stefan Tsonchev, George C. Schatz, and Mark A. Ratner. Hydrophobically-driven self-assembly:? a geometric packing analysis. Nano Letters, 3(5):623–626, May 2003.

[160] Jonathan R. Davis and Athanassios Z. Panagiotopoulos. Monte carlo simulations of amphiphilic nanoparticle self-assembly. J. Chem. Phys., 129(19):194706–7, November 2008.

[161] Jonathan R. Davis, Michael V. Piccarreta, Rory B. Rauch, T. Kyle Vanderlick, and Athanassios Z. Panagiotopoulos. Phase behavior of rigid objects on a cubic lattice? Industrial & Engineering Chemistry Research, 45(16):5421–5425, August 2006.

[162] Stefan Tsonchev, Krista L. Niece, George C. Schatz, Mark A. Ratner, and Samuel I. Stupp. Phase diagram for assembly of biologically-active peptide amphiphiles. The Journal of Physical Chemistry B, 112(2):441–447, January 2008.

[163] Stefan Tsonchev, Alessandro Troisi, George C. Schatz, and Mark A. Ratner. All-atom numerical studies of self-assembly of zwitterionic peptide amphiphiles. The Journal of Physical Chemistry B, 108(39):15278–15284, September 2004.

[164] Stefan Tsonchev, Alessandro Troisi, George C. Schatz, and Mark A. Ratner. On the structure and stability of self-assembled zwitterionic peptide amphiphiles:? a theoretical study. Nano Letters, 4(3):427–431, March 2004.

[165] Siewert J. Marrink, H. Jelger Risselada, Serge Yefimov, D. Peter Tieleman, and Alex H. de Vries. The martini force field:? coarse grained model for biomolecular simulations. The Journal of Physical Chemistry B, 111(27):7812–7824, July 2007.

[166] Siewert J. Marrink, Alex H. de Vries, and Alan E. Mark. Coarse grained model for semiquantitative lipid simulations. J. Phys. Chem. B, 108(2):750–760, January 2004.

[167] Luca Monticelli, Senthil K. Kandasamy, Xavier Periole, Ronald G. Larson, D. Peter Tieleman, and Siewert-Jan Marrink. The martini coarse-grained force field: Extension to proteins. J. Chem. Theor. Comp., 4(5):819–834, May 2008.